

ALMA MATER STUDIORUM  
Class LM-71 - Industrial Chemistry  
Second Cycle Degree/Two Year Master in Industrial Chemistry  
Department of Industrial Chemistry "Toso Montanari"

A study of the *trans-cis*  
photoisomerization mechanism of  
azobenzene in liquid crystals

Candidate:  
Lorenzo Soprani

Supervisor:  
Prof. Claudio Zannoni

Cosupervisor:  
Dott. Luca Muccioli  
Dott. Lara Querciagrossa

Academic Year 2017-2018



# Contents

<b>Abstract</b>	<b>5</b>
<b>1 Introduction</b>	<b>7</b>
<b>2 Photophysics and photochemistry of azobenzene</b>	<b>11</b>
2.1 Deactivation of $T_1$ . . . . .	13
2.2 Deactivation of $S_1$ ( $n\pi^*$ ) . . . . .	14
2.3 Deactivation of $S_2$ ( $\pi\pi^*$ ) . . . . .	14
2.4 Applications of azobenzene and its derivatives . . . . .	17
2.4.1 Azobenzene and liquid crystals . . . . .	17
<b>3 Azobenzene Force Field reparameterization</b>	<b>23</b>
3.1 QM-based Force Fields (Class II) . . . . .	23
3.2 QM-based Force Field for azobenzene . . . . .	24
3.2.1 QM and MM calculations details . . . . .	24
3.2.2 How to obtain FF parameters from QM calculations .	30
3.2.3 Bond parameters . . . . .	31
3.2.4 Bending parameters . . . . .	52
3.2.5 Torsion parameters . . . . .	54
3.2.6 Force Field Cross-terms . . . . .	58
<b>4 Molecular Dynamics Simulations of azobenzene photoexcitation</b>	<b>75</b>
4.1 Energy minimization . . . . .	75
4.2 Adaptive Biasing Force profiles . . . . .	78
4.3 Trajectories analysis . . . . .	81
4.3.1 Azobenzene in vacuum . . . . .	81
4.3.2 Azobenzene in 8CB . . . . .	84
<b>5 Conclusions and future outlooks</b>	<b>87</b>
<b>Bibliography</b>	<b>89</b>



# Abstract

In this work we have studied, by means of Molecular Dynamics simulations, the *trans-cis* photoisomerization mechanism of azobenzene dissolved in a liquid crystal when excited in the state associated to the  $n\pi^*$  transition (first excited singlet  $S_1$ ).

A great number of photochemical applications are based on the *trans-cis* photoisomerization of azobenzene-containing materials [1], and, in particular, liquid crystals [2, 3, 4], and even though many studies have been done, the actual conversion mechanism in condensed phases is still not completely known. Herein, with the purpose to continue the work of Tiberio et al. [5], which analyzed the  $n\pi^*$  photoisomerization in vacuum and in various organic solvents, we start the study of the same phenomenon taking place in a liquid crystal (8CB) via a modified molecular dynamics simulation adopting a QM-based class II force field in the ground and excited state, electronic transitions and stochastic decay events to the fundamental state. We describe the procedure used to parameterize the new force field for azobenzene in ground and first excited state, analyze the molecular trajectories, determine the *trans-cis* photoisomerization quantum yield and decay times and compare our results with experimental ones where available.

Quantum mechanics calculations showed that it is fundamental in the decay pathway to reach a molecule conformation in which the central dihedral angle C–N–N–C is about  $90^\circ$  and the two bending angles C–N–N are asymmetric. With molecular dynamics simulations we see that this mechanism is followed, although with some differences, in vacuum as well as in 8CB.



# Chapter 1

## Introduction

Azobenzene (AB) and its derivatives can isomerize if irradiated with light, transforming from the longer *trans* isomer to the shorter, bent, *cis* isomer and vice versa. This shape variation, coupled with the high stability of the *cis* form and the reversibility of the conversion, can be exploited in the design of materials with photoswitchable physical properties [6, 7, 8] for photonic [9] and micro and nanoscale device applications [10, 11]. Thus, understanding the molecular mechanism of the *trans-cis* photoisomerization and how it can take place in the crowded environment of a condensed phase, such as a liquid crystal, is thus a task of great importance and complexity.

The simulation of photoisomerization, which involves excited state dynamics and nonadiabatic crossings between different electronic states, has been challenging computational chemists and physicists for many years [12] [13]. However, notwithstanding the considerable progress of quantum chemical excited-state methods in the investigation of potential energy surfaces (PESs) and of their intersections and in nonadiabatic dynamics techniques [14, 15, 16], fully quantum chemical simulations of a photochemical process in a complex environment is still not feasible. Therefore, it must be found a suitable and less computationally demanding approximation. During the years, many approaches for treating various contributions to the total Hamiltonian at different levels of theory have been developed. For example, in the quantum mechanical/molecular mechanical (QM/MM) method, some atoms, usually belonging to the solvent or to the nonactive part of a large molecule, are treated classically [17], while in the molecular-mechanics valence-bond method [18] and in tight-binding density functional theory [19] the subdivision regards the electrons on each atom. Also, more affordable semiempirical Hamiltonians, suitably parameterized by means of higher-level calculations, have been employed to describe the dynamics of azobenzene-derived chromophores [20, 21], with considerable advantages in terms of computational time, while the interaction with the surrounding environment is again modeled with classical force fields. However, a further

drastic simplification is needed to be able to study the photochemistry of complex systems with adequate sampling and timescales, and it would be desirable to extend to excited states the application of classical force fields, which have proved to be successful in describing and predicting ground-state physical properties. This is certainly becoming possible for phenomena that are determined by the excited state equilibrium geometries, such as steady emission spectra, since in principle they can be described as accurately as the ground-state case with molecular mechanics. The classical description of dynamics processes that take place upon photon absorption is complicated by the large displacements from the excited-state equilibrium geometry that can follow a Franck-Condon transition from the ground state. It is also worth noting that the curvature of the PES along these displacement coordinates is hardly representable with harmonic functions of normal modes [22]. In this context, it has proved helpful to select the vibronic channels relevant for the dynamics [23] and to treat them at the QM level, while adopting more approximate descriptions for the less relevant ones.

AB photophysics has been extensively studied, and various essential features are now understood, at least in the gas phase. The process, which typically occurs in the picosecond timescale, can involve an  $n\pi^*$  or a  $\pi\pi^*$  absorption, depending on the excitation wavelength [24, 25]. Under the most common experimental conditions (near-UV excitation), a three-state mechanism seems to take place, with promotion from the fundamental state  $S_0$  of the *trans* isomer to the second singlet excited state  $S_2$ , followed by a decay to the first singlet state  $S_1$ , and finally by a decay, either nonradiative via conical intersection ( $S_0/S_1$  CI) or radiative by weak fluorescence, to the  $S_0$  state. The process can be even more complex and some authors have recently pointed out the importance of other singlet and triplet states [24, 26]. By comparison, the photophysics of the process following the  $n\pi^*$  absorption from the ground state in the visible region ( $\lambda = 440\text{-}480\text{ nm}$ ) is simpler as it involves only the first excited state  $S_1$ .

The intramolecular mechanism of the isomerization process involves two basic pathways: torsional (dihedral angle C–N–N–C), and via inversion, which implies a wide increase of one of the C–N–N bending angles with an exchange of the position of the lone pair of one of the nitrogen atoms. The two mechanisms have often been considered as alternatives, and their relative contributions to the isomerization is still controversial even in the gas phase, although some precious clarifications have been provided by recent works [20, 24, 25]. In the most general case, the molecule can follow a mixed mechanism that involves both processes and that reduces to pure torsion or inversion only in borderline cases. Since in all practical applications the AB photoisomerization takes place in solution or in a polymer, it is somehow disappointing that the vast majority of the theoretical information available only refers to isomerization in the gas phase, where the conformational change is not hindered by the environment and where we can expect that the

mechanism can be different. As we have seen, part of the difficulty in studying the solvent environment effects on the *trans-cis* isomerization is due to the need for building a model of the process that combines the essential photophysics with an atomistic description of the guest-host system.

The work presented in this thesis consists of a series of preliminary calculations and tests which will allow to face the issue previously treated by Tiberio et al. [5] with a new and more accurate approach, based on QM calculations performed by Prof. M. Garavelli's group of photophysics and photochemistry, and so contribute to this challenging task by following the  $n\pi^*$  transition in a vacuum and in a nematic liquid crystal by using nonequilibrium molecular dynamics (MD) simulations.

In this first and simplified model we allow for transitions from the ground to the  $S_1$  excited state of one molecule at time; we, then, analyze the trajectories in the excited state and evaluate the decay stochastically. The method we propose is in essence a simple QM/MD scheme, and we aim at testing the methodology as well as obtaining new physical insights into the mechanism of photoisomerization in the nematic liquid crystal 4'-octyl-4-biphenylcarbonitrile (8CB). We believe this investigation to be particularly timely, since significant experimental studies on AB photoisomerization in solution following an  $S_1$  excitation have appeared in the last two decades [27, 3].

This thesis is organized as follows: in Chapter 2 we give a more detailed description of the *trans-cis* photoisomerization of azobenzene, in Chapter 3 we show how we parameterized azobenzene force field from QM calculations, and in Chapter 4 we discuss the obtained results.



## Chapter 2

# Photophysics and photochemistry of azobenzene

Azobenzene (AB) and its derivatives are one of the most important classes of photochromic compounds. AB is made of two phenyl rings connected by the N=N azo group and can exist in two forms, namely, the *cis* and *trans* isomers, which can interconvert both photochemically and thermally (see Figure 2.1, and exhibit well-separated absorption bands in the UV-visible region (see Figure 2.2) and different physical properties, such as dielectric constant and refractive index.

The low-energy absorption spectrum of AB shows two main bands: one, weak, in the visible and one, intense, in the near UV spectral region. In *n*-hexane solution of the *trans* isomer at room temperature, the first band exhibits a maximum at 432 nm ( $\epsilon_{\max} = 400 \text{ L mol}^{-1} \text{ cm}^{-1}$ ) and the second one shows a maximum at 318 nm ( $\epsilon_{\max} = 22\,300 \text{ L mol}^{-1} \text{ cm}^{-1}$ ) [29]. The former band is structureless and is attributed to the lowest excited singlet state,  $S_1$ , associated to  $n\pi^*$  excitation and of  $B_g$  symmetry type in the  $C_{2h}$  symmetry group. The  $S_1 \leftarrow S_0$  transition is then symmetry forbidden and becomes allowed when the molecule is deformed along an  $a_u$  coordinate, such as the (properly symmetrized) twistings around C–N bonds. The band in

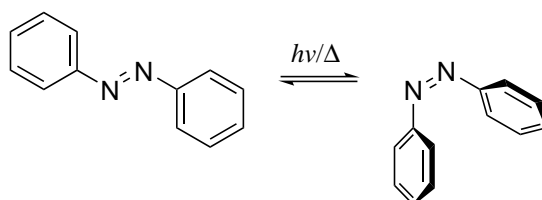


**Figure 2.1:** Azobenzene *trans-cis* photo-/thermal isomerization.

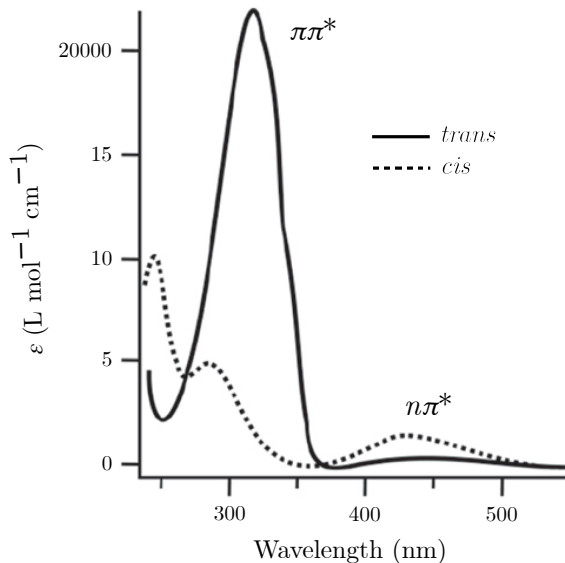


**Figure 2.2:** Electronic absorption spectra of the *trans* and *cis* isomers of azobenzene dissolved in ethanol [28].

**Table 2.1:** Quantum yield  $\Phi$  of *trans*  $\rightarrow$  *cis* and *cis*  $\rightarrow$  *trans* photoconversion of AB in *n*-hexane for  $S_1 \leftarrow S_0$  and  $S_2 \leftarrow S_0$  excitations. Results obtained by Monti and coworkers [32, 33].

$\Phi$	$S_1 \leftarrow S_0$	$S_2 \leftarrow S_0$
<i>trans</i> $\rightarrow$ <i>cis</i>	0.25	0.12
<i>cis</i> $\rightarrow$ <i>trans</i>	0.53	0.40

the UV region presents a rich vibronic structure with the origin at 362 nm in spectra measured in dibenzyl single crystal at 20 K [30], and corresponds to the state  $S_2$ , associates to  $\pi\pi^*$  excitation and of  $B_u$  symmetry type. Thus, while the  $S_1 \leftarrow S_0$  transition is symmetry-forbidden, the  $S_2 \leftarrow S_0$  transition is allowed. The effect of the symmetry selection rules can be observed in the molar extinction coefficients ( $\varepsilon$ ) of the two bands in Figure 2.2.

In the *cis* AB isomer, the frequencies of the absorption bands in the UV-visible absorption spectrum are similar to the ones of the *trans* isome, at 440 and 260 nm. The intensity ratio, instead, is rather different, since the *cis* isomer has a lower symmetry with respect to the *trans* one, and the transition  $n\pi^*$  become more intense [29].

An important and still debated property of the *trans-cis* photoisomerization of AB is the dependence of the quantum yield ( $\Phi$ ) on the excitation wavelength (see Table 2.1) [31]. This violation of the Kasha rule implies that  $S_2$  decays to the ground state bypassing, at least partially the region

where occurs the  $S_1 \rightarrow S_0$  decay. However, this violation disappears in sterically hindered azobenzenes, for example, in azobenzenophanes (ABphanes), where the motion of each AB molecule is somewhat affected by the companion molecule, or in azobenzene-capped crown ether [31].

While in stilbene and in ethylene derivatives the *trans-cis* isomerization can occur only via torsion of the C=C bond, in AB it can proceed along two pathways: the torsion around the N=N double bond and the in-plane inversion. In the latter case, the transition state corresponds to a linear geometry whereby one nitrogen atom is sp hybridized.

The traditional interpretation [31] has assigned the isomerization pathway on the  $S_1$  to inversion and the one on  $S_2$  to torsion, respectively. Assuming that in sterically hindered ABs the torsion motion is frozen, an explanation was provided for the different  $S_1$  and  $S_2$  isomerization quantum yields observed only in AB and not in AB-phanes. Recently, new theoretical and experimental results have questioned this model. Tahara and co-workers [34], through time-resolved fluorescence data, attributed to both  $S_1$  and  $S_2$  photoisomerizations the inversion pathway. On the other hand, Ishikawa and co-workers [35] calculated the potential energy surfaces (PES) of the lowest singlet excited states at the multiconfiguration level and found that their deactivation takes place along the torsion coordinate. Stolow et al. [36], on the basis of combined time-resolved photoelectron spectroscopy observations and *ab initio* calculations, have associated the non-Kasha behavior with the quasi-degeneracy between the benzenic states and the  $S_2$  state localized on the azo group.

We now present the most relevant photoisomerization mechanisms from  $S_1$ ,  $S_2$  and  $T_1$  [20, 24, 25, 37]. For the  $S_1$  and  $S_2$  deactivation we report a more accurate description, while in the case of  $T_1$  state, we give only a brief overview, since it is not too relevant for light organic molecules and for the purpose of this work.

## 2.1 Deactivation of $T_1$

In the ground state, it was found that the optimized barrier for isomerization is ca. 40 kcal mol<sup>-1</sup> higher than the minimum energy *trans* isomer for both inversion and torsion pathways. According to B3LYP calculations, the optimized PES of  $T_1$  along the torsion pathway has its minimum at roughly 105° where its energy is 28.0 kcal mol<sup>-1</sup>. This implies that, provided that the  $S_0$ - $T_1$  spin-orbit coupling is sufficiently strong, thermal isomerization can occur via the  $T_1$  state by overcoming a barrier of about 32 kcal mol<sup>-1</sup>, corresponding to the higher  $S_0$ - $T_1$  crossing.

The isomerization on  $T_1$  was found to show a strong preference for the torsion route: at the B3LYP level, the optimized energies at the twisted and inverted geometry were found to be 28.0 and 48.4 kcal mol<sup>-1</sup>, respectively.

Thus, the AB molecule, once it is excited in  $T_1$  at the *trans* or *cis* geometry, follows the torsion pathway, reaching the minimum where it crosses to  $S_0$  thereby giving isomerization [26].

## 2.2 Deactivation of $S_1$ ( $n\pi^*$ )

From the Frank-Condon (FC) region on  $S_1$  the molecule can reach a planar minimum with wider and still symmetric C–N–N bending angles ( $\vartheta_{\text{CNN}}$  and  $\vartheta_{\text{NNC}}$ ). This planar minimum is located about 10 kcal mol<sup>-1</sup> below the FC geometry. Concerning the the C–N–N–C torsion coordinate, the potential energy curve of  $S_1$  obtained in many calculations [26, 25] is essentially flat.

The  $S_0$ - $S_1$  crossing seam is rather wide and includes both planar geometries characterized by large C–N–N bending angles, and twisted structures with  $\varphi_{\text{CNNC}} = 90^\circ$  and asymmetric C–N–N bending angles (circled zone in Figure 2.3). The former conical intersections (CIs) are found at high potential energy, and therefore inaccessible via direct  $S_1$  population. Furthermore, since they are almost planar, they are unreactive (*i.e.* they lead back to the *trans* isomer). The twisted CIs are almost isoenergetic with the  $S_1$  planar minimum and easily accessible through a TS at  $\varphi_{\text{CNNC}} = 119.7^\circ$ , labeled TS<sub>tors</sub>( $S_1$ ), located at about 2 kcal mol<sup>-1</sup> above the *trans* isomer one. [24]. These CIs are the reactive ones and can lead to the formation of the *cis* isomer.

The  $S_1$  minimum energy path (MEP) follows the torsion coordinate during the whole isomerization. It appears that, as the CNNC torsion increases, the coupling between the two nitrogen lone-pairs weakens and the  $n\pi^*$  excitation tends to localize predominantly on one moiety because of the electron-phonon coupling, that is, of the nuclear reorganization energy associated with the excitation. As a consequence, the two moieties become nonequivalent (*i.e.*,  $\vartheta_{\text{CNN}} \neq \vartheta_{\text{NNC}}$ ).

In Figure 2.3 it is also shown a high energy  $S_1/S_0$  CI in the region of the inverted geometry, labeled CI<sub>inv</sub>, in which one of the two NNC angles is close to 180° and the CNNC dihedral angle is 108.7°.

To sum up, the quantum yields are determined by the competition between the  $S_1/S_0$  internal conversion (IC) and the torsional motion around the N=N double bond: if the IC occurs too early, that is, much before the midpoint along the torsional coordinate ( $\varphi_{\text{CNNC}} = 90^\circ$ ), no isomerization occurs, because of the unfavourable slope of the  $S_0$  PES [20].

## 2.3 Deactivation of $S_2$ ( $\pi\pi^*$ )

MS-3-RASPT2/SA-3-RAS calculations [37] found a  $S_2$  planar minimum characterized by still symmetric C–N–N bending angles ( $\vartheta_{\text{CNN}} = \vartheta_{\text{NNC}} =$

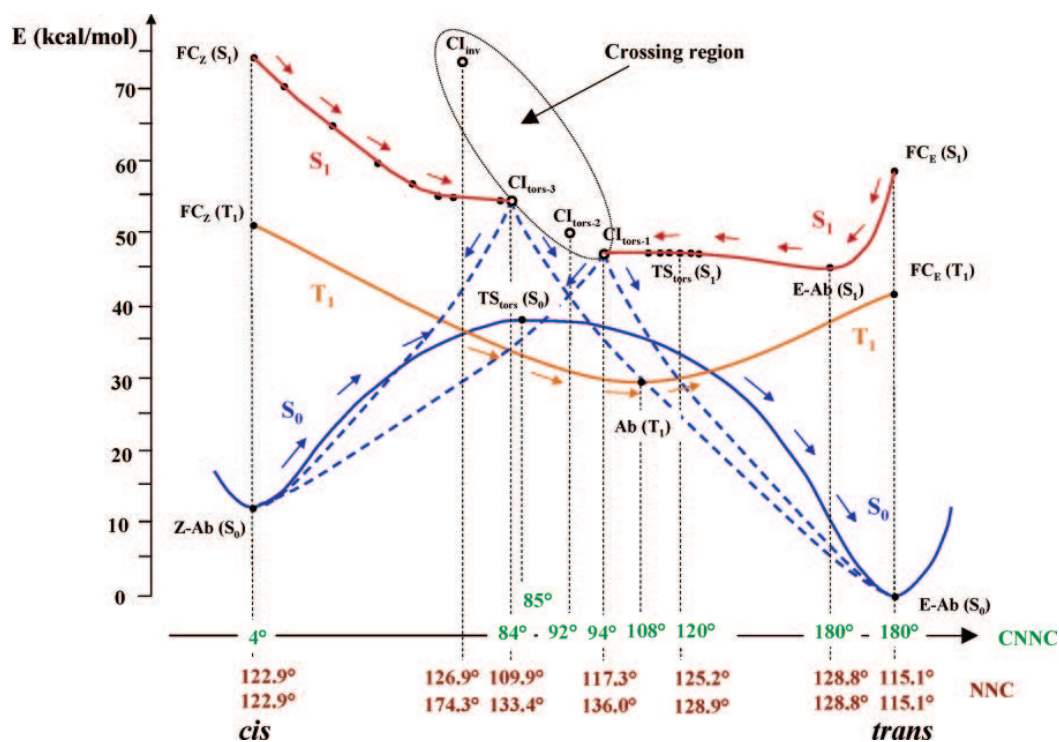


**Figure 2.3:** Schematic representation of singlet ( $S_0$  and  $S_1$ ) and triplet ( $T_1$ ) MEPS for the *trans-cis* photoisomerization of AB. Open circles represent  $S_1/S_0$  CI. The horizontal axis represents the C-N-N-C torsion coordinate (green numbers). Values for N-N-C angles are also reported (brown numbers). The shaded region highlights the  $S_1/S_0$  crossing space and embraces the low-energy (*i.e.*, torsion) and high-energy (*i.e.*, inversion) deactivation funnels. The paths of  $T_1$  and  $S_1$  radiationless decays are also shown. [24]

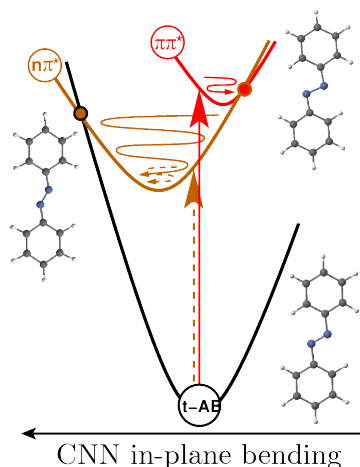


**Figure 2.4:** Simplified scheme of the  $S_2 \rightarrow S_0$  decay in the space of C–N–N in-plane bending. Note that C–N–N angle increases to the left. [37]

111°), smaller with respect to the  $S_0$  *trans* minimum. After the FC excitation, the molecule relaxation toward the  $S_2$  minimum causes also a rearrangement of the bond lengths: N=N bond length increases and the C–N bonds shorten, so that all three bonds lengths become of about 1.4 Å.

In Figure 2.4 it is shown a simplified scheme of the  $S_2$  deactivation projected along the C–N–N in-plane bending. During the molecule relaxation around the  $S_2$  minimum, which are mainly characterized by N=N and C–N stretching modes,  $S_2$  crosses several times with the  $S_1$  state without decay, and these crossings are correlated to the in-plane C–N–N bending. In fact, a planar CI was found at  $\vartheta_{\text{CNN}} = \vartheta_{\text{NNC}} = 104.5^\circ$ , but the nonadiabatic coupling is zero for that geometry. Out-of-plane deformations are required to have a nonzero nonadiabatic coupling. Another CI was found at  $\vartheta_{\text{CNN}} = 108^\circ$ ,  $\vartheta_{\text{NNC}} = 104^\circ$  and  $\varphi_{\text{CNNC}} = 167^\circ$ , through which the internal conversion can occur (less than 100 fs after the  $S_2 \leftarrow S_0$  excitation). [37]

Once in  $n\pi^*$  state, the molecule is found at a considerably high potential energy and can, in principle, access all the above mentioned  $S_1/S_0$  CIs, including the non-reactive ones. Indeed, *ab initio* molecular dynamics (MD) simulations within the second-order multiconfigurational perturbation theory (CASPT2) framework from the FC point on the  $\pi\pi^*$  state confirmed that the hot  $n\pi^*$  population can decay to the GS through a high-energy near-planar region of the  $S_1/S_0$  CI, which is not accessible upon selective excitation of the  $S_1$  state [37]. As we argued in the previous paragraph, this CI region is not reactive, and this explains the fall in the photoisomerization quantum yield and the violation of the Kasha rule.

Figure 2.5 sums up the two mechanisms described above.

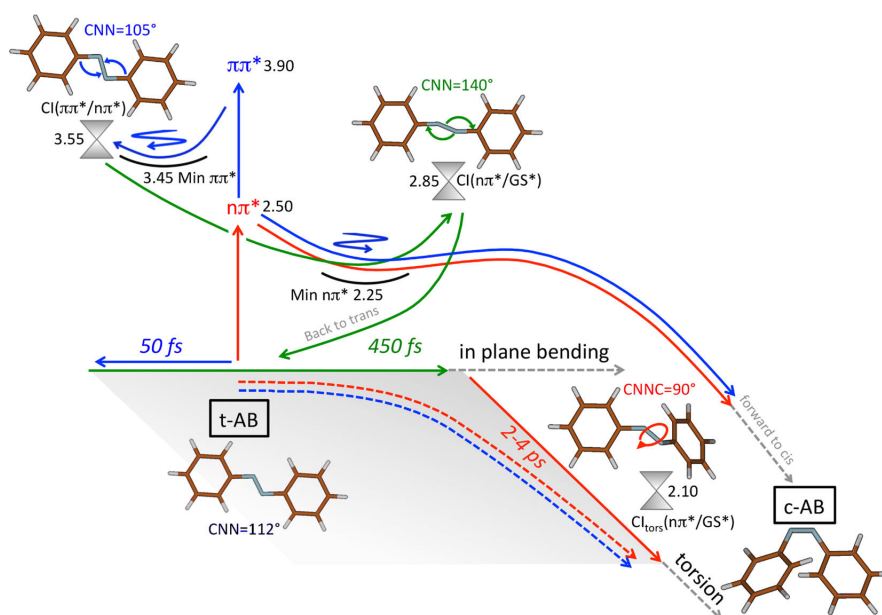


**Figure 2.5:** Overview of the photochemistry of *trans*-AB in the space of the C–N–N in-plane bending and C–N–N–C torsion modes. Excitation of the bright  $S_2 \leftarrow S_0$  transition in the UV (320 nm) opens a subps nonreactive decay channel to the GS via  $\pi\pi^* \rightarrow \text{CI}(\pi\pi^*/n\pi^*) \rightarrow n\pi^* \rightarrow \text{CI}(n\pi^*/S_0)$  (hot channel). [37]

## 2.4 Applications of azobenzene and its derivatives

As we saw, the *trans* and *cis* isomers absorption bands are well separated (see Figure 2.2). This, combined with their different physical properties, such as the refractive index, the dipole moment or the dielectric constant, make azobenzene and its derivatives suitable materials for devices with photomodulable properties. For example, AB has been used in light-triggered switches constituents of erasable holographic data [38], image storage devices [39] and as a possible basis for a light-powered molecular machine [40].

For these reasons, the photophysical and photochemical properties of AB have been and still are the subject of a widespread interest. A great variety of properties and functions can be made photoswitchable: structure and self-organization of materials, chemical and biochemical activity, optical, electrical and permeation parameters.

One of the most relevant and intriguing applications of AB and its derivatives for the scope of this work, is their use in field of the liquid crystals, either as a mesogenic unit [38, 4] or as a solute [6, 2, 3].

### 2.4.1 Azobenzene and liquid crystals

Zannoni and co-workers [41] have explored the changes in the phase stability, orientational order, and dynamics of the nematic 4-cyano-4'-*n*-pentylbiphenyl

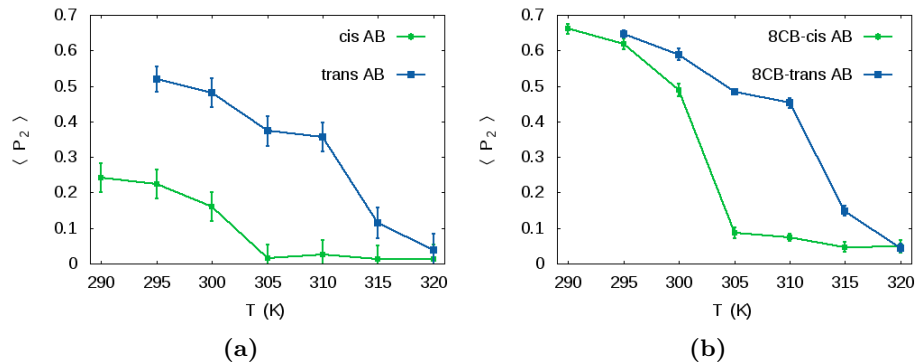


**Figure 2.6:** Calculated  $\langle P_2 \rangle$  order parameter of AB (left) and 8CB (right) in a sample of *trans* (blue line) or *cis* (green line) AB dissolved in 8CB (mole fraction: 0.045) as a function of the temperature. [42]

(5CB) doped with either the *trans* or the *cis* form of different *p*-azobenzene derivatives using the ESR spin-probe technique. In particular they tried to relate the order parameter  $\langle P_2 \rangle$ , the shift of the nematic-isotropic transition temperature ( $T_{NI}$ ) to the solute shape and charge distribution. In all the cases the presence of the azo-derivative causes a depression of  $T_{NI}$ , more pronounced for the *cis* isomers. They also noted that in the presence of the *cis* isomers the samples showed a region of phase separation which was almost negligible at a concentration 1% but became quite evident at higher concentrations (7%) and was found to be wider in samples with larger  $T_{NI}$  shifts.

Thus, isothermal phase transitions of LCs can be induced reversibly by photochemical reaction of photochromic molecules dispersed in the LC phase and with a rapid optical response that typically goes from 50 to 300 microseconds [38, 3]. Figure 2.5 shows the effect of the shape of AB on the  $\langle P_2 \rangle$  order parameter of the nematic liquid crystal 4'-octyl-4-biphenylcarbonitrile (8CB) and of AB itself. We can observe that the AB change of conformation reduces  $T_{NI}$  of about 10 K.

Recently, Goda and co-workers [3] studied the transmittance, the optical switching time and the relaxation time of a guest-host liquid crystal (GH LC) (4-pentyl-4'-cyanobiphenyl) containing more than 4% wt azobenzene guest molecules. A sketch of their device is shown in Figure 2.5. In absence of UV-light, the LC, azobenzene and dichroic dye are vertically aligned (V-state) and visible light can pass through the LC layer because azobenzene and the dichroic dye have weak absorption parallel to the short axis. Upon irradiation of the LC cell with unpolarised UV light, the isotropic state is obtained. When the device is in the isotropic state, visible light is absorbed because of the random alignment of the dichroic dye. After the unpolarised UV light is turned off, the system changes spontaneously back to the V-state

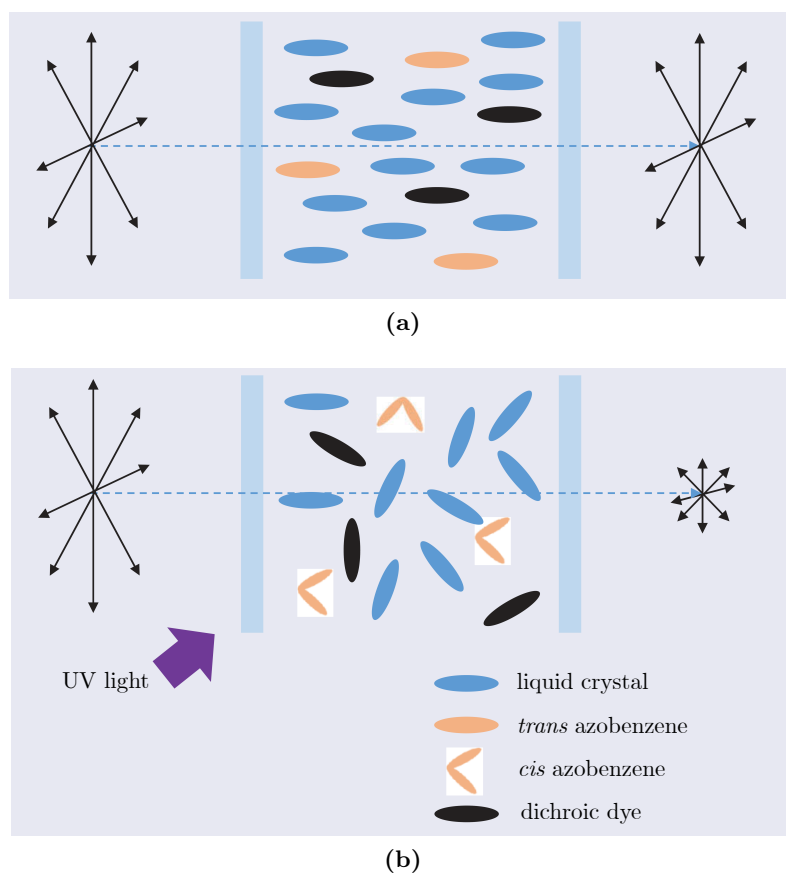


**Figure 2.7:** Scheme of a guest-host liquid crystal (GH LC) with a photocromic molecule (azobenzene). Top: no UV light, the system is vertical aligned (V-state). Bottom: UV light irradiation, the system is isotropic (I-state). [3]

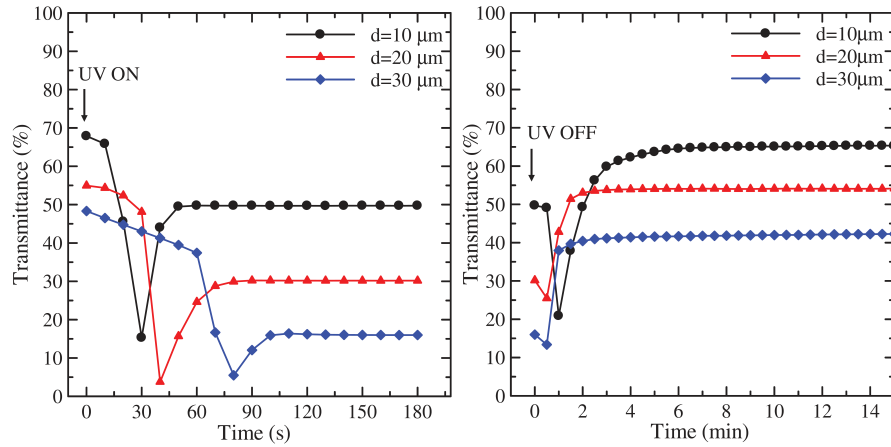


**Figure 2.8:** Transmittance of the GH LC containing azobenzene as a function of time at different cell thicknesses. Left: optical switching time. Right: relaxation time. [3]

through the thermal isomerization of azobenzene (*i.e.*, relaxation process). Their results are shown in Figure 2.7. These unique devices are expected to find use as dimming glass that can be controlled by sunlight.

Azobenzene molecules can be incorporated into polymer matrices as stabilizers. The rigid rod-like structure of azo molecules allows them to behave as liquid-crystal mesogens in many materials. Azobenzene liquid crystals have been developed, in which azobenzene moieties play roles as both mesogens and photosensitive chromophores and some azobenzene derivatives in the *trans* form exhibit a nematic phase (see Figure 2.9), whereas their isomers in the *cis* form show no LC phase. If a large fraction (ideally, all molecules) of the LC azobenzene molecules (*trans* form) in the nematic phase could be isomerized to the *cis* form simultaneously by means of a short laser pulse, the disappearance of the LC phase could take place in principle on the same time scale as the *trans-cis* photoisomerization.

The importance of these devices lies in the fact that they just need an electromagnetic wave and not an external electric field, which could bring technologies advantages.

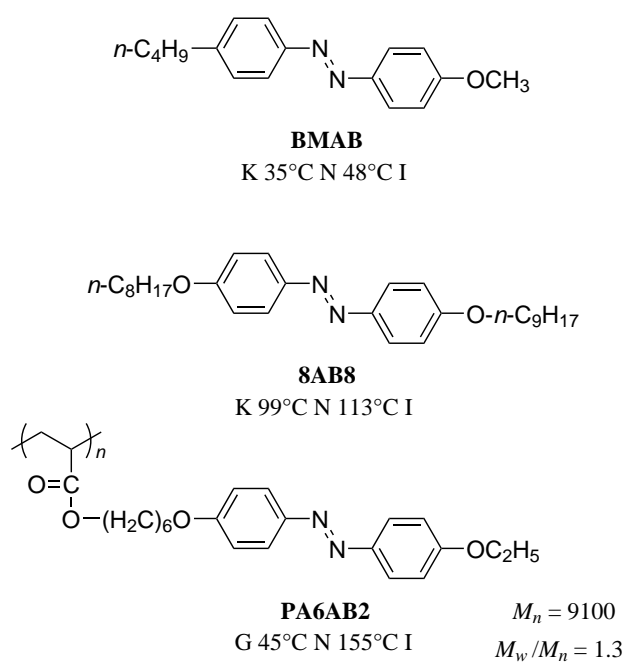


**Figure 2.9:** Structures and phase-transition temperatures of three azobenzene liquid crystals. K: crystal; N: nematic; I, isotropic; G: glass;  $M_n$ : number-average molecular weight;  $M_w$ : weight-average molecular weight. [38]



## Chapter 3

# Azobenzene Force Field reparameterization

### 3.1 QM-based Force Fields (Class II)

The fast evolution of experimental research in complex molecular systems has led to greatly increased need for accurate molecular simulation techniques. The molecular mechanics and dynamics are techniques based on an analytic energy function of the atomic coordinates, the force field (FF), that governs all the relevant molecular energetic, structural, and dynamic properties. Although in some applications only a qualitative description of the studied systems derived from the simulation is sufficient, in the great majority of cases, such as in the one treated in this work, an increasingly higher level of accuracy is crucial to obtaining meaningful results. Examples include structural models of biological species, simulation of enzymatic reaction rates [43] and binding constant [44], prediction of protein structures and interaction energies [45] and study of photophysical and photochemical phenomena [5].

A number of factors affect the accuracy of molecular simulations as compared to practical experimental results, including the treatment of solvent, counterions, and other species that may be present in the real environment, as well as other details of the simulation techniques. However, no advance in these techniques can compensate for inadequacies in the underlying FF. Further, because in practice the final results will generally depend on a delicate balance of many differing types of terms in the model, inadequacies in a FF may be manifested by important qualitative errors in predicted results.

Force fields have traditionally been derived almost exclusively from experimental data, including thermodynamic data (such as conformational energy differences, rotational barriers, and sublimation energies), vibrational frequencies, gas-phase molecular structures, and crystal structures. These information is often rare for many functional groups and sometimes rela-

tively nonexistent. A lack of such experimental data makes it difficult and in some cases impossible to parameterize and test accurate potential energy functions for use in molecular mechanics and dynamics [46].

Further, to account for the intricacies of the energy surfaces of molecules, this data contains a wealth of information on the energy of distorted structures (*i.e.*, anharmonicity), transition states, and the energy changes accompanying displacements of particular internal coordinates, information that is virtually inaccessible to experiment. It is important to note that parameterizing the energy of a molecule employing the quantum mechanical energy surface not only provides a mean for determining the numerical values of individual terms, but also permits development of the analytic form of the energy expression as well [46].

Force fields derived by fitting QM potential energy provide a good starting point when experimental data for representative molecules of a given functional group is too limited or even entirely unavailable. This method is also useful when one needs a prompt derivation of necessary terms in the force field and time is not available for fits of experimental data.

## 3.2 QM-based Force Field for azobenzene

Considering that our simulations deal with photophysical phenomena, such as azobenzene *trans-cis* photoisomerization, several azobenzene force field (FF) parameters for the ground state ( $S_0$ ) and the first excited state ( $S_1$ ) have been recalculated and some new terms were added, in order to increase simulations accuracy. Standard FFs are designed to reproduce correctly the molecules only close to the equilibrium geometry, while we need an accurate description also for higher potential energy molecular geometries. Indeed, the minimum energy structures of the two electronic states differ remarkably, thus, after a vertical electronic excitation, the molecule is found to a high potential energy in the other state.

Starting from AMBER General Force Field (GAFF) for organic molecules (Version 1.4, March 2010) [47], we calculated new parameters, with the aim of minimizing the difference between molecular mechanics ( $U_{\text{MM}}(\mathbf{r})$ ) and quantum mechanics ( $U_{\text{QM}}(\mathbf{r})$ ) potential energy (PE), so as to reproduce *ab initio* energy profiles with classical simulations. In the next sections, we describe the details of the procedure for the force field derivation.

### 3.2.1 QM and MM calculations details

Quantum Mechanics (QM) calculations at DFT level of the theory were performed with the software Gaussian [48], using the PBE0 functional and the cc-pVTZ basis set; MP2 and SS-CASPT2/MS-CASPT2 calculations at RASSCF/CASSCF level were performed by Prof. Marco Garavelli's group of photophysics and photochemistry with the software MOLCAS 8 [49], using

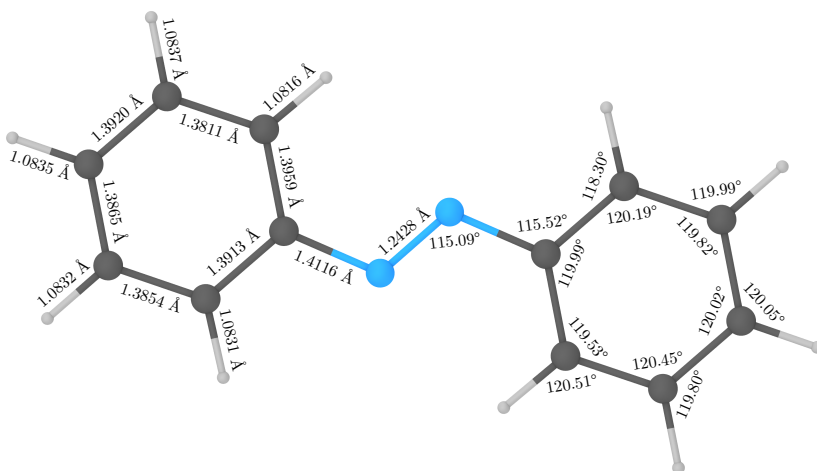


**Figure 3.1:** DFT optimized  $S_0$  azobenzene *trans* isomer. Since the molecule in this conformation belongs to the  $C_{2h}$  point group, bond lengths are indicated in the left part and bending angles in the right one (all the dihedral angles are  $0^\circ$  or  $180^\circ$ ). Calculation details: PBE0 functional, cc-pVTZ basis set.

the ANO-L-VDZP basis set, the active space used consists of 16 orbitals and 18 electrons (full  $\pi$  system plus the two  $n$  orbitals, consisting of the nitrogens lone pairs); Molecular Mechanics (MM) calculations were performed with an in-house modified version of NAMD.

In order to develop an effective method and have initial approximated values to compare with later MP2 and CASPT2 results, we made some test DFT calculations for  $S_0$  AB, using PBE0 functional and cc-pVTZ basis set. We first optimized  $S_0$  *trans* molecular geometry (Figure 3.1), then computed and symmetrized ESP atomic charges and obtained all the geometries required for the parameterization changing the optimized one.

After this preliminary test, we optimized  $S_0$  *trans* and *cis* molecular geometries at MP2 level (ANO-L-VDZP basis set), computed and symmetrized ESP atomic charges (DFT, PBE0//cc-pVTZ) and obtained all the geometries required for the parameterization changing the optimized ones.

We fitted  $S_0$  standard FF parameters for all bonds, some bending and one dihedral for the *trans* isomer, while non-standard ones (*i.e.* those relative to C–N–N bending and C–N–N–C torsion, which are the most involved in the photoisomerization) for a specific combination of the two isomers, described in paragraph 3.2.6.

As we argued in Chapter 2, Cembran et al. [24] found a planar minimum with a very small torsional barrier of about  $2 \text{ kcal mol}^{-1}$ . We did not search for that TS, thus we are not certain about its potential energy at our level of the theory.

We optimized  $S_1$  molecular geometry at RASSCF/MS-CASPT2 level (ANO-

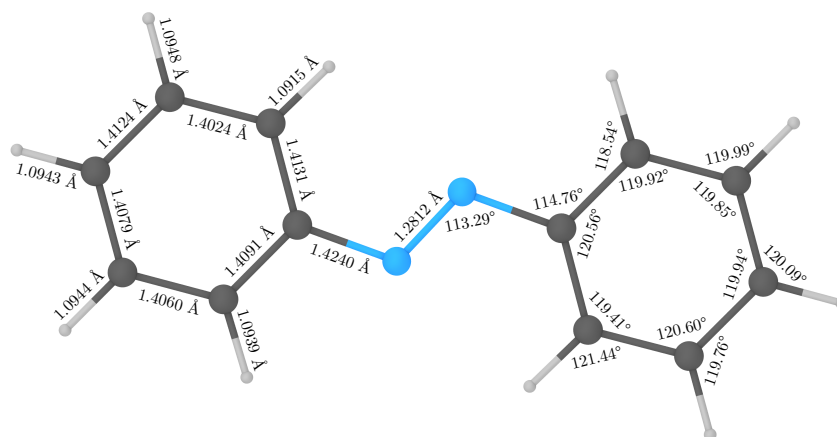


**Figure 3.2:** MP2 optimized azobenzene  $S_0$  *trans* isomer. Since the molecule in this conformation belongs to the  $C_{2h}$  point group, bond lengths are indicated in the left part and bending angles in the right one (all the dihedral angles are  $0^\circ$  or  $180^\circ$ ). Calculation details: ANO-L-VDZP basis set.

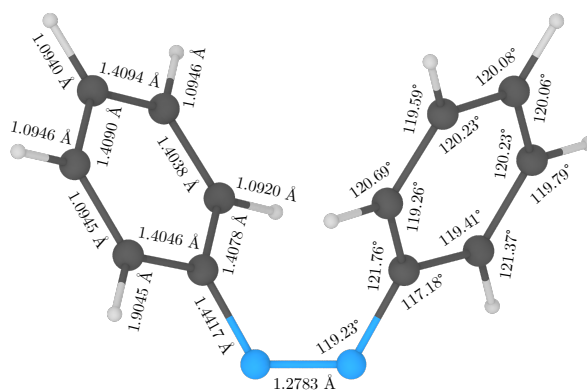


**Figure 3.3:** MP2 optimized azobenzene  $S_0$  *cis* isomer. Since the molecule in this conformation belongs to the  $C_2$  point group, bond lengths are indicated in the left part and bending angles in the right one. Most relevant dihedral angles (not indicated in the figure):  $\varphi_{\text{CNNC}} = 5.67^\circ$ ;  $\varphi_{\text{CCNN}_1} = 128.64^\circ$ ;  $\varphi_{\text{CCNN}_2} = 55.85^\circ$ . Calculation details: ANO-L-VDZP basis set.

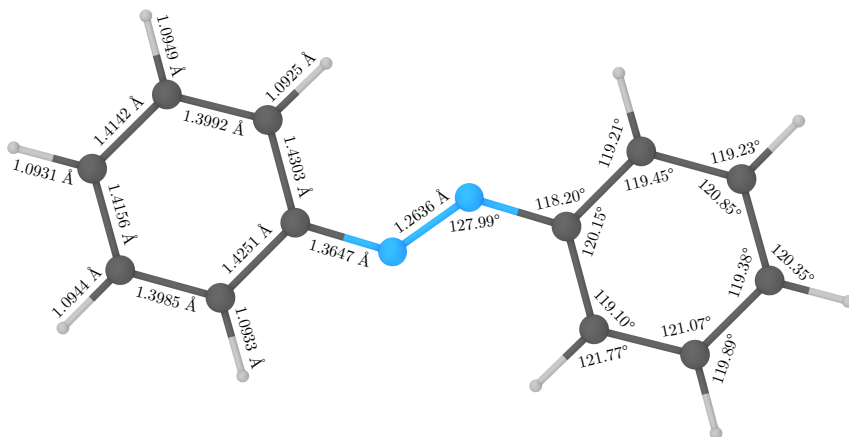


**Figure 3.4:** MS-CASPT2 optimized azobenzene  $S_1$  planar isomer. Since the molecule in this conformation belongs to the  $C_{2h}$  point group, bond lengths are indicated in the left part and bending angles in the right one (all the dihedral angles are  $0^\circ$  or  $180^\circ$ ). Calculation details: RASSCF/MS-CASPT2, ANO-L-VDZP basis set, active space of 16 orbitals and 18 electrons (RAS1 = 9, RAS2 = 0, RAS3 = 7; max. 4 excitations between RAS1 and RAS3).

L-VDZP basis set, active space: 16 orbitals and 18 electrons, RAS1=9 orbitals, RAS2=0 orbitals, RAS3=7 orbitals, at most 4 excitations between RAS1 and RAS3), finding three minimum energy conformations: one planar minimum ( $\mathbf{r}_{\text{plmin}}$ ), similar to  $S_0$  *trans* isomer (see Figure 3.4), one twisted minimum ( $\mathbf{r}_{\text{twmin}}$ ), at  $\varphi_{\text{CNNC}} = 97^\circ$ , and a conical intersection ( $\mathbf{r}_{\text{CI}}$ ), at  $\varphi_{\text{CNNC}} = 95^\circ$ . Both  $\mathbf{r}_{\text{twmin}}$  and  $\mathbf{r}_{\text{CI}}$  have asymmetric C–N–N bending angles.  $S_1$  planar minimum and conical intersection are rather similar to the ones found by Cembran and co-workers [24]. Then, we computed and symmetrized ESP atomic charges (TDDFT, PBE0 functional, cc-pVTZ basis set, solved for 4 singlets) and obtained all the geometries required for the parameterization changing the  $S_1$  planar minimum one.

As for  $S_0$ , We fitted  $S_0$  standard FF parameters for all bonds, some bending and one dihedral for the planar optimized geometry, while non-standard ones (*i.e.* those of C–N–N and N–N–C bending angles and C–N–N–C torsion) for the same geometries used for  $S_0$  FF parameterization (paragraph 3.2.6).

Adopted atomic numbering for azobenzene is shown in Figure 3.5, while calculated ESP atomic charges for each geometry are displayed in Table 3.1. We did not change GAFF LJ parameters (Table 3.2) and kept the same values for  $S_0$  and  $S_1$  FF in MM calculations. Since we noted that internal LJ interactions cause troubles in reproducing *ab initio* PE profiles and prevented us from obtaining suitable parameters (bending ones were the most affected), we decided to bring intramolecular 1-4 interaction scaling factors

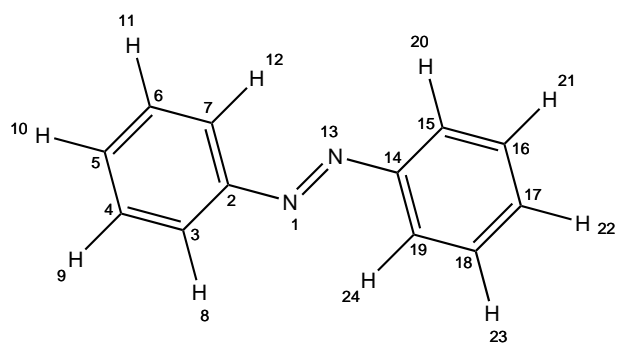


**Figure 3.5:** Azobenzene *trans* isomer and adopted atomic numbering.

to zero (intramolecular 1-2 and 1-3 interactions scaling factors are zero as default option in AMBER FFs).

**Table 3.1:** Atomic ESP charges of azobenzene  $S_0$  *trans* isomer (DFT, PBE0//cc-pVTZ) and  $S_1$  planar isomer (TDDFT, PBE0//cc-pVTZ).

N.	Atom	$S_0$ <i>trans</i> isomer <sup>(a)</sup> ( <i>e</i> units)	$S_0$ <i>trans</i> isomer <sup>(b)</sup> ( <i>e</i> units)	$S_1$ planar isomer <sup>(c)</sup> ( <i>e</i> units)
1-13	N	-0.246 32	-0.240 08	-0.059 12
2-14	C	0.461 88	0.441 78	0.372 91
3-15	C	-0.341 63	-0.337 98	-0.360 95
4-16	C	-0.017 93	-0.010 23	-0.070 59
5-17	C	-0.248 31	-0.253 11	-0.262 42
6-18	C	-0.123 31	-0.102 74	-0.109 45
7-19	C	-0.143 50	-0.171 93	-0.284 65
8-20	H	0.149 74	0.155 22	0.184 43
9-21	H	0.124 63	0.121 36	0.128 95
10-22	H	0.162 00	0.161 65	0.148 64
11-23	H	0.147 91	0.142 00	0.138 82
12-24	H	0.074 83	0.094 07	0.173 43

Optimization details:

<sup>(a)</sup>DFT, PBE0//cc-pVTZ; <sup>(b)</sup>MP2, ANO-L-VDZP;

<sup>(c)</sup> RASSCF/MS-CASPT2, ANO-L-VDZP.

**Table 3.2:** Atomic LJ parameters of azobenzene  $S_0$  *trans* isomer and  $S_1$  planar isomer. It is worth noting that parameters for intramolecular 1-4 interactions are distinguished from the others.

Atom	$\epsilon_j$ (kcal/mol)	$\frac{1}{2} r_{j \text{ min}}$ (Å)	$\epsilon_{j \text{ 1-4}}$ (kcal/mol)	$\frac{1}{2} r_{j \text{ min 1-4}}$ (Å)
N	0.1700	1.824	0.0850	1.824
C	0.0860	1.908	0.0430	1.908
H	0.0150	1.459	0.0075	1.459

### 3.2.2 How to obtain FF parameters from QM calculations

Molecular Mechanics potential energy ( $U_{\text{MM}}(\mathbf{r})$ ) consists of different independent terms, summarized in equation (3.1)

$$U_{\text{MM}}(\mathbf{r}) = U_{\text{b}}(\mathbf{r}) + U_{\text{nb}}(\mathbf{r}), \quad (3.1)$$

where  $\mathbf{r}$  is the set of atoms coordinates,  $U_{\text{b}}(\mathbf{r})$  is the sum of bonded potential energy contributions, while  $U_{\text{nb}}(\mathbf{r})$  is the sum of nonbonded potential energy contributions. Making the terms  $U_{\text{b}}$  and  $U_{\text{nb}}$  explicit,

$$U_{\text{b}}(\mathbf{r}) = \sum_{\text{bond } ab} U_{\text{str}}(r_{ab}) + \sum_{\text{ang } abc} U_{\text{bend}}(\vartheta_{abc}) + \sum_{\text{dih } abcd} U_{\text{tors}}(\varphi_{abcd}), \quad (3.2)$$

$$U_{\text{nb}}(\mathbf{r}) = \sum_{\text{pair } kl} U_{\text{el}}(r_{kl}) + \sum_{\text{pair } kl} U_{\text{LJ}}(r_{kl}), \quad (3.3)$$

where  $U_{\text{str}}(r_{ab})$ ,  $U_{\text{bend}}(\vartheta_{abc})$ ,  $U_{\text{tors}}(\varphi_{abcd})$ ,  $U_{\text{el}}(r_{kl})$  and  $U_{\text{LJ}}(r_{kl})$  are stretching, bending, torsional, electrostatic and Lennard-Jones (LJ) PE terms, respectively; indices  $\text{bond } ab$ ,  $\text{ang } abc$  and  $\text{dih } abcd$  run over all the pairs  $ab$  (bonds), triples  $abc$  (angles) and quadruples  $abcd$  (dihedrals) of covalently bonded atoms, respectively, while indices  $kl$  runs over all the couples  $kl$  of atoms (not necessarily bonded).

Defining  $\mathbf{r}_{\text{min}}$  the set of atomic coordinates of the QM optimized azobenzene molecule, and labelling  $U_{\text{QM}}(\mathbf{r}_{\text{min}})$  and  $U_{\text{MM}}(\mathbf{r}_{\text{min}})$  its QM and MM potential energy, respectively, we can take them as reference values; thus, we get at any geometry

$$\Delta U(\mathbf{r}) \equiv U(\mathbf{r}) - U(\mathbf{r}_{\text{min}}), \quad (3.4)$$

$$\Delta U_{\text{QM}}(\mathbf{r}) \equiv U_{\text{QM}}(\mathbf{r}) - U_{\text{QM}}(\mathbf{r}_{\text{min}}), \quad (3.5)$$

$$\begin{aligned} \Delta U_{\text{MM}}(\mathbf{r}) &\equiv U_{\text{MM}}(\mathbf{r}) - U_{\text{MM}}(\mathbf{r}_{\text{min}}) = \\ &= \Delta U_{\text{b}}(\mathbf{r}) + \Delta U_{\text{nb}}(\mathbf{r}). \end{aligned} \quad (3.6)$$

The aim of the reparameterization is to reproduce *ab initio* PE profiles, therefore the difference between  $\Delta U_{\text{MM}}(\mathbf{r})$  and  $\Delta U_{\text{QM}}(\mathbf{r})$ , from here on called  $\chi(\mathbf{r})$ , has to be minimized. Hence, we can write our problem as

$$\Delta U_{\text{b}}(\mathbf{r}) + \Delta U_{\text{nb}}(\mathbf{r}) = \Delta U_{\text{QM}}(\mathbf{r}) + \chi(\mathbf{r}), \quad (3.7)$$

where  $\chi(\mathbf{r})$  is the residual. Assuming the QM potential energies and MM potential energy terms have been sampled in the set of  $N$  geometries  $\{\mathbf{r}_1, \dots, \mathbf{r}_N\}$ , the problem is solved minimizing the sum of the squared residuals ( $\chi^2$ ), defined as

$$\chi^2 \equiv \|\chi(\mathbf{r})\|^2 = \sum_i^N [\Delta U_{\text{b}}(\mathbf{r}_i) + \Delta U_{\text{nb}}(\mathbf{r}_i) - \Delta U_{\text{QM}}(\mathbf{r}_i)]^2, \quad (3.8)$$

by changing the FF parameters. Actually, we fit the FF parameters so as to reproduce.

Equation (3.7) relates QM PE to MM PE, allowing to obtain FF parameters, as we will show later.

In the next sections we will express the fits error with the root-mean-square absolute error (RMSAE) and the root-mean-square relative error (RMSRE), defined as

$$\begin{aligned} \text{RMSAE} &\equiv \sqrt{\frac{\chi^2}{N}}, \\ \text{RMSRE} &\equiv \frac{\text{RMSAE}}{\langle \Delta U_{\text{QM}}(\mathbf{r}_i) \rangle_i}, \end{aligned} \quad (3.9)$$

where  $\langle \Delta U_{\text{QM}}(\mathbf{r}_i) \rangle_i$  is the average of  $\Delta U_{\text{QM}}(\mathbf{r})$  over the  $N$  molecular geometries  $\{\mathbf{r}_i\}$ :

$$\langle \Delta U_{\text{QM}}(\mathbf{r}_i) \rangle_i = \frac{1}{N} \sum_i^N \Delta U_{\text{QM}}(\mathbf{r}_i). \quad (3.10)$$

The standard deviation absolute errors (SDAE) and relative errors (SDRE) on the FF parameters values will be expressed with the diagonal values of the estimated covariance matrix .

### 3.2.3 Bond parameters

The 2-body spring bond potential describes the harmonic vibrational motion between an  $(a, b)$ -pair of covalently bonded atoms, and has the form

$$U_{\text{str}}(r_{ab}) = k_{ab} (r_{ab} - r_{ab0})^2, \quad (3.11)$$

where  $r_{ab} = |\mathbf{r}_b - \mathbf{r}_a|$  is the distance between the atoms, while  $r_{ab0}$  and  $k_{ab}$  are the equilibrium distance and the spring constant of the bond  $ab$  in the FF, respectively. Note that  $r_{ab0}$  is not necessarily equal to  $r_{ab\text{min}}$ : it is the equilibrium distance between the two body  $a$  and  $b$  if the only force acting on them were the gradient of the potential described in equation (3.11).

If it is possible to modify the minimum energy geometry in such a way that only a single bond distance  $r_{ab}$  varies, without altering other variables, the only terms that will change in the expression of  $U_{\text{MM}}(\mathbf{r})$  are  $U_{\text{str}}(r_{ab})$  and  $U_{\text{nb}}(\mathbf{r})$ ; thus, rewriting (3.7),

$$\Delta U_{\text{str}}(r_{ab}) + \Delta U_{\text{nb}}(\mathbf{r}) = \Delta U_{\text{QM}}(\mathbf{r}) + \chi(\mathbf{r}), \quad (3.12)$$

$$\Delta U_{\text{str}}(r_{ab}) = \Delta U_{\text{QM}}(\mathbf{r}) - [\Delta U_{\text{el}}(\mathbf{r}) + \Delta U_{\text{LJ}}(\mathbf{r})] + \chi(\mathbf{r}). \quad (3.13)$$

Where, for a more concise notation, we defined

$$\begin{aligned} \Delta U_{\text{el}}(\mathbf{r}) &\equiv \sum_{\text{pair } kl} \Delta U_{\text{el}}(r_{kl}), \\ \Delta U_{\text{LJ}}(\mathbf{r}) &\equiv \sum_{\text{pair } kl} \Delta U_{\text{LJ}}(r_{kl}). \end{aligned} \quad (3.14)$$

**Table 3.3:**  $S_0$  *trans* isomer DFT PE and MM PE contributions computed for different N–N bond distances (rigid scan). DFT calculations were performed with Gaussian, PBE0 functional, cc-pVTZ basis set.

$r_{\text{NN}}$ (Å)	$\Delta U_{\text{QM}}$ (kcal/mol)	$\Delta U_{\text{nb}}$ (kcal/mol)	$\Delta U_{\text{QM}} - \Delta U_{\text{nb}}$ (kcal/mol)	$\Delta U_{\text{str}}$ (kcal/mol)	$\Delta U_{\text{MM}}$ (kcal/mol)
1.2328	0.0812	0.0401	0.0411	0.0409	0.0810
1.2378	0.0200	0.0201	-0.0001	0.0005	0.0206
1.2428	0	0	0	0	0
1.2478	0.0197	-0.0202	0.0399	0.0394	0.0192
1.2528	0.0779	-0.0405	0.1184	0.1187	0.0781

Recalling (3.11) and (3.6), we can write

$$\begin{aligned} \Delta U_{\text{str}}(r_{ab}) &\equiv U_{\text{str}}(r_{ab}) - U_{\text{str}}(r_{ab\text{min}}) = \\ &= k_{ab} (r_{ab} - r_{ab0})^2 - U_{\text{str}}(r_{ab\text{min}}), \end{aligned} \quad (3.15)$$

$$k_{ab} (r_{ab} - r_{ab0})^2 - U_{\text{str}}(r_{ab\text{min}}) = \Delta U_{\text{QM}}(\mathbf{r}) - \Delta U_{\text{nb}}(\mathbf{r}) + \chi(\mathbf{r}). \quad (3.16)$$

Since we have unchanged atomic charges and LJ coefficients, the FF parameters to fit are simply  $k_{ab}$  and  $r_{ab0}$ .

Bonds parameters have been determined lengthening and shortening each bond distance (rigid scan) of 0.005, 0.01 and 0.02 Å. When it was not possible to alter one single bond distance without affecting any other degree of freedom, they were changed in appropriate combinations (*e.g.* in phenyl rings). Then, we calculated QM PE and all various MM PE contributions, subtracted nonbonded MM PE terms to QM PE, and minimized  $\chi^2$  through nonlinear least squares method.

### N–N bond

**DFT,  $S_0$  *trans* isomer.** DFT and MM calculations results are shown in Table 3.3.

Fitted parameters for N–N bond:

- $k_{\text{NN}} = (798 \pm 7) \text{ kcal mol}^{-1} \text{ \AA}^{-2}$  (SDRE = 0.82%)
- $r_{\text{NN}0} = (1.24033 \pm 0.00003) \text{ \AA}$  (SDRE = 0.0025%)

Fit RMSAE and RMSRE:

- RMSAE = 0.0004 kcal mol<sup>-1</sup>
- RMSRE = 0.93%

**Table 3.4:**  $S_0$  *trans* isomer MP2 PE and MM PE contributions computed for different N–N bond distances (rigid scan). MP2 calculations were performed with MOLCAS, ANO-L-VDZP basis set.

$r_{\text{NN}}$ (Å)	$\Delta U_{\text{QM}}$ (kcal/mol)	$\Delta U_{\text{nb}}$ (kcal/mol)	$\Delta U_{\text{QM}} - \Delta U_{\text{nb}}$ (kcal/mol)	$\Delta U_{\text{str}}$ (kcal/mol)	$\Delta U_{\text{MM}}$ (kcal/mol)
1.2612	0.2580	0.0698	0.1882	0.1865	0.2562
1.2712	0.0627	0.0351	0.0276	0.0315	0.0666
1.2812	0	0	0	0	0
1.2912	0.0602	-0.0355	0.0957	0.0920	0.0565
1.3012	0.2342	-0.0715	0.3057	0.3075	0.2360

**MP2,  $S_0$  *trans* isomer.** MP2 and MM calculations results are shown in Table 3.4.

Fitted parameters for N–N bond are:

- $k_{\text{NN}} = (617 \pm 11) \text{ kcal mol}^{-1} \text{ \AA}^{-2}$  (SDRE = 1.8 %)
- $r_{\text{NN}0} = (1.2788 \pm 0.0001) \text{ \AA}$  (SDRE = 0.0092 %)

Fit RMSAE and RMSRE:

- RMSAE = 0.003 kcal mol<sup>-1</sup>
- RMSRE = 2.2 %

**SS-CASPT2,  $S_1$  planar isomer.** SS-CASPT2 and MM calculations results are shown in Table 3.5.

Fitted parameters for N–N bond:

- $k_{\text{NN}} = (677 \pm 16) \text{ kcal mol}^{-1} \text{ \AA}^{-2}$  (SDRE = 2.3 %)
- $r_{\text{NN}0} = (1.2624 \pm 0.0001) \text{ \AA}$  (SDRE = 0.011 %)

Fit RMSAE and RMSRE:

- RMSAE = 0.004 kcal mol<sup>-1</sup>
- RMSRE = 2.7 %

In Figure 3.6 we show  $\Delta U_{\text{QM}} - \Delta U_{\text{nb}}$  and the fitted harmonic potential of the N–N bond as a function of  $r_{\text{NN}}$  for the  $S_0$  and the  $S_1$  electronic states. As we can observe, the bond equilibrium distance  $r_{\text{NN}0}$  decreases from the ground to the excited state, while the bond strength slightly increases (a higher value of  $k_{\text{NN}}$  produces a steeper parabola).

**Table 3.5:**  $S_1$  planar isomer SS-CASPT2 PE and MM PE contributions computed for different N–N bond distances (rigid scan). SS-CASPT2 calculations were performed with MOLCAS, ANO-L-VDZP basis set (active space: 16 orbitals, 18 electrons).

$r_{\text{NN}}$ (Å)	$\Delta U_{\text{QM}}$ (kcal/mol)	$\Delta U_{\text{nb}}$ (kcal/mol)	$\Delta U_{\text{QM}} - \Delta U_{\text{nb}}$ (kcal/mol)	$\Delta U_{\text{str}}$ (kcal/mol)	$\Delta U_{\text{MM}}$ (kcal/mol)
1.2436	0.2662	0.0249	0.2413	0.2393	0.2642
1.2536	0.0584	0.0125	0.0459	0.0519	0.0644
1.2636	0	0	0	0	0
1.2736	0.0754	-0.0124	0.0878	0.0834	0.0709
1.2836	0.2741	-0.0250	0.2991	0.3020	0.2771

**Table 3.6:**  $S_0$  *trans* isomer DFT PE and MM PE contributions computed with a rigid scan of C–N bond distance (C2-N1, see Figure 3.5 for AB atomic numbering). DFT calculations were performed with Gaussian, PBE0 functional, cc-pVTZ basis set.

$r_{\text{CN}}$ (Å)	$\Delta U_{\text{QM}}$ (kcal/mol)	$\Delta U_{\text{nb}}$ (kcal/mol)	$\Delta U_{\text{QM}} - \Delta U_{\text{nb}}$ (kcal/mol)	$\Delta U_{\text{str}}$ (kcal/mol)	$\Delta U_{\text{MM}}$ (kcal/mol)
1.4016	0.0401	0.0726	-0.0325	-0.0325	0.0401
1.4066	0.0099	0.0359	-0.0260	-0.0257	0.0102
1.4116	0	0	0	0	0
1.4166	0.0097	-0.0351	0.0448	0.0446	0.0095
1.4216	0.0384	-0.0694	0.1078	0.1080	0.0386

### C–N bond

**DFT,  $S_0$  *trans* isomer.** DFT and MM calculations results are shown in Table 3.6.

Fitted parameters for C–N bond:

- $k_{\text{CN}} = (377 \pm 3) \text{ kcal mol}^{-1} \text{ \AA}^{-2}$  (SDRE = 0.77 %)
- $r_{\text{CN}0} = (1.40230 \pm 0.00008) \text{ \AA}$  (SDRE = 0.0053 %)

Fit RMSAE and RMSRE:

- RMSAE = 0.0002 kcal mol<sup>-1</sup>
- RMSRE = 0.83 %

**MP2,  $S_0$  *trans* isomer.** MP2 and MM calculations results are shown in Table 3.7.

Fitted parameters for C–N bond:

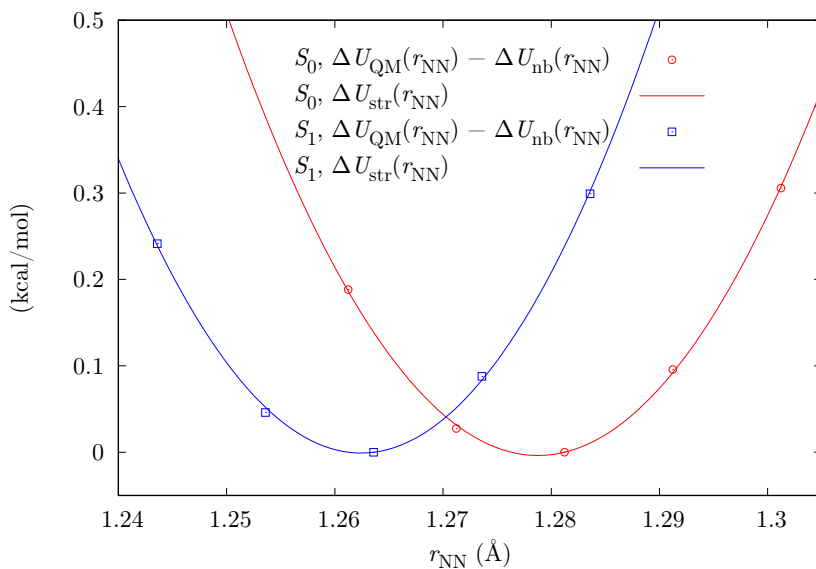


**Figure 3.6:** PE scan of  $r_{\text{NN}}$ . Potential energies for  $S_0$  and  $S_1$  states are normalized with respect to the one of the  $S_0$  *trans* isomer and the  $S_1$  planar isomer, respectively.

- $k_{\text{CN}} = (370 \pm 5) \text{ kcal mol}^{-1} \text{ \AA}^{-2}$  (SDRE = 1.4 %)
- $r_{\text{CN}0} = (1.4152 \pm 0.0002) \text{ \AA}$  (SDRE = 0.011 %)

Fit RMSAE and RMSRE:

- RMSAE = 0.001 kcal mol<sup>-1</sup>
- RMSRE = 1.6 %

**Table 3.7:**  $S_0$  *trans* isomer MP2 PE and MM PE contributions computed with a rigid scan of C–N bond distance (C2–N1, see Figure 3.5 for AB atomic numbering) (rigid scan). MP2 calculations were performed with MOLCAS, ANO-L-VDZP basis set.

$r_{\text{CN}}$ (Å)	$\Delta U_{\text{QM}}$ (kcal/mol)	$\Delta U_{\text{nb}}$ (kcal/mol)	$\Delta U_{\text{QM}} - \Delta U_{\text{nb}}$ (kcal/mol)	$\Delta U_{\text{str}}$ (kcal/mol)	$\Delta U_{\text{MM}}$ (kcal/mol)
1.4040	0.1582	0.1394	0.0188	0.0180	0.1574
1.4140	0.0380	0.0679	-0.0299	-0.0280	0.0399
1.4240	0	0	0	0	0
1.4340	0.0393	-0.0645	0.1038	0.1022	0.0377
1.4440	0.1516	-0.1260	0.2776	0.2785	0.1526

**Table 3.8:**  $S_1$  planar isomer SS-CASPT2 PE and MM PE contributions computed with a rigid scan of C–N bond distance (2-1, see Figure 3.5 for AB atomic numbering). SS-CASPT2 calculations were performed with MOLCAS, ANO-L-VDZP basis set (active space: 16 orbitals, 18 electrons).

$r_{\text{CN}}$ (Å)	$\Delta U_{\text{QM}}$ (kcal/mol)	$\Delta U_{\text{nb}}$ (kcal/mol)	$\Delta U_{\text{QM}} - \Delta U_{\text{nb}}$ (kcal/mol)	$\Delta U_{\text{str}}$ (kcal/mol)	$\Delta U_{\text{MM}}$ (kcal/mol)
1.3447	0.1841	0.0293	0.1548	0.1561	0.1853
1.3547	0.0434	0.0141	0.0293	0.0331	0.0472
1.3647	0	0	0	0	0
1.3747	0.0413	-0.0129	0.0542	0.0569	0.0439
1.3847	0.1768	-0.0249	0.2017	0.2037	0.1788

**SS-CASPT2,  $S_1$  planar isomer.** SS-CASPT2 and MM calculations results are shown in Table 3.8.

Fitted parameters for C–N bond:

- $k_{\text{CN}} = (450 \pm 5) \text{ kcal mol}^{-1} \text{ \AA}^{-2}$  (SDRE = 1.2 %)
- $r_{\text{CN}0} = (1.36335 \pm 0.00007) \text{ \AA}$  (SDRE = 0.0052 %)

Fit RMSAE and RMSRE:

- RMSAE = 0.02 kcal mol<sup>-1</sup>
- RMSRE = 2.5 %

### H–C bonds

Azobenzene presents ten H–C bonds; for symmetry reasons there are only three chemically different H–C bond types: *ortho*- H–C, *meta*- H–C, and *para*- H–C. Since their contribution is not particularly important for the scope of this work, we modeled them with a single set of parameters. Similarly to what we did for N–N and C–N bonds, we modified singularly each H–C bond. The resulting parameters were then averaged, weighting them according to the number of bonds of each type (one *para*- H–C bond, two *meta*- H–C bonds, two *ortho*- H–C bonds).

**DFT,  $S_0$  *trans* isomer.** DFT and MM calculations results are shown in Table 3.9.

Fitted parameters for *para*- H–C bond:

- $k_{p\text{-HC}} = (404 \pm 3) \text{ kcal mol}^{-1} \text{ \AA}^{-2}$  (SDRE = 0.62 %)
- $r_{p\text{-HC}0} = (1.08247 \pm 0.00002) \text{ \AA}$  (SDRE = 0.0018 %)

Fit RMSAE and RMSRE:

- RMSAE = 0.0002 kcal mol<sup>-1</sup>
- RMSRE = 0.89 %

Fitted parameters for *meta*- H–C bond:

- $k_{m\text{-HC}} = (403 \pm 3) \text{ kcal mol}^{-1} \text{ \AA}^{-2}$  (SDRE = 0.74 %)
- $r_{m\text{-HC}0} = (1.08236 \pm 0.00002) \text{ \AA}$  (SDRE = 0.0022 %)

Fit RMSAE and RMSRE:

- RMSAE = 0.0002 kcal mol<sup>-1</sup>
- RMSRE = 0.89 %

Fitted parameters for *ortho*- H–C bond:

- $k_{o\text{-HC}} = (412 \pm 2) \text{ kcal mol}^{-1} \text{ \AA}^{-2}$  (SDRE = 0.56 %)
- $r_{o\text{-HC}0} = (1.08291 \pm 0.00002) \text{ \AA}$  (SDRE = 0.0017 %)

Fit RMSAE and RMSRE:

- RMSAE = 0.0002 kcal mol<sup>-1</sup>
- RMSRE = 0.83 %

DFT and MM calculations results with averaged parameters are shown in Table 3.9.

Averaged parameters for H–C bonds:

- $k_{\text{HC}} = (407 \pm 4) \text{ kcal mol}^{-1} \text{ \AA}^{-2}$  (SDRE = 1.1 %)
- $r_{\text{HC}0} = (1.0826 \pm 0.0003) \text{ \AA}$  (SDRE = 0.026 %)

Overall fit RMSAE and RMSRE:

- RMSAE = 0.001 kcal mol<sup>-1</sup>
- RMSRE = 7.2 %

**Table 3.9:**  $S_0$  *trans* isomer DFT PE and MM PE contributions computed with a rigid scan of *para*-, *meta*- and *ortho*- H–C bond distances (H10-C5, H9-C4 and H8-C3; see Figure 3.5 for AB atomic numbering) bond distances. DFT calculations were performed with Gaussian, PBE0 functional, cc-pVTZ basis set.

$r_{p\text{-HC}}$ (Å)	$\Delta U_{\text{QM}}$ (kcal/mol)	$\Delta U_{\text{nb}}$ (kcal/mol)	$\Delta U_{\text{QM}} - \Delta U_{\text{nb}}$ (kcal/mol)	$\Delta U_{\text{str}}$ (kcal/mol)	$\Delta U_{\text{MM}}$ (kcal/mol)
1.0735	0.0411	0.0087	0.0324	0.0323	0.0410
1.0785	0.0101	0.0043	0.0058	0.0061	0.0104
1.0835	0	0	0	0	0
1.0885	0.0100	-0.0044	0.0144	0.0141	0.0097
1.0935	0.0396	-0.0088	0.0484	0.0485	0.0397
$r_{m\text{-HC}}$ (Å)	$\Delta U_{\text{QM}}$ (kcal/mol)	$\Delta U_{\text{nb}}$ (kcal/mol)	$\Delta U_{\text{QM}} - \Delta U_{\text{nb}}$ (kcal/mol)	$\Delta U_{\text{str}}$ (kcal/mol)	$\Delta U_{\text{MM}}$ (kcal/mol)
1.0736	0.0410	0.0110	0.0300	0.0299	0.0409
1.0787	0.0101	0.0055	0.0046	0.0049	0.0104
1.0837	0	0	0	0	0
1.0886	0.0099	-0.0056	0.0155	0.0153	0.0097
1.0937	0.0395	-0.0111	0.0506	0.0508	0.0396
$r_{o\text{-HC}}$ (Å)	$\Delta U_{\text{QM}}$ (kcal/mol)	$\Delta U_{\text{nb}}$ (kcal/mol)	$\Delta U_{\text{QM}} - \Delta U_{\text{nb}}$ (kcal/mol)	$\Delta U_{\text{str}}$ (kcal/mol)	$\Delta U_{\text{MM}}$ (kcal/mol)
1.0716	0.0418	-0.0099	0.0517	0.0516	0.0417
1.0766	0.0103	-0.0050	0.0153	0.0155	0.0106
1.0816	0	0	0	0	0
1.0866	0.0101	0.0049	0.0052	0.0051	0.0099
1.0916	0.0402	0.0097	0.0305	0.0307	0.0403

**Table 3.10:**  $S_0$  *trans* isomer DFT PE and MM PE contributions computed with a rigid scan of *para*-, *meta*- and *ortho*- H–C bond distances (H10-C5, H9-C4 and H8-C3; see Figure 3.5 for AB atomic numbering). DFT calculations were performed with Gaussian, PBE0 functional, cc-pVTZ basis set.

$r_{p\text{-HC}}$ (Å)	$\Delta U_{\text{QM}}$ (kcal/mol)	$\Delta U_{\text{nb}}$ (kcal/mol)	$\Delta U_{\text{QM}} - \Delta U_{\text{nb}}$ (kcal/mol)	$\Delta U_{\text{str}}$ (kcal/mol)	$\Delta U_{\text{MM}}$ (kcal/mol)
1.0735	0.0411	0.0087	0.0324	0.0336	0.0423
1.0785	0.0101	0.0043	0.0058	0.0067	0.0110
1.0835	0	0	0	0	0
1.0885	0.0100	-0.0044	0.0144	0.0137	0.0093
1.0935	0.0396	-0.0088	0.0484	0.0478	0.0390
$r_{m\text{-HC}}$ (Å)	$\Delta U_{\text{QM}}$ (kcal/mol)	$\Delta U_{\text{nb}}$ (kcal/mol)	$\Delta U_{\text{QM}} - \Delta U_{\text{nb}}$ (kcal/mol)	$\Delta U_{\text{str}}$ (kcal/mol)	$\Delta U_{\text{MM}}$ (kcal/mol)
1.0736	0.0410	0.0110	0.0300	0.0322	0.0432
1.0787	0.0101	0.0055	0.0046	0.0059	0.0114
1.0837	0	0	0	0	0
1.0886	0.0099	-0.0056	0.0155	0.0145	0.0089
1.0937	0.0395	-0.0111	0.0506	0.0492	0.0381
$r_{o\text{-HC}}$ (Å)	$\Delta U_{\text{QM}}$ (kcal/mol)	$\Delta U_{\text{nb}}$ (kcal/mol)	$\Delta U_{\text{QM}} - \Delta U_{\text{nb}}$ (kcal/mol)	$\Delta U_{\text{str}}$ (kcal/mol)	$\Delta U_{\text{MM}}$ (kcal/mol)
1.0716	0.0418	-0.0099	0.0517	0.0485	0.0385
1.0766	0.0103	-0.0050	0.0153	0.0141	0.0091
1.0816	0	0	0	0	0
1.0866	0.0101	0.0049	0.0052	0.0063	0.0111
1.0916	0.0402	0.0097	0.0305	0.0329	0.0425

**MP2,  $S_0$  *trans* isomer.** MP2 and MM calculations results are shown in Table 3.11.

Fitted parameters for *para*- H–C bond:

- $k_{p\text{-HC}} = (412 \pm 6) \text{ kcal mol}^{-1} \text{ \AA}^{-2}$  (SDRE = 1.4 %)
- $r_{p\text{-HC}0} = (1.09372 \pm 0.00008) \text{ \AA}$  (SDRE = 0.0074 %)

Fit RMSAE and RMSRE:

- RMSAE = 0.001 kcal mol<sup>-1</sup>
- RMSRE = 1.6 %

Fitted parameters for *meta*- H–C bond:

- $k_{m\text{-HC}} = (411 \pm 6) \text{ kcal mol}^{-1} \text{ \AA}^{-2}$  (SDRE = 1.4 %)
- $r_{m\text{-HC}0} = (1.09320 \pm 0.00008) \text{ \AA}$  (SDRE = 0.0075 %)

Fit RMSAE and RMSRE:

- RMSAE = 0.001 kcal mol<sup>-1</sup>
- RMSRE = 1.7 %

Fitted parameters for *ortho*- H–C bond:

- $k_{o\text{-HC}} = (413 \pm 5) \text{ kcal mol}^{-1} \text{ \AA}^{-2}$  (SDRE = 1.3 %)
- $r_{o\text{-HC}0} = (1.09606 \pm 0.00008) \text{ \AA}$  (SDRE = 0.0075 %)

Fit RMSAE and RMSRE:

- RMSAE = 0.001 kcal mol<sup>-1</sup>
- RMSRE = 1.6 %

MP2 and MM calculations results with averaged parameters are shown in Table 3.12.

Averaged parameters for H–C bonds:

- $k_{\text{HC}} = (412 \pm 7) \text{ kcal mol}^{-1} \text{ \AA}^{-2}$  (SDRE = 1.7 %)
- $r_{\text{HC}0} = (1.094 \pm 0.001) \text{ \AA}$  (SDRE = 0.14 %)

Overall fit RMSAE and RMSRE:

- RMSAE = 0.015 kcal mol<sup>-1</sup>
- RMSRE = 18 %

**Table 3.11:**  $S_0$  *trans* isomer MP2 PE and MM PE contributions computed with a rigid scan of *para*-, *meta*- and *ortho*- H–C bond distances (H10-C5, H9-C4 and H8-C3; see Figure 3.5 for AB atomic numbering). MP2 calculations were performed with MOLCAS, ANO-L-VDZP basis set.

$r_{p\text{-HC}}$ (Å)	$\Delta U_{\text{QM}}$ (kcal/mol)	$\Delta U_{\text{nb}}$ (kcal/mol)	$\Delta U_{\text{QM}} - \Delta U_{\text{nb}}$ (kcal/mol)	$\Delta U_{\text{str}}$ (kcal/mol)	$\Delta U_{\text{MM}}$ (kcal/mol)
1.0743	0.1709	0.0144	0.1565	0.1558	0.1702
1.0843	0.0419	0.0073	0.0346	0.0367	0.0439
1.0943	0	0	0	0	0
1.1043	0.0403	-0.0073	0.0476	0.0458	0.0386
1.1143	0.1584	-0.0146	0.1730	0.1741	0.1595
$r_{m\text{-HC}}$ (Å)	$\Delta U_{\text{QM}}$ (kcal/mol)	$\Delta U_{\text{nb}}$ (kcal/mol)	$\Delta U_{\text{QM}} - \Delta U_{\text{nb}}$ (kcal/mol)	$\Delta U_{\text{str}}$ (kcal/mol)	$\Delta U_{\text{MM}}$ (kcal/mol)
1.0744	0.1707	0.0254	0.1453	0.1446	0.1699
1.0844	0.0418	0.0127	0.0291	0.0312	0.0439
1.0944	0	0	0	0	0
1.1044	0.0404	-0.0127	0.0531	0.0512	0.0385
1.1144	0.1584	-0.0254	0.1838	0.1847	0.1593
$r_{o\text{-HC}}$ (Å)	$\Delta U_{\text{QM}}$ (kcal/mol)	$\Delta U_{\text{nb}}$ (kcal/mol)	$\Delta U_{\text{QM}} - \Delta U_{\text{nb}}$ (kcal/mol)	$\Delta U_{\text{str}}$ (kcal/mol)	$\Delta U_{\text{MM}}$ (kcal/mol)
1.0739	0.1712	-0.0299	0.2011	0.2002	0.1703
1.0839	0.0419	-0.0150	0.0569	0.0588	0.0439
1.0939	0	0	0	0	0
1.1039	0.0405	0.0150	0.0255	0.0239	0.0388
1.1139	0.1590	0.0298	0.1292	0.1303	0.1601

**Table 3.12:**  $S_0$  *trans* isomer MP2 PE and MM PE contributions computed with a rigid scan of *para*-, *meta*- and *ortho*- H–C bond distances (H10-C5, H9-C4 and H8-C3; see Figure 3.5 for AB atomic numbering). MP2 calculations were performed with MOLCAS, ANO-L-VDZP basis set.

$r_{p\text{-HC}}$ (Å)	$\Delta U_{\text{QM}}$ (kcal/mol)	$\Delta U_{\text{nb}}$ (kcal/mol)	$\Delta U_{\text{QM}} - \Delta U_{\text{nb}}$ (kcal/mol)	$\Delta U_{\text{str}}$ (kcal/mol)	$\Delta U_{\text{MM}}$ (kcal/mol)
1.0743	0.1709	0.0144	0.1565	0.1678	0.1822
1.0843	0.0419	0.0073	0.0346	0.0427	0.0499
1.0943	0	0	0	0	0
1.1043	0.0403	-0.0073	0.0476	0.0398	0.0325
1.1143	0.1584	-0.0146	0.1730	0.1620	0.1475
$r_{m\text{-HC}}$ (Å)	$\Delta U_{\text{QM}}$ (kcal/mol)	$\Delta U_{\text{nb}}$ (kcal/mol)	$\Delta U_{\text{QM}} - \Delta U_{\text{nb}}$ (kcal/mol)	$\Delta U_{\text{str}}$ (kcal/mol)	$\Delta U_{\text{MM}}$ (kcal/mol)
1.0744	0.1707	0.0254	0.1453	0.1654	0.1908
1.0844	0.0418	0.0127	0.0291	0.0415	0.0542
1.0944	0	0	0	0	0
1.1044	0.0404	-0.0127	0.0531	0.0410	0.0283
1.1144	0.1584	-0.0254	0.1838	0.1644	0.1390
$r_{o\text{-HC}}$ (Å)	$\Delta U_{\text{QM}}$ (kcal/mol)	$\Delta U_{\text{nb}}$ (kcal/mol)	$\Delta U_{\text{QM}} - \Delta U_{\text{nb}}$ (kcal/mol)	$\Delta U_{\text{str}}$ (kcal/mol)	$\Delta U_{\text{MM}}$ (kcal/mol)
1.0739	0.1712	-0.0299	0.2011	0.1733	0.1434
1.0839	0.0419	-0.0150	0.0569	0.0454	0.0305
1.0939	0	0	0	0	0
1.1039	0.0405	0.0150	0.0255	0.0371	0.0520
1.1139	0.1590	0.0298	0.1292	0.1566	0.1864

**SS-CASPT2,  $S_1$  planar isomer.** SS-CASPT2 and MM calculations results are shown in Table 3.13.

Fitted parameters for *para*- H–C bond:

- $k_{p\text{-HC}} = (419 \pm 6) \text{ kcal mol}^{-1} \text{ \AA}^{-2}$  (SDRE = 1.5 %)
- $r_{p\text{-HC}0} = (1.09204 \pm 0.00009) \text{ \AA}$  (SDRE = 0.0080 %)

Fit RMSAE and RMSRE:

- RMSAE = 0.001 kcal mol<sup>-1</sup>
- RMSRE = 1.7 %

Fitted parameters for *meta*- H–C bond:

- $k_{m\text{-HC}} = (416 \pm 6) \text{ kcal mol}^{-1} \text{ \AA}^{-2}$  (SDRE = 1.4 %)
- $r_{m\text{-HC}0} = (1.09259 \pm 0.00009) \text{ \AA}$  (SDRE = 0.0080 %)

Fit RMSAE and RMSRE:

- RMSAE = 0.001 kcal mol<sup>-1</sup>
- RMSRE = 1.7 %

Fitted parameters for *ortho*- H–C bond:

- $k_{o\text{-HC}} = (418 \pm 6) \text{ kcal mol}^{-1} \text{ \AA}^{-2}$  (SDRE = 1.4 %)
- $r_{o\text{-HC}0} = (1.09465 \pm 0.00009) \text{ \AA}$  (SDRE = 0.0078 %)

Fit RMSAE and RMSRE:

- RMSAE = 0.001 kcal mol<sup>-1</sup>
- RMSRE = 1.7 %

SS-CASPT2 and MM calculations results with averaged parameters are shown in Table 3.14.

Averaged parameters for H–C bonds:

- $k_{\text{HC}} = (417 \pm 7) \text{ kcal mol}^{-1} \text{ \AA}^{-2}$  (SDRE = 1.8 %)
- $r_{\text{HC}0} = (1.093 \pm 0.001) \text{ \AA}$  (SDRE = 0.11 %)

Overall fit RMSAE and RMSRE:

- RMSAE = 0.015 kcal mol<sup>-1</sup>
- RMSRE = 15 %

**Table 3.13:**  $S_1$  planar isomer SS-CASPT2 PE and MM PE contributions computed with a rigid scan of *para*-, *meta*- and *ortho*- H–C bond distances (H10-C5, H9-C4 and H8-C3; see Figure 3.5 for AB atomic numbering). SS-CASPT2 calculations were performed with MOLCAS, ANO-L-VDZP basis set (active space: 16 orbitals, 18 electrons).

$r_{p\text{-HC}}$ (Å)	$\Delta U_{\text{QM}}$ (kcal/mol)	$\Delta U_{\text{nb}}$ (kcal/mol)	$\Delta U_{\text{QM}} - \Delta U_{\text{nb}}$ (kcal/mol)	$\Delta U_{\text{str}}$ (kcal/mol)	$\Delta U_{\text{MM}}$ (kcal/mol)
1.0731	0.1666	0.0158	0.1508	0.1497	0.1653
1.0831	0.0391	0.0079	0.0312	0.0330	0.0408
1.0931	0	0	0	0	0
1.1031	0.0452	-0.0079	0.0531	0.0509	0.0429
1.1131	0.1688	-0.0158	0.1846	0.1855	0.1696
$r_{m\text{-HC}}$ (Å)	$\Delta U_{\text{QM}}$ (kcal/mol)	$\Delta U_{\text{nb}}$ (kcal/mol)	$\Delta U_{\text{QM}} - \Delta U_{\text{nb}}$ (kcal/mol)	$\Delta U_{\text{str}}$ (kcal/mol)	$\Delta U_{\text{MM}}$ (kcal/mol)
1.0744	0.1662	0.0296	0.1366	0.1354	0.1651
1.0844	0.0393	0.0148	0.0245	0.0261	0.0409
1.0944	0	0	0	0	0
1.1044	0.0444	-0.0148	0.0592	0.0570	0.0422
1.1144	0.1667	-0.0296	0.1963	0.1972	0.1675
$r_{o\text{-HC}}$ (Å)	$\Delta U_{\text{QM}}$ (kcal/mol)	$\Delta U_{\text{nb}}$ (kcal/mol)	$\Delta U_{\text{QM}} - \Delta U_{\text{nb}}$ (kcal/mol)	$\Delta U_{\text{str}}$ (kcal/mol)	$\Delta U_{\text{MM}}$ (kcal/mol)
1.0733	0.1656	-0.0252	0.1908	0.1896	0.1644
1.0833	0.0388	-0.0125	0.0513	0.0530	0.0405
1.0933	0	0	0	0	0
1.1033	0.0453	0.0126	0.0327	0.0306	0.0431
1.1133	0.1687	0.0249	0.1438	0.1448	0.1697

**Table 3.14:**  $S_1$  planar isomer SS-CASPT2 PE and MM PE contributions computed with a rigid scan of *para*-, *meta*- and *ortho*- H–C bond distances (H10-C5, H9-C4 and H8-C3; see Figure 3.5 for AB atomic numbering). SS-CASPT2 calculations were performed with MOLCAS, ANO-L-VDZP basis set (active space: 16 orbitals, 18 electrons).

$r_{p\text{-HC}}$ (Å)	$\Delta U_{\text{QM}}$ (kcal/mol)	$\Delta U_{\text{nb}}$ (kcal/mol)	$\Delta U_{\text{QM}} - \Delta U_{\text{nb}}$ (kcal/mol)	$\Delta U_{\text{str}}$ (kcal/mol)	$\Delta U_{\text{MM}}$ (kcal/mol)
1.0731	0.1666	0.0158	0.1508	0.1701	0.1859
1.0831	0.0391	0.0079	0.0312	0.0433	0.0512
1.0931	0	0	0	0	0
1.1031	0.0452	-0.0079	0.0531	0.0401	0.0323
1.1131	0.1688	-0.0158	0.1846	0.1637	0.1479
$r_{m\text{-HC}}$ (Å)	$\Delta U_{\text{QM}}$ (kcal/mol)	$\Delta U_{\text{nb}}$ (kcal/mol)	$\Delta U_{\text{QM}} - \Delta U_{\text{nb}}$ (kcal/mol)	$\Delta U_{\text{str}}$ (kcal/mol)	$\Delta U_{\text{MM}}$ (kcal/mol)
1.0744	0.1662	0.0296	0.1366	0.1478	0.1774
1.0844	0.0393	0.0148	0.0245	0.0322	0.0470
1.0944	0	0	0	0	0
1.1044	0.0444	-0.0148	0.0592	0.0513	0.0365
1.1144	0.1667	-0.0296	0.1963	0.1861	0.1564
$r_{o\text{-HC}}$ (Å)	$\Delta U_{\text{QM}}$ (kcal/mol)	$\Delta U_{\text{nb}}$ (kcal/mol)	$\Delta U_{\text{QM}} - \Delta U_{\text{nb}}$ (kcal/mol)	$\Delta U_{\text{str}}$ (kcal/mol)	$\Delta U_{\text{MM}}$ (kcal/mol)
1.0733	0.1656	-0.0252	0.1908	0.1668	0.1416
1.0833	0.0388	-0.0125	0.0513	0.0417	0.0291
1.0933	0	0	0	0	0
1.1033	0.0453	0.0126	0.0327	0.0418	0.0543
1.1133	0.1687	0.0249	0.1438	0.1671	0.1920

### C–C bonds

In the AB molecule there are twelve carbon atoms as many C–C bonds; for symmetry reasons, we can distinguish only four C atoms and three C–C bond types. In order to avoid a useless complication of the FF, we decided to keep the parameterization used in the work of Tiberio et al. [5] and consider just two type of C atoms (named CA and CD, as showed in Figure 3.7). Consequently, the C–C bond types to be parameterized are two: the CA–CD and the CD–CD. Since in a phenyl ring it is not possible to modify one single bond distance without affecting any other geometrical variable, we lengthened and shortened couples of C–C bond distances in opposite positions (C2–C3 and C5–C6, C3–C4 and C6–C7, C4–C5 and C7–C2), so as to vary the smallest number of degrees of freedom. Then, we calculated  $\Delta U_{\text{QM}}(\mathbf{r}) - \Delta U_{\text{nb}}(\mathbf{r})$  and minimized  $\chi^2$  using the Nelder-Mead method [50]. In this case, we can rewrite equation (3.7) as

$$\sum_{ab} k_{ab} (r_{ab} - r_{ab0})^2 - U_{\text{str}}(r_{ab\text{min}}) = \Delta U_{\text{QM}}(\mathbf{r}) - \Delta U_{\text{nb}}(\mathbf{r}) + \chi(\mathbf{r}), \quad (3.17)$$

where the indices  $ab$  run over the bonds whose distance has been modified case by case. Since at least a bond of the CD–CD type is always involved, we fitted simultaneously all the four parameters  $k_{\text{CACD}}$ ,  $k_{\text{CDCD}}$ ,  $r_{\text{CACD}0}$ ,  $r_{\text{CDCD}0}$ .

**MP2,  $S_0$  *trans* isomer.** MP2 and MM calculations results are shown in the tables from 3.15 to 3.17.

Fitted parameters for CA–CD bond type:

- $k_{\text{CACD}} = (593 \pm 15) \text{ kcal mol}^{-1} \text{ \AA}^{-2}$  (SDRE = 2.5 %)
- $r_{\text{CACD}0} = (1.416 \pm 0.003) \text{ \AA}$  (SDRE = 0.21 %)

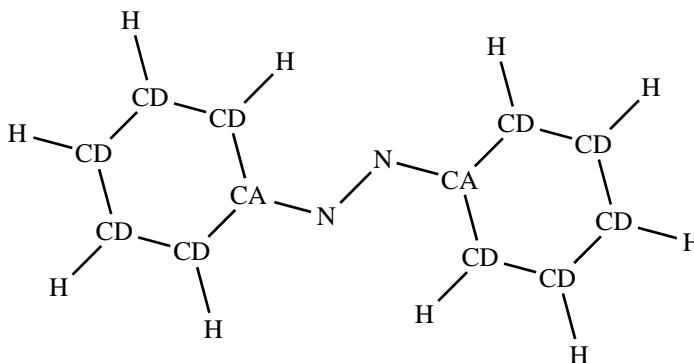


**Figure 3.7:** Azobenzene atom types used in this FF parameterization.

**Table 3.15:**  $S_0$  *trans* isomer MP2 PE and MM PE contributions computed with a rigid scan of couples of C2–C3 and C5–C6 bond distances (see Figure 3.5 for AB atomic numbering).

$r_{\text{C2C3}}$ $r_{\text{C5C6}}$ (Å)	$\Delta U_{\text{QM}}$ (kcal/mol)	$\Delta U_{\text{nb}}$ (kcal/mol)	$\Delta U_{\text{QM}} - \Delta U_{\text{nb}}$ (kcal/mol)	$\Delta U_{\text{str}}$ (kcal/mol)	$\Delta U_{\text{MM}}$ (kcal/mol)
1.3924 1.3891	0.4313	-0.0580	0.4893	0.4575	0.3993
1.4024 1.3991	0.1059	-0.0289	0.1348	0.1184	0.0893
1.4074 1.4041	0.0263	-0.0145	0.0408	0.0316	0.0171
1.4124 1.4091	0	0	0	0	0
1.4174 1.4141	0.0253	0.0145	0.0108	0.0235	0.0381
1.4224 1.4191	0.1011	0.0289	0.0722	0.1023	0.1314
1.4324 1.4291	0.3985	0.0578	0.3407	0.4253	0.4835

Fitted parameters for CD–CD bond type:

- $k_{\text{CDCD}} = (511 \pm 16) \text{ kcal mol}^{-1} \text{ \AA}^{-2}$  (SDRE = 3.1 %)
- $r_{\text{CDCD}0} = (1.405 \pm 0.004) \text{ \AA}$  (SDRE = 0.28 %)

Fit RMSAE and RMSRE:

- RMSAE =  $0.029 \text{ kcal mol}^{-1}$
- RMSRE = 19 %

**Table 3.16:**  $S_0$  *trans* isomer MP2 PE and MM PE contributions computed with a rigid scan of C3–C4 and C6–C7 bond distances (see Figure 3.5 for AB atomic numbering).

$r_{\text{C3C4}}$ $r_{\text{C6C7}}$ (Å)	$\Delta U_{\text{QM}}$ (kcal/mol)	$\Delta U_{\text{nb}}$ (kcal/mol)	$\Delta U_{\text{QM}} - \Delta U_{\text{nb}}$ (kcal/mol)	$\Delta U_{\text{str}}$ (kcal/mol)	$\Delta U_{\text{MM}}$ (kcal/mol)
1.3860	0.4431	-0.0276	0.4707	0.4455	0.4187
1.3824					
1.3960	0.1085	-0.0137	0.1222	0.1206	0.1073
1.3924					
1.4010	0.0267	-0.0068	0.0335	0.0347	0.0281
1.3974					
1.4060	0	0	0	0	0
1.4024					
1.4110	0.0266	0.0068	0.0198	0.0163	0.0230
1.4074					
1.4160	0.1053	0.0136	0.0917	0.0836	0.0970
1.4124					
1.4260	0.4128	0.0271	0.3857	0.3716	0.3981
1.4224					

**Table 3.17:**  $S_0$  *trans* isomer MP2 PE and MM PE contributions computed with a rigid scan of C4–C5 and C7–C2 bond distances (see Figure 3.5 for AB atomic numbering).

$r_{\text{C4C5}}$ $r_{\text{C7C2}}$ (Å)	$\Delta U_{\text{QM}}$ (kcal/mol)	$\Delta U_{\text{nb}}$ (kcal/mol)	$\Delta U_{\text{QM}} - \Delta U_{\text{nb}}$ (kcal/mol)	$\Delta U_{\text{str}}$ (kcal/mol)	$\Delta U_{\text{MM}}$ (kcal/mol)
1.3931	0.4269	0.0617	0.3652	0.4539	0.5154
1.3879					
1.4031	0.1048	0.0295	0.0753	0.1166	0.1459
1.3979					
1.4081	0.0261	0.0144	0.0117	0.0307	0.0451
1.4029					
1.4131	0	0	0	0	0
1.4079					
1.4181	0.0253	-0.0137	0.0390	0.0244	0.0109
1.4129					
1.4231	0.1004	-0.0268	0.1272	0.1041	0.0775
1.4179					
1.4331	0.3947	-0.0511	0.4458	0.4290	0.3783
1.4279					

**SS-CASPT2,  $S_1$  planar isomer.** RASSCF/SS-CASPT2 and MM calculations results are shown in the tables from 3.18 to 3.20.

Fitted parameters for CA–CD bond type:

- $k_{\text{CACD}} = (377 \pm 9) \text{ kcal mol}^{-1} \text{ \AA}^{-2}$  (SDRE = 2.4 %)
- $r_{\text{CACD}0} = (1.453 \pm 0.005) \text{ \AA}$  (SDRE = 0.25 %)

Fitted parameters for CD–CD bond type:

- $k_{\text{CDCD}} = (538 \pm 14) \text{ kcal mol}^{-1} \text{ \AA}^{-2}$  (SDRE = 2.6 %)
- $r_{\text{CDCD}0} = (1.400 \pm 0.005) \text{ \AA}$  (SDRE = 0.33 %)

Fit RMSAE and RMSRE:

- RMSAE =  $0.012 \text{ kcal mol}^{-1}$
- RMSRE = 8.2 %

**Table 3.18:**  $S_1$  planar isomer RASSCF/SS-CASPT2 PE and MM PE contributions computed with a rigid scan of couples of C2–C3 and C5–C6 bond distances (see Figure 3.5 for AB atomic numbering).

$r_{\text{C2C3}}$ $r_{\text{C5C6}}$ (Å)	$\Delta U_{\text{QM}}$ (kcal/mol)	$\Delta U_{\text{nb}}$ (kcal/mol)	$\Delta U_{\text{QM}} - \Delta U_{\text{nb}}$ (kcal/mol)	$\Delta U_{\text{str}}$ (kcal/mol)	$\Delta U_{\text{MM}}$ (kcal/mol)
1.4051	0.4033	-0.0739	0.4772	0.4868	0.4120
1.3942					
1.4151	0.1005	-0.0369	0.1374	0.1519	0.1146
1.4042					
1.4201	0.0258	-0.0184	0.0442	0.0531	0.0345
1.4092					
1.4251	0	0	0	0	0
1.4142					
1.4301	0.0208	0.0185	0.0023	-0.0073	0.0114
1.4192					
1.4351	0.0867	0.0369	0.0498	0.0311	0.0684
1.4242					
1.4451	0.3522	0.0737	0.2785	0.2451	0.3197
1.4342					

**Table 3.19:**  $S_1$  planar isomer RASSCF/SS-CASPT2 PE and MM PE contributions computed with a rigid scan of C3–C4 and C6–C7 bond distances (see Figure 3.5 for AB atomic numbering).

$r_{\text{C3C4}}$ $r_{\text{C6C7}}$ (Å)	$\Delta U_{\text{QM}}$ (kcal/mol)	$\Delta U_{\text{nb}}$ (kcal/mol)	$\Delta U_{\text{QM}} - \Delta U_{\text{nb}}$ (kcal/mol)	$\Delta U_{\text{str}}$ (kcal/mol)	$\Delta U_{\text{MM}}$ (kcal/mol)
1.3785	0.4547	-0.0323	0.4870	0.4871	0.4614
1.3792					
1.3885	0.1153	-0.0160	0.1313	0.1360	0.1232
1.3892					
1.3935	0.0309	-0.0079	0.0388	0.0411	0.0347
1.3942					
1.3985	0	0	0	0	0
1.3992					
1.4035	0.0226	0.0081	0.0145	0.0127	0.0192
1.4042					
1.4085	0.0959	0.0160	0.0799	0.0793	0.0921
1.4092					
1.4185	0.3951	0.0320	0.3631	0.3737	0.3993
1.4192					

**Table 3.20:**  $S_1$  planar isomer RASSCF/SS-CASPT2 PE and MM PE contributions computed with a rigid scan of C4–C5 and C7–C2 bond distances (see Figure 3.5 for AB atomic numbering).

$r_{\text{C4C5}}$ $r_{\text{C7C2}}$ (Å)	$\Delta U_{\text{QM}}$ (kcal/mol)	$\Delta U_{\text{nb}}$ (kcal/mol)	$\Delta U_{\text{QM}} - \Delta U_{\text{nb}}$ (kcal/mol)	$\Delta U_{\text{str}}$ (kcal/mol)	$\Delta U_{\text{MM}}$ (kcal/mol)
1.4103 1.3956	0.3718	-0.0341	0.4059	0.3783	0.3430
1.4203 1.4056	0.0865	-0.0175	0.1040	0.0977	0.0796
1.4253 1.4106	0.0194	-0.0089	0.0283	0.0260	0.0168
1.4303 1.4156	0	0	0	0	0
1.4353 1.4206	0.0262	0.0092	0.0170	0.0198	0.0292
1.4403 1.4256	0.0969	0.0186	0.0783	0.0853	0.1044
1.4503 1.4356	0.3669	0.0379	0.3290	0.3535	0.3926

### 3.2.4 Bending parameters

The 3-body angular bond potential describes the angular vibrational motion occurring between an  $(a, b, c)$ -triple of covalently bonded atoms, and has the form

$$U_{\text{bend}}(\vartheta_{abc}) = k_{abc} (\vartheta_{abc} - \vartheta_{abc0})^2, \quad (3.18)$$

where  $\vartheta_{abc}$  is the angle in radians between vectors  $\mathbf{r}_{ba} = \mathbf{r}_a - \mathbf{r}_b$  and  $\mathbf{r}_{bc} = \mathbf{r}_c - \mathbf{r}_b$ ,  $\vartheta_{abc0}$  is the equilibrium angle, and  $k_{abc}$  is the angle constant.

If it is possible to modify one single angle width  $\vartheta_{abc}$  without altering any other variable, as we have previously seen in paragraph 3.2.3, the only terms that will change in the expression of  $U_{\text{MM}}(\mathbf{r})$  are  $U_{\text{bend}}(\vartheta_{abc})$  and  $\sum U_{\text{nb}}(\mathbf{r})$ ; thus, rewriting the equation (3.7),

$$k_{abc} (\vartheta_{abc} - \vartheta_{abc0})^2 - U_{\text{bend}}(\vartheta_{abc\text{min}}) = \Delta U_{\text{QM}}(\mathbf{r}) - \Delta U_{\text{nb}}(\mathbf{r}) + \chi(\mathbf{r}). \quad (3.19)$$

Always keeping constant atomic charges and LJ coefficients, the FF parameters to fit are simply  $k_{abc}$  and  $\vartheta_{abc0}$ .

Unfortunately, except from  $\vartheta_{\text{CNN}}$  and  $\vartheta_{\text{NCC}}$  (whose parameterization will be discussed in a separate section), all the other angles can not be modified singularly. In order to modify the smallest number of variables, produced geometries by changing of  $\pm 0.5^\circ$ ,  $\pm 1^\circ$  and  $\pm 2^\circ$  appropriate combinations of angles (rigid scan). Then, we calculated  $\Delta U_{\text{QM}}(\mathbf{r}) - \Delta U_{\text{nb}}(\mathbf{r})$  and minimized  $\chi^2$  through the script cited in paragraph 3.2.3 (C–C bonds paragraph).

For simplicity, we will show only the detailed data for the derivation of the  $\vartheta_{\text{CCN}}$  bending angles parameters, since the procedure is almost identical to the one used for the C–C bonds parameterization.

#### C–C–N bending

In this case, an in-plane rotation of a phenyl ring around a CA-type atom (C2 or C14) allow to vary CD–CA–N angles only. Let us call  $\vartheta_{\text{CCN}}$  and  $\vartheta_{\text{NCC}}$  the two CD–CA–N bending angles and  $\vartheta_{\text{CCC}}$  the CD–CA–CD angle. If the rotation preserves the molecular planarity we get

$$\vartheta_{\text{CCN}} + \vartheta_{\text{NCC}} + \vartheta_{\text{CCC}} = 2\pi. \quad (3.20)$$

Since the parameters for the two C–C–N bending angles are the same, we can rewrite equation (3.7) as

$$\Delta U_{\text{bend}}(\vartheta_{\text{CCN}}) + \Delta U_{\text{bend}}(\vartheta_{\text{NCC}}) = \Delta U_{\text{QM}}(\mathbf{r}) - \Delta U_{\text{nb}}(\mathbf{r}) + \chi(\mathbf{r}), \quad (3.21)$$

$$k_{\text{CCN}} \left[ (\vartheta_{\text{CCN}} - \vartheta_{\text{CCN}0})^2 + (2\pi - \vartheta_{\text{CCC}} - \vartheta_{\text{CCN}} - \vartheta_{\text{CCN}0})^2 \right] + \\ - U_{\text{bend}}(\vartheta_{\text{CCN}\text{min}}, \vartheta_{\text{NCC}\text{min}}) = \Delta U_{\text{QM}}(\mathbf{r}) - \Delta U_{\text{nb}}(\mathbf{r}) + \chi(\mathbf{r}), \quad (3.22)$$

**Table 3.21:**  $S_0$  *trans* isomer MP2 PE and MM PE contributions computed with a rigid scan of two C–C–N bending angles (C3–C2–N1 and C7–C2–N1, see Figure 3.5 for AB atomic numbering).

$\vartheta_{\text{CCN}}$ ( $^\circ$ )	$\Delta U_{\text{QM}}$ (kcal/mol)	$\Delta U_{\text{nb}}$ (kcal/mol)	$\Delta U_{\text{QM}} - \Delta U_{\text{nb}}$ (kcal/mol)	$\Delta U_{\text{bend}}$ (kcal/mol)	$\Delta U_{\text{MM}}$ (kcal/mol)
111.76	0.4267	-0.5372	0.9639	0.9212	0.3842
112.76	0.1903	-0.3857	0.5760	0.5666	0.1810
113.76	0.0476	-0.2086	0.2562	0.2595	0.0510
114.26	0.0118	-0.1087	0.1205	0.1238	0.0152
114.76	0	0	0	0	0
115.26	0.0122	0.1185	-0.1063	-0.1120	0.0065
115.76	0.0488	0.2477	-0.1989	-0.2121	0.0357
116.76	0.1963	0.5438	-0.3475	-0.3766	0.1673
117.76	0.4448	0.8999	-0.4551	-0.4936	0.4063

where

$$U_{\text{bend}}(\vartheta_{\text{CCN min}}, \vartheta_{\text{NCC min}}) \equiv U_{\text{bend}}(\vartheta_{\text{CCN min}}) + U_{\text{bend}}(\vartheta_{\text{NCC min}}).$$

We noticed that the parameters  $k_{\text{CCN}}$  and  $\vartheta_{\text{CCN}0}$  showed a strong correlation and that the algorithm changed the value of  $k_{\text{CCN}}$  only, whatever the  $\vartheta_{\text{CCN}0}$  starting value was. Thus, we fixed  $\vartheta_{\text{CCN}0}$  at  $120^\circ$  and minimized  $\chi^2$  letting the algorithm change nothing but the  $k_{\text{CCN}}$  value.

**MP2,  $S_0$  *trans* isomer.** MP2 and MM calculations results are shown in Table 3.21.

Fitted parameters for C–C–N bending angle:

- $k_{\text{CCN}} = (39.0 \pm 0.7) \text{ kcal mol}^{-1} \text{ rad}^{-2}$  (SDRE = 1.8 %)
- $\vartheta_{\text{CCN}0} = 120.0^\circ$

Fit RMSAE and RMSRE:

- RMSAE =  $0.022 \text{ kcal mol}^{-1}$
- RMSRE = 15 %

**RASSCF/SS-CASPT2,  $S_1$  planar isomer.** RASSCF/SS-CASPT2 and MM calculations results are shown in Table 3.22.

Fitted parameters for C–C–N bending angle:

- $k_{\text{CCN}} = (43 \pm 3) \text{ kcal mol}^{-1} \text{ rad}^{-2}$  (SDRE = 6.1 %)

**Table 3.22:**  $S_1$  planar isomer RASSCF/SS-CASPT2 PE and MM PE contributions computed with a rigid scan of two C–C–N bending angles (C3–C2–N1 and C7–C2–N1, see Figure 3.5 for AB atomic numbering).

$\vartheta_{\text{CCN}}$ ( $^\circ$ )	$\Delta U_{\text{QM}}$ (kcal/mol)	$\Delta U_{\text{nb}}$ (kcal/mol)	$\Delta U_{\text{QM}} - \Delta U_{\text{nb}}$ (kcal/mol)	$\Delta U_{\text{bend}}$ (kcal/mol)	$\Delta U_{\text{MM}}$ (kcal/mol)
116.20	0.1852	-0.1202	0.3054	0.2882	0.1681
117.20	0.0527	-0.0656	0.1183	0.1177	0.0521
117.70	0.0164	-0.0343	0.0507	0.0522	0.0179
118.20	0	0	0	0	0
118.70	0.0051	0.0378	-0.0327	-0.0390	-0.0012
119.20	0.0308	0.0793	-0.0485	-0.0649	0.0145
120.20	0.1417	0.1754	-0.0337	-0.0769	0.0985

- $\vartheta_{\text{CCN}0} = 120.0^\circ$

Fit RMSAE and RMSRE:

- RMSAE = 0.019 kcal mol $^{-1}$
- RMSRE = 30 %

In Figure 3.8 we show  $\Delta U_{\text{QM}\mathbf{r}} - \Delta U_{\text{nb}\mathbf{r}}$  and the fitted harmonic potential of the C–C–N bending as a function of  $\vartheta_{\text{CCN}}$  for the  $S_0$  and the  $S_1$  electronic states. As we can observe, the force constant  $k_{\text{CCN}}$  is almost equal in the two cases, suggesting that this potential is not particularly involved in the excitation process. We encountered some problems in fitting this parameter, since the Lennard-Jones repulsion grows faster with the rotation of the phenyl ring.

### 3.2.5 Torsion parameters

The 4-body torsion angle (also known as dihedral angle) potential describes the angular spring between the planes formed by the first three and last three atoms of a consecutively bonded  $(a, b, c, d)$ -quadruple of atoms,

$$U_{\text{tors}}(\varphi_{abcd}) \equiv \begin{cases} \sum_n a_n [1 + \cos(n\varphi_{abcd} - \gamma_n)] & \text{if } n > 0 \\ a(\varphi_{abcd} - \gamma)^2 & \text{if } n = 0 \end{cases} \quad (3.23)$$

Bond stretching and angle bending can be considered stiff: during the motion, bond distances and bending angles remain in the neighborhood of the minimum energy geometry value, thus, a local sampling with a PE rigid scan is typically sufficient. Instead, dihedral angles can vary in the interval  $[0; 2\pi[$ , hence, a sampling of the whole interval is required. Furthermore, the

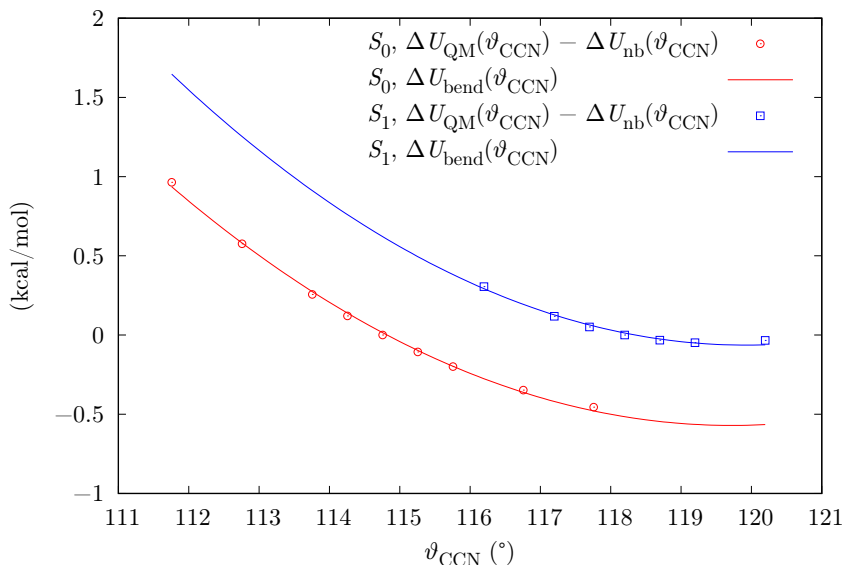


**Figure 3.8:** PE scan of  $\vartheta_{CCN}$ . Potential energies for  $S_0$  and  $S_1$  states are normalized with respect to the one of the  $S_0$  *trans* isomer and the  $S_1$  planar isomer, respectively.

explored conformations can differ dramatically from the minimum energy one, thus, a rigid scan could cause clashes of molecular fragments and give rise to high steric interactions. This is not correctly described by standard FFs, which do not factor in any charge redistribution or LJ coefficients variations and work properly only near the minimum energy conformation. A relaxed scan allow to avoid this problem, provided that all the parameters but those of the scanned dihedral angle are known.

For a relaxed scan of  $\varphi_{ijkl}$  dihedral angle, we get

$$\begin{aligned} \Delta U_{\text{tors}}(\varphi_{ijkl}) = & \Delta U_{\text{QM}}(\mathbf{r}) - \Delta U_{\text{nb}}(\mathbf{r}) - \Delta U_{\text{str}}(\mathbf{r}) + \\ & - \Delta U_{\text{bend}}(\mathbf{r}) - \sum_{\text{dih } abcd \neq ijkl} \Delta U_{\text{tors}}(\varphi_{abcd}) + \chi(\mathbf{r}), \quad (3.24) \end{aligned}$$

where

$$\begin{aligned} \Delta U_{\text{str}}(\mathbf{r}) &\equiv \sum_{\text{bond } ab} \Delta U_{\text{str}}(r_{ab}) \\ \Delta U_{\text{bend}}(\mathbf{r}) &\equiv \sum_{\text{ang } abc} \Delta U_{\text{bend}}(\vartheta_{abc}). \end{aligned} \quad (3.25)$$

### C–C–N–N torsion

Since the phenyl ring stays approximately planar during its rotation, the C–C–N–N dihedral angles to change are both C3–C2–N1–N13 and C7–

C2–N1–N13 (which we will name  $\varphi_{\text{CCNN}1}$  and  $\varphi_{\text{NNCC}1}$ , respectively), and

$$\varphi_{\text{CCNN}} + \varphi_{\text{NNCC}} \approx \pi. \quad (3.26)$$

Considering that we have not determined  $\vartheta_{\text{CNN}}$ ,  $\vartheta_{\text{NNC}}$  and  $\varphi_{\text{CNNC}}$  parameters yet, we can not apply equation (3.24) performing a full relaxed scan. Thus, we rotated one phenyl ring about the C–N axis and performed optimizations with multiple constraints, *i.e.*, keeping fixed  $\varphi_{\text{CCNN}1}$  and  $\varphi_{\text{NNCC}1}$  at the scan values,  $\varphi_{\text{CCNN}2}$  (C15–C14–N13–N1),  $\varphi_{\text{NNCC}2}$  (N1–N13–C14–C19),  $\vartheta_{\text{CNN}}$ ,  $\vartheta_{\text{NNC}}$  and  $\varphi_{\text{CNNC}}$  at the  $S_0$  *trans* isomer values). Then, we computed the same scan without the constraints on  $\varphi_{\text{CCNN}2}$ ,  $\varphi_{\text{NNCC}2}$ ,  $\vartheta_{\text{CNN}}$ ,  $\vartheta_{\text{NNC}}$  and  $\varphi_{\text{CNNC}}$ , in order to verify if these geometrical variables played an important role in one phenyl ring rotation or if their change could be actually neglected, and the calculations legitimized the approximation.

After the molecule relaxation, the conformation with  $\varphi_{\text{CCNN}} = 0$  and  $\varphi_{\text{NNCC}} = \pi$  is indistinguishable from that with  $\varphi_{\text{CCNN}} = \pi$  and  $\varphi_{\text{NNCC}} = 0$ , and so is the one with  $\varphi_{\text{CCNN}} = \pi/2$  and  $\varphi_{\text{NNCC}} = -\pi/2$  from the one with  $\varphi_{\text{CCNN}} = -\pi/2$  and  $\varphi_{\text{NNCC}} = \pi/2$ , so we can sample just in the interval  $[\pi/2; \pi]$  and must use the  $n$ -even terms of (3.23) only (except from  $n = 0$ , obviously). Therefore, from (3.7), we get

$$\begin{aligned} \Delta U_{\text{tors}}(\varphi_{\text{CCNN}}) + \Delta U_{\text{tors}}(\varphi_{\text{NNCC}}) = & \\ 2 \left\{ \sum_n a_{2n_{\text{CCNN}}} [1 + \cos(2n \varphi_{\text{CCNN}} - \gamma_{2n})] - U_{\text{tors}}(\varphi_{\text{CCNN}}) \right\} = & \\ \Delta U_{\text{QM}}(\mathbf{r}) - \Delta U_{\text{nb}}(\mathbf{r}) - \Delta U_{\text{str}}(\mathbf{r}) - \Delta U_{\text{bend}}(\mathbf{r}) + & \\ - \sum_{\text{dih } abcd \neq \text{CCNN, NNCC}} \Delta U_{\text{tors}}(\varphi_{abcd}) + \chi(\mathbf{r}), & \quad (3.27) \end{aligned}$$

where we used  $\cos(2n(\pi - \varphi)) = \cos(2n\varphi)$ . Phases  $\gamma_{2n}$  values are all  $\pi$ , since  $2n$  is even and the minimum energy conformation is at  $\varphi_{\text{CCNN}} = 0$  and  $\varphi_{\text{CCNN}} = \pi$ . The constants  $U_{\text{tors}}(\varphi_{\text{CCNN}_{\text{min}}})$  and  $U_{\text{tors}}(\varphi_{\text{NNCC}_{\text{min}}})$  do not appear in equation (3.27) because they are zero (since  $\varphi_{\text{CCNN}_{\text{min}}} = \pi$  and  $\varphi_{\text{NNCC}_{\text{min}}} = 0$ ).

After the QM calculations, we used the script cited in paragraph 3.2.3 to determine the parameters  $\{a_{2n_{\text{CCNN}}}\}$ . To obtain the various MM PE contributions we brought to zero the  $\varphi_{\text{CCNN}}$  parameters. MD simulation software support six cosine functions at most for each dihedral angle, thus, cosines we proved various combination of cosines until we reached the best result. In the case of the  $S_0$  FF, we used the first six even cosines, while in the case of the  $S_1$  fit, we use the first five even cosines.

**MP2,  $S_0$  *trans* isomer.** Structures were optimized at MP2 level. MP2 and MM calculations results are shown in Table 3.23.

**Table 3.23:**  $S_0$  *trans* isomer MP2 PE and MM PE computed with a semi-axed scan of two C–C–N–N dihedral angles (C3–C2–N1–N13 and C7–C2–N1–N13, see Figure 3.5 for AB atomic numbering).

$\varphi_{\text{CCNN}}$ ( $^\circ$ )	$\Delta U_{\text{QM}}$ (kcal/mol)	$\Delta U_{\text{MM}}$ (kcal/mol)
90	5.1355	5.1356
108	4.3754	4.3756
126	2.6032	2.6033
144	0.9614	0.9615
162	0.1675	0.1676
175	0.0107	0.0108
180	0	0

Fitted parameters for C–C–N–N dihedral angle (since  $\langle \chi^2(\mathbf{r}) \rangle$  were very small, algorithm could not compute the errors for the parameters):

- $a_{2\text{CCNN}} = 1.6068 \text{ kcal mol}^{-1}$
- $a_{4\text{CCNN}} = -0.10153 \text{ kcal mol}^{-1}$
- $a_{6\text{CCNN}} = -0.011158 \text{ kcal mol}^{-1}$
- $a_{8\text{CCNN}} = -2.9584 \times 10^{-3} \text{ kcal mol}^{-1}$
- $a_{10\text{CCNN}} = 3.1122 \times 10^{-4} \text{ kcal mol}^{-1}$
- $a_{12\text{CCNN}} = 4.6183 \times 10^{-3} \text{ kcal mol}^{-1}$

Fit RMSAE and RMSRE:

- RMSAE =  $3 \times 10^{-5} \text{ kcal mol}^{-1}$
- RMSRE = 0.0024 %

**RASSCF/SS-CASPT2,  $S_1$  planar isomer.** Since many geometrical optimizations at RASSCF/SS-CASPT2 level would have requested a big amount of CPU, we first optimized the molecular structures through TDDFT, and then calculated the RASSCF/SS-CASPT2 energy of each final geometry. RASSCF/SS-CASPT2 and MM calculations results are shown in Table 3.24. Note that the energies are always normalized with respect to the  $S_1$  planar isomer (where  $\varphi_{\text{CCNN}} = 180^\circ$ , which has been optimized at RASSCF/SS-CASPT2 level. This causes a shift of the other structures at higher energies, since they remarkably differ from  $S_1$  planar isomer (especially in bond distances). Also the fit RMSAE is larger than in the previous case for this reason, but still very small.

Fitted parameters for C–C–N–N dihedral angle:

**Table 3.24:**  $S_0$  *trans* isomer MP2 PE and MM PE computed with a semi-axed scan of two C–C–N–N dihedral angles (C3–C2–N1–N13 and C7–C2–N1–N13, see Figure 3.5 for AB atomic numbering).

$\varphi_{\text{CCNN}}$ ( $^\circ$ )	$\Delta U_{\text{QM}}$ (kcal/mol)	$\Delta U_{\text{MM}}$ (kcal/mol)
90	10.2394	10.2404
108	9.8935	9.8928
126	8.5969	8.5992
144	6.0973	6.0948
162	3.4171	3.4321
175	2.2451	2.1529
180	0	0

- $a_{2\text{CCNN}} = (2.07 \pm 0.02) \text{ kcal mol}^{-1}$
- $a_{4\text{CCNN}} = (0.35 \pm 0.02) \text{ kcal mol}^{-1}$
- $a_{6\text{CCNN}} = (0.032 \pm 0.018) \text{ kcal mol}^{-1}$
- $a_{8\text{CCNN}} = (0.021 \pm 0.017) \text{ kcal mol}^{-1}$
- $a_{10\text{CCNN}} = (0.015 \pm 0.014) \text{ kcal mol}^{-1}$

Fit RMSAE and RMSRE:

- RMSAE =  $0.03 \text{ kcal mol}^{-1}$
- RMSRE =  $0.61 \%$

### 3.2.6 Force Field Cross-terms

Differing types of terms in the energy expression may be added, deleted, or reformulated using the fit to the theoretical energy surface and its derivatives as criteria of physical importance.

The information contained in the quantum energy surfaces indicates that there is a significant anharmonicity, and that important intramolecular coupling interactions exist between internal degrees of freedom. The representation of the nature of these interactions, not present in diagonal, quadratic force fields (Class I force fields), such as AMBER and CHARMM, is important in describing accurately molecular energy surfaces [51]. Class II force fields derived from the quantum energy surfaces accounts for these important intramolecular force by adding cross-terms to the energy expressions and thus achieve more satisfactory results [52]. Indeed, the potential energy surfaces fit accuracy increases significantly by including these functions. Bond anharmonicity, angle anharmonicity, and bond-angle, bond-torsion, and angle-angle-torsion cross-term interactions result in the most

significant overall improvement in reproducing QM distorted structures energies [22].

Here we show some of the most relevant functions that represent the coupling terms cited above.

**Bond-bond cross-term** The bond-bond coupling describes the coupling between two stretching modes, and has the form

$$U_{ss}^{\text{II}}(r_{ab}, r_{bc}) \equiv k_{ss}^{\text{II}} (r_{ab} - r_{ab0}) (r_{bc} - r_{bc0}) , \quad (3.28)$$

where  $r_{ij0}$  is the same stretching equilibrium distance that appears in the harmonic stretching potential (see equation (3.11)). To a first approximation, it is considered only the interaction between two adjacent bonds involving atoms  $a$ ,  $b$  and  $c$ , but it can also be extended to bonds without any shared atom. The inclusion of this bond/bond coupling interaction is necessary for a force field to reproduce vibrational frequencies with high accuracy [46]. This coupling is particularly strong for bonds in systems with delocalized electrons.

**Bond-angle cross-term** The bond-angle cross-term describes the coupling between a stretching and a bending mode, and has the form

$$U_{sb}^{\text{II}}(r_{ab}, \vartheta_{abc}) \equiv k_{sb}^{\text{II}} (r_{ab} - r_{ab0}) (\vartheta_{abc} - \vartheta_{abc0}) , \quad (3.29)$$

where  $\vartheta_{abc0}$  is the same equilibrium bending angle that appears in the harmonic bending potential (see equation (3.18)). There are two of these terms for each angle (*i.e.*, one for each bond). Bond-angle coupling can be necessary to reproduce frequencies and several structural features. The neglect of coupling of an angle to other bonds (*i.e.*, different from the two that define the bond angle) is typically a good approximation [53], and this has been verified by fits of *ab initio* PESs.

**Angle-angle cross-term** The angle-angle cross-term describes the coupling between two bending modes, and has the form

$$U_{bb}^{\text{II}}(\vartheta_{abc}, \vartheta_{bcd}) \equiv k_{bb}^{\text{II}} (\vartheta_{abc} - \vartheta_{abc0}) (\vartheta_{bcd} - \vartheta_{bcd0}) , \quad (3.30)$$

Bending angles are coupled to other bending angles that share a common bond. It has been suggested that this term is relatively negligible for bending angles in tetracoordinate centers. The results obtained from the fit of the quantum energy surface, especially in molecules with large amounts of angle strain (*i.e.*, cyclopropane and methyl derivatives of cyclopropane), support the importance of the angle/angle coupling interactions [22].

**Bond-dihedral cross-term** The bond-dihedral cross-term describes the coupling between a stretching and a torsional mode, and has the form

$$U_{ts}^{\text{II}}(r_{ij}, \varphi_{abcd}) \equiv (\vartheta_{abc} - \vartheta_{abc0}) \sum_{n=1} a_{tsn}^{\text{II}} \cos(n \varphi_{abcd} - \gamma_n^{\text{II}}), \quad (3.31)$$

where  $ij = ab, bc$ . In fact, in this case there are two types of bond-dihedral cross-terms, because of there are two types of bonds for each dihedral angle: one central and two external. The fits of the alkane *ab initio* PES show the existence of the bond-torsion and bending-torsion coupling interactions, both for alkanes as well as acetals, carbohydrates, amides, and other functional groups [22].

**Angle-dihedral cross-term** The angle-dihedral cross-term describes the coupling between a bending and a torsional mode, and has the form

$$U_{tb}^{\text{II}}(\varphi_{abcd}, \vartheta_{abc}) \equiv (\vartheta_{abc} - \vartheta_{abc0}) \sum_{n=1} a_n^{\text{II}} \cos(n \varphi_{abcd} - \gamma_n^{\text{II}}). \quad (3.32)$$

Also in this case there are two possible bending angles for each dihedral angle. The bond-torsion and the bending-torsion coupling terms were found to reproduce the anomeric effect in acetals and carbohydrates or other functional groups, especially when a carbon atom separates two electronegative atoms [54].

**Angle-angle-dihedral cross-term**

$$\begin{aligned} U_{tb}^{\text{II}}(\varphi_{abcd}, \vartheta_{abc}, \vartheta_{bcd}) &\equiv \\ &\equiv (\vartheta_{abc} - \vartheta_{abc0}) (\vartheta_{bcd} - \vartheta_{bcd0}) \sum_{n=1} a_n^{\text{II}} \cos(n \varphi_{abcd} - \gamma_n^{\text{II}}). \end{aligned} \quad (3.33)$$

This coupling term, which was first introduced by Lifson and Warshel [55] was found to make a large contribution to the *ab initio* relative energies, forces and coupling derivatives in a lot of alkanes [22].

**C–N–N–C, C–N–N, N–N–C parameters**

We are interested in describing two electronic states simultaneously, *i.e.* we must be able to calculate the right  $S_0$  PE while the molecule moves near the  $S_1$  minimum (which is geometrically and energetically far from the  $S_0$  one) and vice versa. This requires a wider potential energy scan and implies the use of functions depending on several non-separable geometrical variables, since, as we explained in paragraph 3.2.6, the curvature of the potential energy surfaces along these displacement coordinates is hardly representable with harmonic functions of normal modes. Considering that it is not possible

to extend this kind of description to many variables, in this context, it has proved helpful to select the vibronic channels relevant for the dynamics and reserve this treatment for them only.

The *trans-cis* isomerization directly influences at least six internal degrees of freedom [56], namely: the C–N–N–C torsional dihedral angle ( $\varphi_{\text{CNNC}}$ ), the two C–N–N bending angles ( $\vartheta_{\text{CNN}}$  and  $\vartheta_{\text{NNC}}$ ), and C–N and N–N bond lengths ( $r_{\text{CN}}$  and  $r_{\text{NN}}$ ). Because of the increasing computational complexity associated with the use of potential energy hyper-surfaces (PES) depending on many non-separable variables, we limit here the additional FF cross-terms (see paragraph 3.2.6) only to the first three degrees of freedom cited.

As described in paragraph 3.2.5, when a torsional FF term has to be parameterized, a relaxed PE scan should be possibly performed, since the explored conformations can differ dramatically from the minimum energy one. This can give rise to high steric interactions, which are not correctly described by the classic model, which does not factor in any charge redistribution or LJ coefficients variations. Nevertheless, since computational time necessary for many optimizations at CASPT2 level would have been too high, again, we decided to perform rigid scans, merging the *trans*- and *cis*-potentials by keeping the lowest-energy structure for each geometry. What we did was a double 3D scan of  $\varphi_{\text{CNNC}}$  (from  $0^\circ$  to  $180^\circ$ ),  $\vartheta_{\text{CNN}}$  and  $\vartheta_{\text{NNC}}$  (both from  $100^\circ$  to  $160^\circ$ ) starting from  $S_0$  *trans* and *cis* isomer conformations. Then, we compared the two potential energies point by point and discarded, in the parameterization procedure, the one with the higher value. For large values of  $\varphi_{\text{CNNC}}$ ,  $\vartheta_{\text{CNN}}$  and  $\vartheta_{\text{NNC}}$ , we kept the PE of *trans*-isomer-derived geometries, while for small values, the *cis*-isomer-derived structures give a lower potential energy.

*Trans*- and *cis*-  $S_0$  and  $S_1$  potential energy as a function of  $\varphi_{\text{CNNC}}$  are shown in Figure 3.9 and Figure 3.10. As we can see in Figure 3.9, between  $50^\circ$  and  $70^\circ$ , both  $S_0$  and  $S_1$  *trans* and *cis* potential energies cross: for  $\vartheta_{\text{CNN}}, \vartheta_{\text{NNC}} = 112^\circ$  and  $\varphi_{\text{CNNC}} < 50^\circ$ , we kept *cis* PE scan points, while for  $\varphi_{\text{CNNC}} > 70^\circ$ , we kept *trans* PE scan ones.  $S_0$  and  $S_1$  *trans* PE steeply rises for  $\varphi_{\text{CNNC}} < 60^\circ$ : this is due to the fact that the two phenyl rings get extremely close to one another, as  $\varphi_{\text{CNNC}}$  decreases. This clash is avoided (or, actually, shifted to much smaller values of  $\varphi_{\text{CNNC}}$ ) when the molecule has the *cis* minimum energy conformation, in which the two  $\varphi_{\text{CCNN}}$  are  $128.6^\circ$  and  $55.6^\circ$ , instead of  $180^\circ$  and  $0^\circ$ . Indeed, in Figure 3.10, where the two bending angles are wider ( $\vartheta_{\text{CNN}} = \vartheta_{\text{NNC}} = 126^\circ$ ) we can observe that *trans-cis* PE crossing has moved to  $30^\circ$ - $50^\circ$  interval, since at those values of  $\varphi_{\text{CNNC}}$  the phenyl rings are farther apart.

We explained how we chose *cis* or *trans* PE using the minimum energy criterion, but we did not mention how we treated the points in the crossing region. We noted that *trans*-minimum-derived conformations near crossing region produce very strong LJ interactions, causing a way too steep surge in

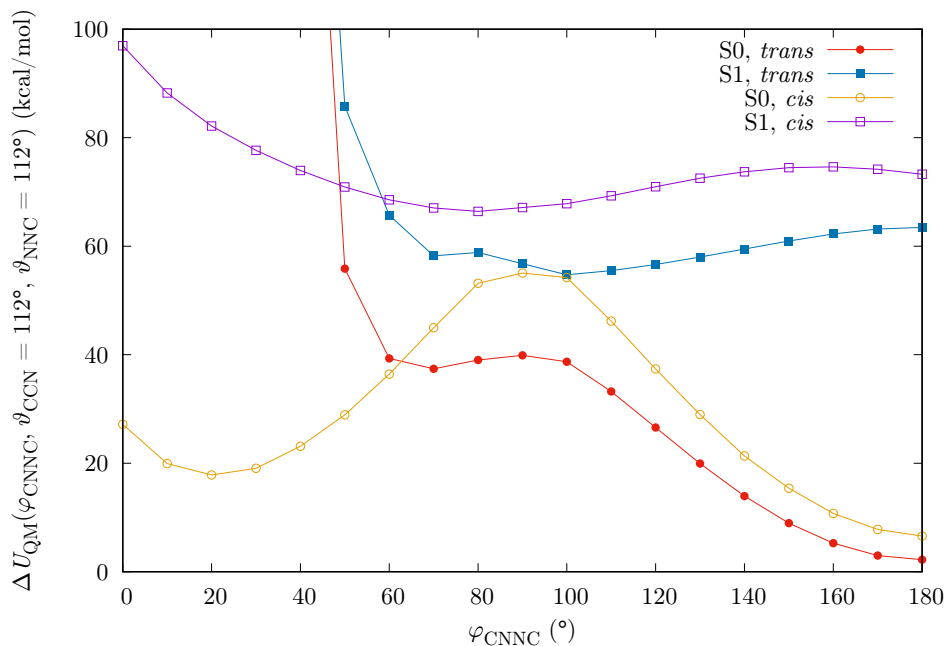


**Figure 3.9:** Total RASSCF/SS-CASPT2 energy ( $\Delta U_{\text{QM}}$ ) as a function of  $\varphi_{\text{CNNC}}$ , at  $\vartheta_{\text{CNN}}, \vartheta_{\text{NNC}} = 112^\circ$  (rigid scan). Remaining degrees of freedom were kept fixed and equal to  $S_0$  *trans* or *cis* minimum energy conformation ones.

$U_{\text{MM}}$  with respect to that observed in  $U_{\text{QM}}$ . This is incompatible with QM model and not reproducible with neither classical or class II FF functions. One of the assumptions of the Molecular Mechanics model that we use is that it must be possible to consider the electronic distribution (*i.e.* atomic charges and LJ parameters) as constant: in such molecular conformations, the small distance between the two phenyl rings, causes a non-negligible charge redistribution, which is taken into account in QM model, but not in MM one. Therefore, potential energies with high values of  $\Delta U_{\text{LJ}}$  cannot be taken into account. In Figure 3.11 and Figure 3.12 we see  $\Delta U_{\text{LJ}}$  as a function of  $\varphi_{\text{CNNC}}$ , at  $\vartheta_{\text{CNN}}, \vartheta_{\text{NNC}} = 112^\circ$  and  $\vartheta_{\text{CNN}}, \vartheta_{\text{NNC}} = 126^\circ$ , respectively. The phenyl rings clash can be identified with the hike in LJ PE.

As we did in previous paragraphs, we need to understand how to treat QM data to obtain the required FF parameters. Rewriting (3.7), we get

$$\begin{aligned}
 \Delta U_{\text{QM}}(\mathbf{r}) + \chi(\mathbf{r}) = & \sum_{\text{bond } ab} \Delta U_{\text{str}}(r_{ab}) + \sum_{\text{ang } abc \neq \text{CNN,NNC}} \Delta U_{\text{bend}}(\vartheta_{abc}) + \\
 & + \sum_{\text{dih } abcd \neq \text{CNNC}} \Delta U_{\text{tors}}(\varphi_{abcd}) + \Delta U_{\text{nb}}(\mathbf{r}) + \\
 & + \Delta U_{\text{tbb}}(\varphi_{\text{CNNC}}, \vartheta_{\text{CNN}}, \vartheta_{\text{NNC}}).
 \end{aligned} \tag{3.34}$$

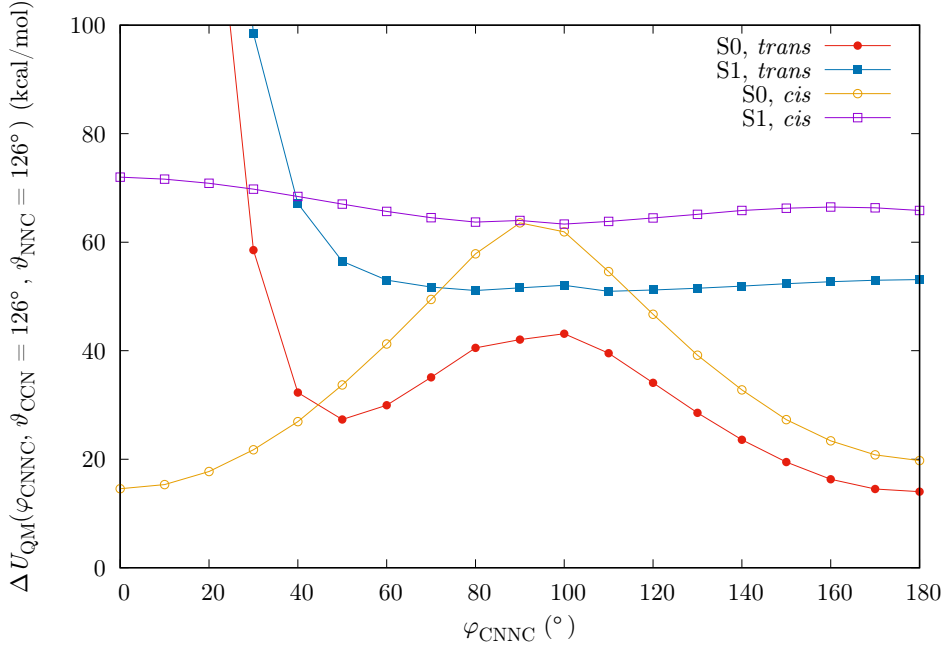


**Figure 3.10:** Total RASSCF/SS-CASPT2 energy ( $\Delta U_{\text{QM}}$ ) as a function of  $\varphi_{\text{CNNC}}$ , at  $\vartheta_{\text{CNN}}, \vartheta_{\text{NNC}} = 126^\circ$  (rigid scan). Remaining degrees of freedom were kept fixed and equal to  $S_0$  *trans* or *cis* minimum energy conformation ones.

where  $\Delta U_{\text{tbb}}(\varphi_{\text{CNNC}}, \vartheta_{\text{CNN}}, \vartheta_{\text{NNC}})$  is the PE contribution of the C–N–N and N–N–C bending and C–N–N–C torsion, normalized with respect to that of the minimum energy conformation:

$$\begin{aligned} \Delta U_{\text{tbb}}(\varphi_{\text{CNNC}}, \vartheta_{\text{CNN}}, \vartheta_{\text{NNC}}) &\equiv \\ &\equiv U_{\text{tbb}}(\varphi_{\text{CNNC}}, \vartheta_{\text{CNN}}, \vartheta_{\text{NNC}}) - U_{\text{tbb}}(\varphi_{\text{CNNC min}}, \vartheta_{\text{CNN min}}, \vartheta_{\text{NNC min}}). \end{aligned} \quad (3.35)$$

For the geometries obtained starting from the *trans* minimum structure ( $\mathbf{r}_{\text{min}}$ ), only  $\varphi_{\text{CNNC}}$ ,  $\vartheta_{\text{CNN}}$  and  $\vartheta_{\text{NNC}}$  were modified. As a consequence, the first three terms on the right-hand side of equation (3.34) are zero in such cases. Therefore, recalling definitions of (3.14), we get

$$\begin{aligned} U_{\text{tbb}}(\varphi_{\text{CNNC}}, \vartheta_{\text{CNN}}, \vartheta_{\text{NNC}}) - U_{\text{tbb}}(\varphi_{\text{CNNC min}}, \vartheta_{\text{CNN min}}, \vartheta_{\text{NNC min}}) &= \\ &= \Delta U_{\text{QM}}(\mathbf{r}) - \Delta U_{\text{nb}}(\mathbf{r}) + \chi(\mathbf{r}). \end{aligned} \quad (3.36)$$

On the other hand, the geometries obtained from the *cis* isomer differ from the *trans* minimum structure ( $\mathbf{r}_{\text{min}}$ ) in every degree of freedom. As a consequence, the first three terms on the right side of the equation (3.34) are constant, but not equal to zero and have to be calculated. Let us define  $\mathbf{r}_{\text{cis}}^*$  the ensemble of the variables that describe the minimum energy molecular geometry of azobenzene *cis* isomer, but with  $\vartheta_{\text{CNN cis}}^* = \vartheta_{\text{CNN min}}$ ,  $\vartheta_{\text{NNC cis}}^* =$

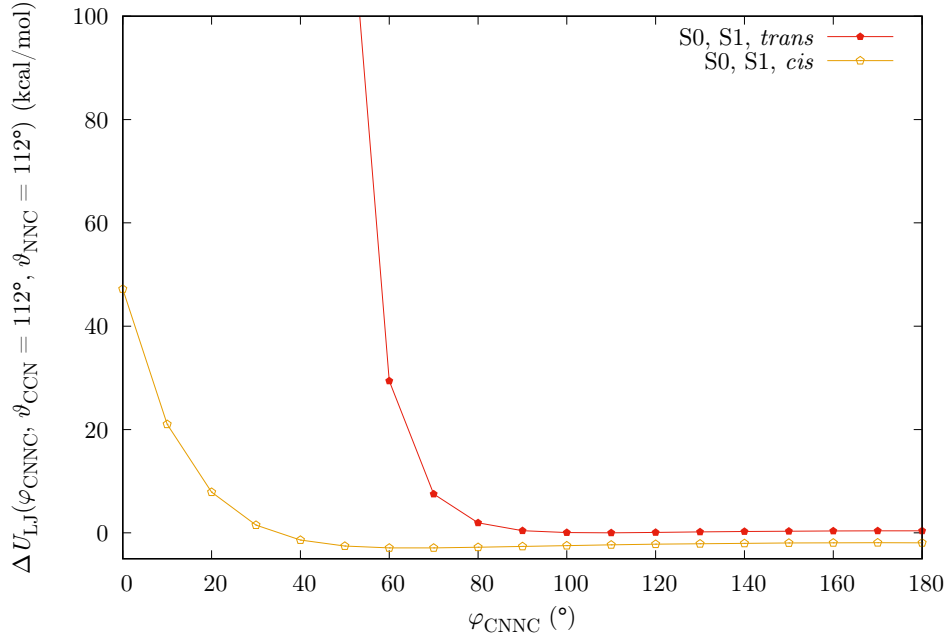


**Figure 3.11:**  $\Delta U_{\text{LJ}}$  as a function of  $\varphi_{\text{CNNC}}$ , at  $\vartheta_{\text{CNN}}, \vartheta_{\text{NNC}} = 112^\circ$  (rigid scan). The remaining degrees of freedom were kept fixed and equal to those of  $S_0$  *trans* or *cis* minimum energy conformations. Note that, since LJ coefficients of  $S_0$  and  $S_1$  FF are the same, so does  $\Delta U_{\text{LJ}}$ .

$\vartheta_{\text{NNC min}}$  and  $\varphi_{\text{CNNC cis}}^* = \varphi_{\text{CNNC min}}$ . If we consider the PE calculated for this particular conformation,  $\Delta U_{\text{tbb}}(\varphi_{\text{CNNC}}, \vartheta_{\text{CNN}}, \vartheta_{\text{NNC}})$  becomes zero, while the other terms can be easily obtained:

$$\begin{aligned} \sum_{\text{bond } ab} \Delta U_{\text{str}}(r_{ab}) &= \sum_{\text{bond } ab} \Delta U_{\text{str}}(r_{ab \text{ cis}}^*) \equiv \\ &\equiv \sum_{\text{bond } ab} U_{\text{str}}(r_{ab \text{ cis}}^*) - \sum_{\text{bond } ab} U_{\text{str}}(r_{ab \text{ min}}), \quad (3.37) \end{aligned}$$

$$\begin{aligned} \sum_{\text{ang } abc \neq \text{CNN, NNC}} \Delta U_{\text{bend}}(\vartheta_{abc}) &= \sum_{\text{ang } abc} \Delta U_{\text{bend}}(\vartheta_{abc \text{ cis}}^*) \equiv \\ &\equiv \sum_{\text{ang } abc} U_{\text{bend}}(\vartheta_{abc \text{ cis}}^*) - \sum_{\text{ang } abc} U_{\text{bend}}(\vartheta_{abc \text{ min}}), \quad (3.38) \end{aligned}$$

$$\begin{aligned} \sum_{\text{dih } abcd \neq \text{CNNC}} \Delta U_{\text{tors}}(\varphi_{abcd}) &= \sum_{\text{dih } abcd} \Delta U_{\text{tors}}(\varphi_{abcd \text{ cis}}^*) \equiv \\ &\equiv \sum_{\text{dih } abcd} U_{\text{tors}}(\varphi_{abcd \text{ cis}}^*) - \sum_{\text{dih } abcd} U_{\text{tors}}(\varphi_{abcd \text{ min}}), \quad (3.39) \end{aligned}$$

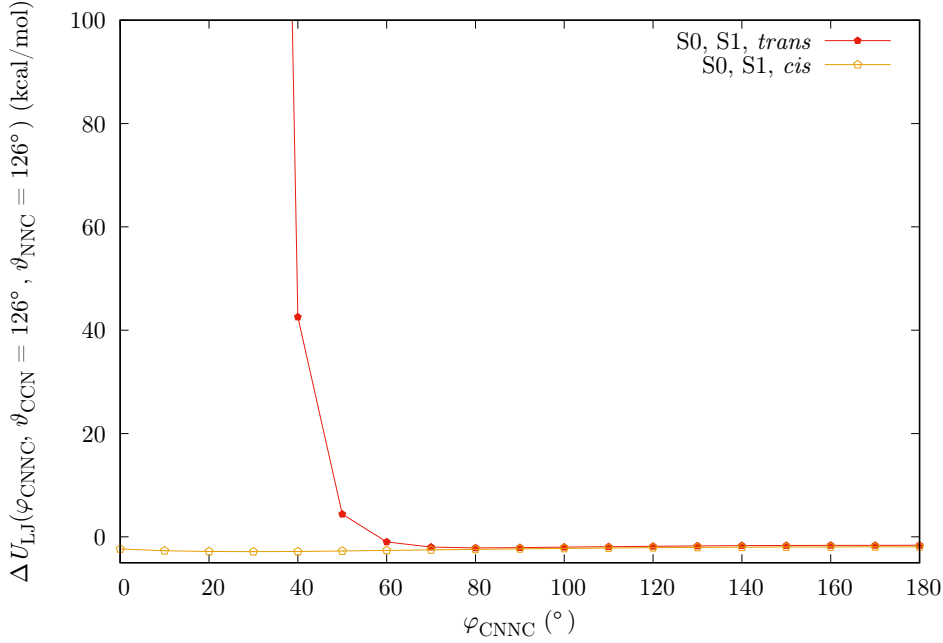


**Figure 3.12:**  $\Delta U_{\text{LJ}}$  as a function of  $\varphi_{\text{CNNC}}$ , at  $\vartheta_{\text{CNN}}, \vartheta_{\text{NNC}} = 126^{\circ}$  (rigid scan). The remaining degrees of freedom were kept fixed and equal to those of  $S_0$  *trans* or *cis* minimum energy conformations. Note that, since LJ coefficients of  $S_0$  and  $S_1$  FF are the same, so does  $\Delta U_{\text{LJ}}$ .

or, more concisely, recalling definition of (3.2), we can write

$$\begin{aligned} & \sum_{\text{bonds } ab} \Delta U_{\text{str}}(r_{ab}) + \sum_{\text{ang } abc \neq \text{CNN,NNC}} \Delta U_{\text{bend}}(\vartheta_{abc}) + \\ & + \sum_{\text{dih } abcd \neq \text{CNNC}} \Delta U_{\text{tors}}(\varphi_{abcd}) = \sum \Delta U_{\text{b}}(\mathbf{r}_{\text{cis}}^*) \equiv \Delta U_{\text{b}}(\mathbf{r}_{\text{cis}}^*). \end{aligned} \quad (3.40)$$

Thus, for the energies calculated starting from *cis* isomer minimum energy geometry, we obtain

$$\begin{aligned} U_{\text{tbb}}(\varphi_{\text{CNNC}}, \vartheta_{\text{CNN}}, \vartheta_{\text{NNC}}) - U_{\text{tbb}}(\varphi_{\text{CNNC min}}, \vartheta_{\text{CNN min}}, \vartheta_{\text{NNC min}}) = \\ = \Delta U_{\text{QM}}(\mathbf{r}) - \Delta U_{\text{nb}}(\mathbf{r}) - \Delta U_{\text{b}}(\mathbf{r}_{\text{cis}}^*) + \chi(\mathbf{r}). \end{aligned} \quad (3.41)$$

The function  $U_{\text{tbb}}(\varphi_{\text{CNNC}}, \vartheta_{\text{CNN}}, \vartheta_{\text{NNC}})$  used to approximate the potential energy (hyper)surface (PES) is a combination of class I FF and class II

FF functions:

$$\begin{aligned}
U_{\text{tbb}}(\varphi_{\text{CNNC}}, \vartheta_{\text{CNN}}, \vartheta_{\text{NNC}}) &\equiv \\
&\equiv \sum_{\text{ang } abc=\text{CNN,NNC}} U_{\text{bend}}(\vartheta_{abc}) + U_{\text{tors}}(\varphi_{\text{CNNC}}) + \\
&+ U_{\text{bb}}^{\text{II}}(\vartheta_{\text{CNN}}, \vartheta_{\text{NNC}}) + \sum_{\text{ang } abc=\text{CNN,NNC}} U_{\text{tb}}^{\text{II}}(\varphi_{\text{CNNC}}, \vartheta_{abc}). \quad (3.42)
\end{aligned}$$

where  $U_{\text{bend}}(\vartheta_{abc})$  and  $U_{\text{tors}}(\varphi_{\text{CNNC}})$ ,

$$U_{\text{bend}}(\vartheta_{abc}) \equiv k_{abc} (\vartheta_{abc} - \vartheta_{abc0})^2, \quad (3.43)$$

$$U_{\text{tors}}(\varphi_{\text{CNNC}}) \equiv \sum_{n=1}^6 a_n [1 + \cos(n \varphi_{\text{CNNC}} - \gamma_n)], \quad (3.44)$$

are classical FF functions, described in the !!!introductive section!!! and in the paragraphs 3.2.4 and 3.2.5, while  $U_{\text{bb}}^{\text{II}}(\vartheta_{\text{CNN}}, \vartheta_{\text{NNC}})$  and  $U_{\text{tb}}^{\text{II}}(\varphi_{\text{CNNC}}, \vartheta_{abc})$ ,

$$U_{\text{bb}}^{\text{II}}(\vartheta_{\text{CNN}}, \vartheta_{\text{NNC}}) \equiv k_{\text{bb}}^{\text{II}} (\vartheta_{\text{CNN}} - \vartheta_{\text{CNN}0}) (\vartheta_{\text{NNC}} - \vartheta_{\text{NNC}0}), \quad (3.45)$$

$$U_{\text{tb}}^{\text{II}}(\varphi_{\text{CNNC}}, \vartheta_{abc}) \equiv (\vartheta_{abc} - \vartheta_{abc0}) \sum_{n=1}^6 a_n^{\text{II}} \cos(n \varphi_{\text{CNNC}} - \gamma_n^{\text{II}}), \quad (3.46)$$

are class II FF cross-terms discussed in paragraph 3.2.6. Parameters  $k_{abc}$ ,  $\vartheta_{abc0}$ ,  $a_n$ ,  $k_{\text{bb}}^{\text{II}}$ ,  $a_n^{\text{II}}$  and  $U_{\text{tbb}}(\varphi_{\text{CNNC min}}, \vartheta_{\text{CNN min}}, \vartheta_{\text{NNC min}})$  (16, in total) were all fitted simultaneously, so as to obtain a more accurate approximation. Phases  $\gamma_n$  were determined by symmetry (0 for  $n$  odd,  $\pi$  for  $n$  even), while  $\gamma_n^{\text{II}}$  were kept fixed to 0, since their optimization did not improve the fit.

In the figures from 3.13 to 3.16 we see the reconstructed PES  $\Delta U_{\text{QM}} - \Delta U_{\text{nb}}$  and  $\Delta U_{\text{tbb}}$  with contour lines. Even though the regions with the points we discarded because of the high values of  $\Delta U_{\text{LJ}}$  are not empty but filled with interpolated values, these sketches are useful to evaluate more easily the precision of the approximation. As we can observe, the regions in which the function  $\Delta U_{\text{tbb}}$  differs most from  $\Delta U_{\text{QM}} - \Delta U_{\text{nb}}$  are those at small and high values of  $\vartheta_{\text{CNN}}$  and  $\vartheta_{\text{CNN}}$ . In the first case, when small values of bending angles are combined with small values of  $\varphi_{\text{CNNC}}$ , the difference is due to steric repulsion of phenyl rings, as discussed before. Also the neighborhood of the  $S_0$  *trans* minimum, which is shifted to smaller values of  $\vartheta_{\text{CNN}}$  and  $\vartheta_{\text{CNN}}$  (see paragraph ?? for a more detailed description) is not well reproduced. In regions at high bending angles values we can see a sharp change in the gradient for both the  $S_0$  and  $S_1$  PES. This is caused by the fact that there are high energy conical intersections and the two states cross. This trend can not be reproduced by our kind of functions and so those points were not used for the fit. This should not be a problem, since

**Table 3.25:**  $U_{\text{tbb}}(\varphi_{\text{CNNC}}, \vartheta_{\text{CNN}}, \vartheta_{\text{NNC}})$  parameters values and relative uncertainties, fitted on  $S_0$  PES  $\Delta U_{\text{QM}}(\varphi_{\text{CNNC}}, \vartheta_{\text{CNN}}, \vartheta_{\text{NNC}}) - \Delta U_{\text{nb}}(\varphi_{\text{CNNC}}, \vartheta_{\text{CNN}}, \vartheta_{\text{NNC}})$  (rigid scan).

Parameter	Value	SDAE	Unit of measurement	SDRE (%)
$k_{abc}$	42.6	17.0	$\text{kcal mol}^{-1} \text{rad}^{-2}$	39.9
$\vartheta_{abc0}$	110.8	22.2	degrees	20.0
$a_1$	0.00164	0.00023	$\text{kcal mol}^{-1}$	14.0
$a_2$	19.2	3.2	$\text{kcal mol}^{-1}$	16.5
$a_3$	-1.24	0.17	$\text{kcal mol}^{-1}$	13.6
$a_4$	-1.05	0.14	$\text{kcal mol}^{-1}$	13.3
$a_5$	0.134	0.020	$\text{kcal mol}^{-1}$	15.1
$a_6$	0.374	0.039	$\text{kcal mol}^{-1}$	10.5
$k_{\text{bb}}^{\text{II}}$	20.2	10.3	$\text{kcal mol}^{-1} \text{rad}^{-2}$	51.0
$a_1^{\text{II}}$	-5.18	0.87	$\text{kcal mol}^{-1} \text{rad}^{-1}$	16.8
$a_2^{\text{II}}$	11.6	1.8	$\text{kcal mol}^{-1} \text{rad}^{-1}$	15.4
$a_3^{\text{II}}$	1.85	0.29	$\text{kcal mol}^{-1} \text{rad}^{-1}$	15.7
$a_4^{\text{II}}$	0.083	0.013	$\text{kcal mol}^{-1} \text{rad}^{-1}$	15.7
$a_5^{\text{II}}$	-0.468	0.080	$\text{kcal mol}^{-1} \text{rad}^{-1}$	17.2
$a_6^{\text{II}}$	-0.0159	0.0019	$\text{kcal mol}^{-1} \text{rad}^{-1}$	12.2
$U_{\text{tbb min}}$	1.56	0.47	$\text{kcal mol}^{-1}$	30.1

the FC point on  $S_1$  is at a smaller value of PE and that region should not be accessible.

In the  $S_1$  QM PES we can note a double well in the region at  $\varphi_{\text{CNNC}} = 90^\circ$  and asymmetric bending angles (Figure 3.15c). Clearly, the function  $\Delta U_{\text{tbb}}$  does not account for a similar behaviour, and “smooths” them producing a unique well in the midpoint between the two (Figure 3.15d). This could be an important difference, and we will have to verify if the simulation trajectories can explore the whole region anyway or if it is visited the neighborhood of the minimum. Considering that the  $S_1$  PES is rather flat (the barrier height separating the two potential wells is less than  $5 \text{ kcal mol}^{-1}$ ), this could be possible.

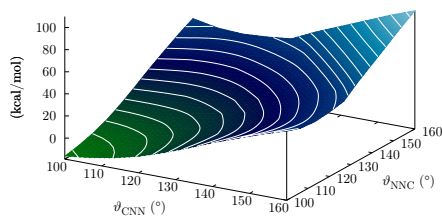
The fitted parameters of  $U_{\text{tbb}}(\varphi_{\text{CNNC}}, \vartheta_{\text{CNN}}, \vartheta_{\text{NNC}})$  are shown in Table 3.25 and Table 3.26.

- Fit RMSAE and RMSRE for  $S_0$  PES:

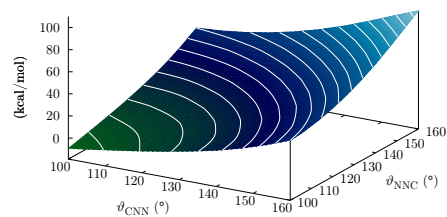
- RMSAE =  $2.93 \text{ kcal mol}^{-1}$
- RMSRE = 7.01 %

- Fit RMSAE and RMSRE for  $S_1$  PES:

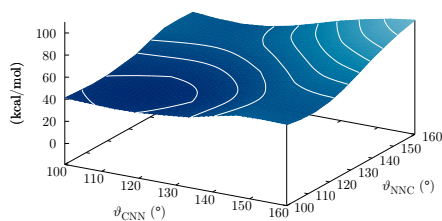
- RMSAE =  $1.67 \text{ kcal mol}^{-1}$
- RMSRE = 10.9 %



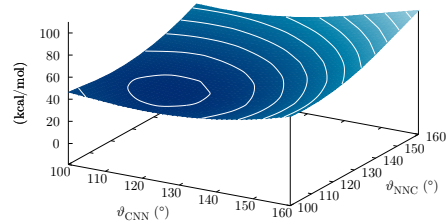
(a)  $\Delta U_{\text{QM}} - \Delta U_{\text{nb}}$   
 $(\varphi_{\text{CNNC}} = 10^\circ, \vartheta_{\text{CNN}}, \vartheta_{\text{NNC}})$



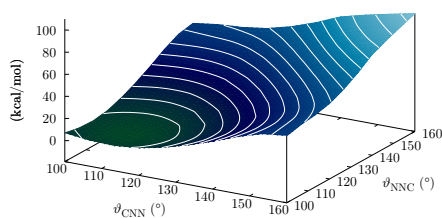
(b)  $\Delta U_{\text{ttb}}$   
 $(\varphi_{\text{CNNC}} = 10^\circ, \vartheta_{\text{CNN}}, \vartheta_{\text{NNC}})$



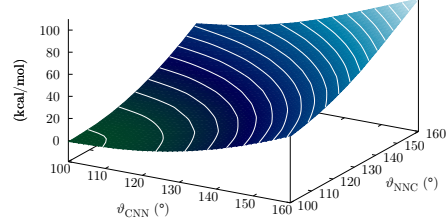
(c)  $\Delta U_{\text{QM}} - \Delta U_{\text{nb}}$   
 $(\varphi_{\text{CNNC}} = 90^\circ, \vartheta_{\text{CNN}}, \vartheta_{\text{NNC}})$



(d)  $\Delta U_{\text{ttb}}$   
 $(\varphi_{\text{CNNC}} = 90^\circ, \vartheta_{\text{CNN}}, \vartheta_{\text{NNC}})$



(e)  $\Delta U_{\text{QM}} - \Delta U_{\text{nb}}$   
 $(\varphi_{\text{CNNC}} = 180^\circ, \vartheta_{\text{CNN}}, \vartheta_{\text{NNC}})$



(f)  $\Delta U_{\text{ttb}}$   
 $(\varphi_{\text{CNNC}} = 180^\circ, \vartheta_{\text{CNN}}, \vartheta_{\text{NNC}})$

**Figure 3.13:** Sections of reconstructed  $S_0$  PES. From top to bottom:  $\Delta U_{\text{QM}} - \Delta U_{\text{nb}}$  (left) and  $\Delta U_{\text{ttb}}$  (right) as a function of  $\vartheta_{\text{CNN}}$  and  $\vartheta_{\text{NNC}}$  at  $\varphi_{\text{CNNC}} = 10^\circ, 90^\circ, 180^\circ$ .

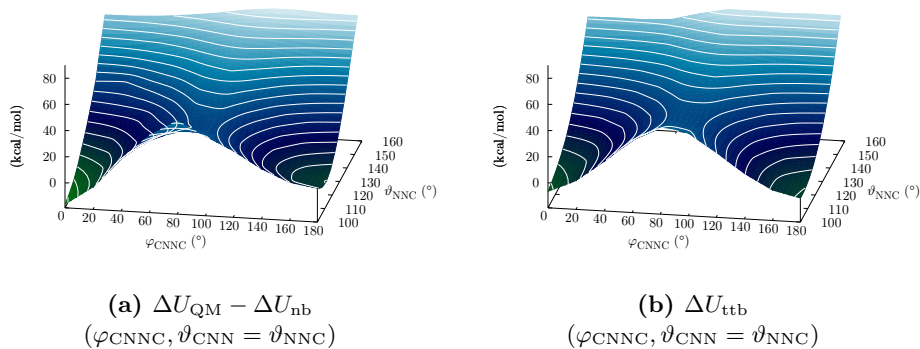
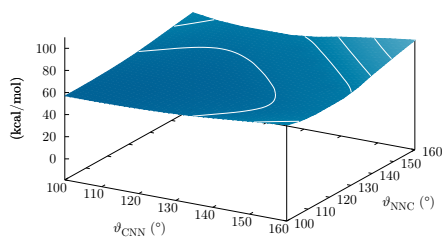


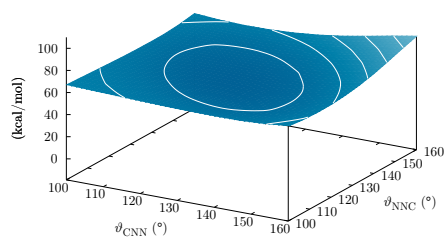
**Figure 3.14:** Sections of reconstructed  $S_0$  PES.  $\Delta U_{\text{QM}} - \Delta U_{\text{nb}}$  (left) and  $\Delta U_{\text{ttb}}$  (right) as a function of  $\varphi_{\text{CNNC}}$  and  $\vartheta_{\text{NNC}}$  with symmetric bending angles ( $\vartheta_{\text{CNN}} = \vartheta_{\text{NNC}}$ ).

**Table 3.26:**  $U_{\text{ttb}}(\varphi_{\text{CNNC}}, \vartheta_{\text{CNN}}, \vartheta_{\text{NNC}})$  parameters values and relative uncertainties, fitted on  $S_1$  PES  $\Delta U_{\text{QM}}(\varphi_{\text{CNNC}}, \vartheta_{\text{CNN}}, \vartheta_{\text{NNC}}) - \Delta U_{\text{nb}}(\varphi_{\text{CNNC}}, \vartheta_{\text{CNN}}, \vartheta_{\text{NNC}})$  (rigid scan).

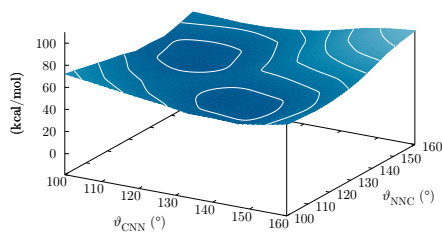
Parameter	Value	SDAE	Unit of measurement	SDRE (%)
$k_{abc}$	34.9	8.3	$\text{kcal mol}^{-1} \text{rad}^{-2}$	23.9
$\vartheta_{abc0}$	125.0	6.0	degrees	4.9
$a_1$	0.1287	0.0063	$\text{kcal mol}^{-1}$	4.9
$a_2$	-1.524	0.064	$\text{kcal mol}^{-1}$	4.2
$a_3$	0.481	0.022	$\text{kcal mol}^{-1}$	4.6
$a_4$	-0.619	0.028	$\text{kcal mol}^{-1}$	4.6
$a_5$	0.512	0.027	$\text{kcal mol}^{-1}$	5.2
$a_6$	0.0329	0.0012	$\text{kcal mol}^{-1}$	3.6
$k_{\text{bb}}^{\text{II}}$	31.1	9.7	$\text{kcal mol}^{-1} \text{rad}^{-2}$	31.2
$a_1^{\text{II}}$	-0.887	0.090	$\text{kcal mol}^{-1} \text{rad}^{-1}$	10.1
$a_2^{\text{II}}$	-3.29	0.31	$\text{kcal mol}^{-1} \text{rad}^{-1}$	9.5
$a_3^{\text{II}}$	-0.995	0.095	$\text{kcal mol}^{-1} \text{rad}^{-1}$	9.5
$a_4^{\text{II}}$	-2.56	0.24	$\text{kcal mol}^{-1} \text{rad}^{-1}$	9.5
$a_5^{\text{II}}$	-0.300	0.031	$\text{kcal mol}^{-1} \text{rad}^{-1}$	10.4
$a_6^{\text{II}}$	0.811	0.059	$\text{kcal mol}^{-1} \text{rad}^{-1}$	7.3
$U_{\text{ttb min}}$	54.9	5.3	$\text{kcal mol}^{-1}$	9.6



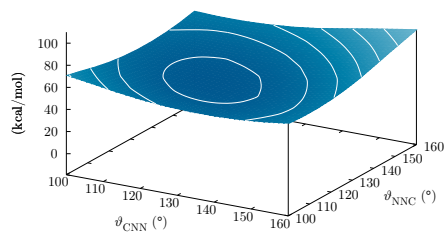
(a)  $\Delta U_{\text{QM}} - \Delta U_{\text{nb}}$   
( $\varphi_{\text{C}^{\text{NNC}}} = 10^\circ, \vartheta_{\text{CNN}}, \vartheta_{\text{NNC}}$ )



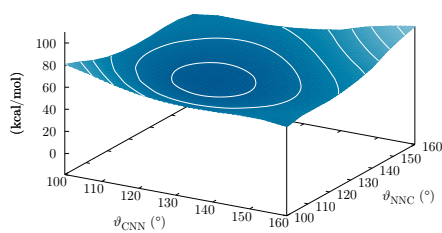
(b)  $\Delta U_{\text{ttb}}$   
( $\varphi_{\text{C}^{\text{NNC}}} = 10^\circ, \vartheta_{\text{CNN}}, \vartheta_{\text{NNC}}$ )



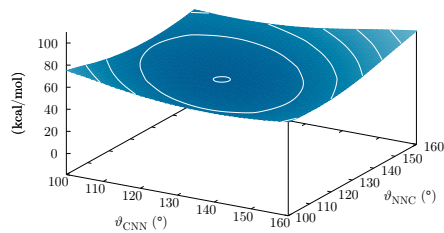
(c)  $\Delta U_{\text{QM}} - \Delta U_{\text{nb}}$   
( $\varphi_{\text{C}^{\text{NNC}}} = 90^\circ, \vartheta_{\text{CNN}}, \vartheta_{\text{NNC}}$ )



(d)  $\Delta U_{\text{ttb}}$   
( $\varphi_{\text{C}^{\text{NNC}}} = 90^\circ, \vartheta_{\text{CNN}}, \vartheta_{\text{NNC}}$ )



(e)  $\Delta U_{\text{QM}} - \Delta U_{\text{nb}}$   
( $\varphi_{\text{C}^{\text{NNC}}} = 180^\circ, \vartheta_{\text{CNN}}, \vartheta_{\text{NNC}}$ )



(f)  $\Delta U_{\text{ttb}}$   
( $\varphi_{\text{C}^{\text{NNC}}} = 180^\circ, \vartheta_{\text{CNN}}, \vartheta_{\text{NNC}}$ )

**Figure 3.15:** Sections of reconstructed  $S_1$  PES. From top to bottom:  $\Delta U_{\text{QM}} - \Delta U_{\text{nb}}$  (left) and  $\Delta U_{\text{ttb}}$  (right) as a function of  $\vartheta_{\text{CNN}}$  and  $\vartheta_{\text{NNC}}$  at  $\varphi_{\text{C}^{\text{NNC}}} = 10^\circ, 90^\circ, 180^\circ$ .

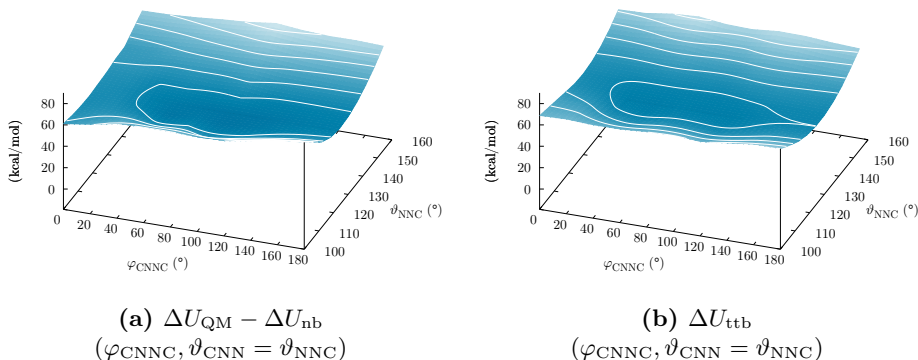


**Figure 3.16:** Sections of reconstructed  $S_1$  PES.  $\Delta U_{\text{QM}} - \Delta U_{\text{nb}}$  (left) and  $\Delta U_{\text{ttb}}$  (right) as a function of  $\varphi_{\text{CNNC}}$  and  $\vartheta_{\text{NNC}}$  with symmetric bending angles ( $\vartheta_{\text{CNN}} = \vartheta_{\text{NNC}}$ ).

The values of parameters SDAE and SDRE and fit RMSAE and RMSRE, although still acceptable, are higher with respect to those of the previous fits of the class I FF parameters. This is due to the fact that here we are dealing with wider ranges of geometrical variables and potential energy, where harmonic approximations are no longer valid.  $S_1$  PES develops in a more restrained range of potential energies than  $S_0$  one does, and it is reflected in a smaller value of the fit root mean square error and a greater root-mean-square relative error.

To prove the importance of the class II FF cross-terms for the PES fit, cited in paragraph 3.2.6, we show in Figure 3.17 and Figure 3.18 the PES fitted without the functions  $U_{\text{bb}}^{\text{II}}(\vartheta_{\text{CNN}}, \vartheta_{\text{NNC}})$ ,  $U_{\text{tb}}^{\text{II}}(\varphi_{\text{CNNC}}, \vartheta_{\text{CNN}})$  and  $U_{\text{tb}}^{\text{II}}(\varphi_{\text{CNNC}}, \vartheta_{\text{NNC}})$ . We can observe the smaller resemblance of the fitted PES to the QM ones, confirmed by the fit RMSAE and RMSRE, which almost double.

- Fit RMSAE and RMSRE for  $S_0$  PES (no potential energy cross-terms):
  - RMSAE = 5.45 kcal mol<sup>-1</sup>
  - RMSRE = 13.1 %
- Fit RMSAE and RMSRE for  $S_1$  PES (no potential energy cross-terms):
  - RMSAE = 1.67 kcal mol<sup>-1</sup>
  - RMSRE = 21.1 %

In conclusion, the function  $\Delta U_{\text{ttb}}(\varphi_{\text{CNNC}}, \vartheta_{\text{CNN}}, \vartheta_{\text{NNC}})$  does not reproduce all the PES fine details, but this is the price to pay to have a good molecular description in a wide range of geometries with relatively simple analytic functions. Moreover, since the overall trend is well preserved, and

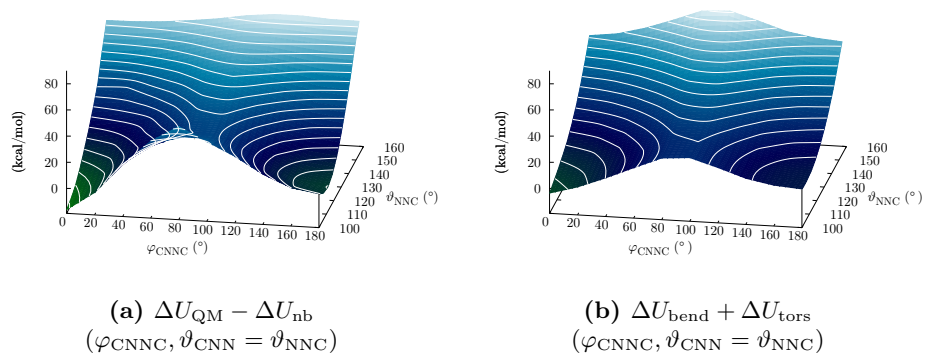


**Figure 3.17:** Fit results without cross-terms. Sections of reconstructed  $S_0$  PES.  $\Delta U_{\text{QM}} - \Delta U_{\text{nb}}$  (left) and  $\Delta U_{\text{bend}} + \Delta U_{\text{tors}}$  (right) as a function of  $\varphi_{\text{CNNC}}$  and  $\vartheta_{\text{NNC}}$  with symmetric bending angles ( $\vartheta_{\text{CNN}} = \vartheta_{\text{NNC}}$ ).

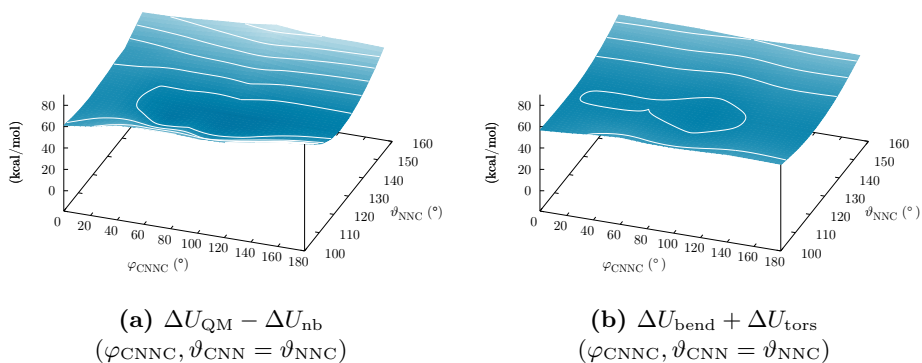


**Figure 3.18:** Fit results without cross-terms. Sections of reconstructed  $S_1$  PES.  $\Delta U_{\text{QM}} - \Delta U_{\text{nb}}$  (left) and  $\Delta U_{\text{bend}} + \Delta U_{\text{tors}}$  (right) as a function of  $\varphi_{\text{CNNC}}$  and  $\vartheta_{\text{NNC}}$  with symmetric bending angles ( $\vartheta_{\text{CNN}} = \vartheta_{\text{NNC}}$ ).

considering the thermal noise present at temperatures nearby 300 K, these errors could become negligible in a standard MD simulation.



## Chapter 4

# Molecular Dynamics Simulations of azobenzene photoexcitation

### 4.1 Energy minimization

For further validating the accuracy of the derived force field in reproducing QM results, we performed energy MM minimizations for  $S_0$  *trans* and *cis* isomers and  $S_1$  minimum energy conformations, and compared the resulting molecular geometries with those obtained via QM calculations. The results are shown in Tables from 4.1 to 4.4.

In the case of  $S_0$  *trans* and  $S_1$  planar isomers, which are the structures used for the FF parameterization, the variables values of QM and MM minima are very similar to one another (see Table 4.1 and Table 4.3). Indeed, the relative error (RE) for each bond length and angle stays under 1% and the absolute error (AE) reaches a maximum value of about 1°, with the exception of  $\vartheta_{\text{CNN}} = \vartheta_{\text{NNC}}$ , which differs from the QM value of about 4°. The

**Table 4.1:** Comparison between the most significant variables of QM and MM  $S_0$  *trans* isomers.

Variable	QM	MM	AE	RE (%)
$r_{\text{NN}}$ (Å)	1.2812	1.2808	-0.0005	-0.04
$r_{\text{CN}}$ (Å)	1.4240	1.4262	0.0022	0.15
$\vartheta_{\text{CNN}}$ (°)	113.29	108.92	-4.37	-3.86
$\vartheta_{\text{CCN}}$ (°)	114.76	114.03	-0.73	-0.63
$\vartheta_{\text{NCC}}$ (°)	124.68	125.72	1.04	0.84
$\varphi_{\text{CNNC}}$ (°)	180.00	180.00	0.00	0.00
$\varphi_{\text{CCNN}}$ (°)	180.00	180.00	0.00	0.00
$\varphi_{\text{NNCC}}$ (°)	0.00	0.00	0.00	0.00

**Table 4.2:** Comparison between the most significant variables of QM and MM  $S_0$  *cis* isomers.

Variable	QM	MM	AE	RE (%)
$r_{\text{NN}}$ (Å)	1.2783	1.2915	0.0132	1.03
$r_{\text{CN}}$ (Å)	1.4417	1.4244	-0.0173	-1.20
$\vartheta_{\text{CNN}}$ (°)	119.23	118.02	-1.21	-1.02
$\vartheta_{\text{CCN}}$ (°)	117.18	117.10	-0.09	-0.07
$\vartheta_{\text{NCC}}$ (°)	121.76	121.76	0.004	0.004
$\varphi_{\text{CNNC}}$ (°)	5.66	5.67	0.01	0.25
$\varphi_{\text{CCNN}}$ (°)	128.64	118.89	-9.75	-7.58
$\varphi_{\text{NNCC}}$ (°)	55.85	66.45	10.60	18.98

**Table 4.3:** Comparison between the most significant variables of QM and MM  $S_1$  planar isomers.

Variable	QM	MM	AE	RE (%)
$r_{\text{NN}}$ (Å)	1.2636	1.2634	-0.0002	-0.02
$r_{\text{CN}}$ (Å)	1.3647	1.3649	0.0003	0.02
$\vartheta_{\text{CNN}}$ (°)	128.02	128.26	0.25	0.19
$\vartheta_{\text{CCN}}$ (°)	118.20	117.77	-0.43	-0.36
$\vartheta_{\text{NCC}}$ (°)	121.65	120.63	-1.02	-0.84
$\varphi_{\text{CNNC}}$ (°)	180.00	180.00	0.00	0.00
$\varphi_{\text{CCNN}}$ (°)	180.00	180.00	0.00	0.00
$\varphi_{\text{NNCC}}$ (°)	0.00	0.00	0.00	0.00

reason can be identified in the function  $U_{\text{tbb}}(\varphi_{\text{CNNC}}, \vartheta_{\text{CNN}}, \vartheta_{\text{NCC}})$  used to approximate the PES: as discussed in paragraph ??, the function does not reproduce accurately the neighborhood of the  $S_0$  absolute minimum (*trans* isomer), and, consequently, the minimum energy point shifts to smaller values of  $\vartheta_{\text{CNN}}$  and  $\vartheta_{\text{NCC}}$ .

Concerning the  $S_0$  *cis* isomer (Table 4.2), the errors are a little higher but still acceptable, except for the MM values of  $\varphi_{\text{CCNN}}$  dihedral angles, which differ significantly from the QM ones ( $\sim 10^\circ$ ). This is probably because of the semi-relaxed scan used to determine  $\varphi_{\text{CCNN}}$  parameters (see paragraph 3.2.5), which makes them precise only if the molecular conformation remains in proximity to the *trans* minimum (which is not the case of the *cis* isomer). It is also important to recall that atomic charges were fitted on the *trans* isomer charge distribution and were not changed for the *cis* isomer.

In the case of the  $S_1$  twisted isomer (see Table 4.4), we see that the difference between the MM and QM optimized geometries is greater with respect to the previous cases: this is due to the fact that, again, the function  $U_{\text{tbb}}(\varphi_{\text{CNNC}}, \vartheta_{\text{CNN}}, \vartheta_{\text{NCC}})$  does not reproduce the double well of the PES at  $\varphi_{\text{CNNC}} \approx 90^\circ$ - $100^\circ$  and asymmetric bending angles  $\vartheta_{\text{CNN}}$  and  $\vartheta_{\text{NCC}}$ , but

**Table 4.4:** Comparison between the most significant variables of QM and MM  $S_1$  twisted isomers.

Variable	QM	MM	AE	RE (%)
$r_{\text{NN}}$ (Å)	1.2681	1.2632	-0.0048	-0.38
$r_{\text{CN}}$ (Å)	1.4180	1.3654	-0.0526	-3.71
$r_{\text{NC}}$ (Å)	1.3544	1.3654	0.0110	0.81
$\vartheta_{\text{CNN}}$ (°)	116.05	126.45	10.40	8.96
$\vartheta_{\text{NNC}}$ (°)	138.77	126.45	-12.32	-8.88
$\vartheta_{\text{CCN}1}$ (°)	116.21	117.48	1.28	1.10
$\vartheta_{\text{NCC}1}$ (°)	120.09	117.48	-2.61	-2.17
$\vartheta_{\text{CCN}2}$ (°)	123.08	120.93	-2.15	-1.74
$\vartheta_{\text{NCC}2}$ (°)	119.85	120.93	1.08	0.90
$\varphi_{\text{CNNC}}$ (°)	97.00	100.59	3.59	3.70
$\varphi_{\text{CCNN}1}$ (°)	176.84	179.79	2.96	1.67
$\varphi_{\text{NNCC}1}$ (°)	175.54	179.79	4.25	2.42
$\varphi_{\text{CCNN}2}$ (°)	-4.67	-0.85	3.83	81.86
$\varphi_{\text{NNCC}2}$ (°)	-6.88	-0.85	6.04	87.68

“smooths” them producing a unique well in the midpoint between the two (see  $\varphi_{\text{CNNC}} = 90^\circ$  PES section in Figure 3.15). Indeed, the MM molecule keeps the  $C_2$  axis and the bond lengths and the angles are a sort of intermediate values of QM molecular conformation ones. As we already said, this is not dramatic, since the PES flatness allow the molecule trajectory to explore the whole region. Another source of errors for the  $S_1$  FF is the fact that the rigid scan of  $\varphi_{\text{CNNC}}$ ,  $\vartheta_{\text{CNN}}$  and  $\vartheta_{\text{NNC}}$ , were made starting from *trans* and *cis* isomers geometries, which are  $S_0$ -optimized structures, relatively far from  $S_1$ -optimized ones.

After the geometrical comparison of this four stationary points, we compared the potential energy difference between molecular conformations in the same electronic state.

- $U_{0\text{QM}}(\mathbf{r}_{\text{cis min}}) - U_{0\text{QM}}(\mathbf{r}_{\text{trans min}}) = 8.52 \text{ kcal mol}^{-1}$
- $U_{0\text{MM}}(\mathbf{r}_{\text{cis eq}}) - U_{0\text{MM}}(\mathbf{r}_{\text{trans eq}}) = 9.19 \text{ kcal mol}^{-1}$
- $U_{1\text{QM}}(\mathbf{r}_{\text{pl min}}) - U_{1\text{QM}}(\mathbf{r}_{\text{tw min}}) = 0.25 \text{ kcal mol}^{-1}$
- $U_{1\text{MM}}(\mathbf{r}_{\text{pl eq}}) - U_{1\text{MM}}(\mathbf{r}_{\text{tw eq}}) = 2.44 \text{ kcal mol}^{-1}$

where we called  $\mathbf{r}_{\text{trans eq}}$  and  $\mathbf{r}_{\text{cis eq}}$  the molecular geometries of the MM optimized *trans* and *cis* isomers, respectively. As we can observe, the PE difference between the QM and MM structures is reasonably comparable. The error is higher for  $S_1$  state, always because of the wrong shape of  $\Delta U_{\text{tbb}}(\varphi_{\text{CNNC}}, \vartheta_{\text{CNN}}, \vartheta_{\text{NNC}})$  in the neighborhood of  $\varphi_{\text{CNNC}} = 90^\circ$ , which makes the  $S_1$  twisted minimum slightly shift to a lower potential energy with respect to the planar minimum.

## 4.2 Adaptive Biasing Force profiles

After verifying the correct description of the main geometrical parameters, the actual shape of the energy profiles was explored by means of force-biased MD simulations.

The Adaptive Biasing Force (ABF method) [57] is based on the thermodynamic integration (TI) scheme for computing free energy profiles. The Helmholtz free energy as a function of a set of collective variables  $\boldsymbol{\xi} = \{\xi_i\}$  is defined from the canonical distribution of  $\boldsymbol{\xi}$ ,  $\mathcal{P}(\boldsymbol{\xi})$ :

$$A(\boldsymbol{\xi}) = -\frac{1}{\beta} \ln \mathcal{P}(\boldsymbol{\xi}) + A_0. \quad (4.1)$$

In the TI formalism, the free energy is obtained from its gradient, which is generally calculated in the form of the average of a force  $\mathbf{F}_\xi$  exerted on  $\xi$ , taken over an iso- $\xi$  surface:

$$\nabla_\xi A(\boldsymbol{\xi}) = -\langle \mathbf{F}_\xi \rangle_\xi. \quad (4.2)$$

NAMD implementation of ABF relies partly on the classic formulation [58], and partly on a more versatile scheme originating in a work by Ruiz-Montero et al. [59], generalized by den Otter [60] and extended to multiple variables by Ciccotti et al. [61]. Consider a system subject to constraints of the form  $\sigma_k(\mathbf{x}) = 0$ . Let  $\{\mathbf{v}_i\}$  be arbitrarily chosen vector fields ( $\mathbb{R}^{3N} \rightarrow \mathbb{R}^{3N}$ ) verifying, for all  $i, j$  and  $k$ ,

$$\mathbf{v}_i \cdot \nabla_{\mathbf{x}} \xi_j = \delta_{ij} \quad (4.3)$$

$$\mathbf{v}_i \cdot \nabla_{\mathbf{x}} \sigma_k = 0, \quad (4.4)$$

then the following holds

$$\frac{\partial A}{\partial \xi_i} = \langle \mathbf{v}_i \cdot \nabla_{\mathbf{x}} V - k_B T \nabla_{\mathbf{x}} \cdot \mathbf{v}_i \rangle_\xi \quad (4.5)$$

where  $V$  is the potential energy function. The vector  $\mathbf{v}_i$  can be interpreted as the direction along which the force acting on variable  $\xi_i$  is measured, whereas the second term in the average corresponds to the geometric entropy contribution that appears as a Jacobian correction in the classic formalism [58]. Condition (4.3) states that the direction along which the system force on  $\xi_i$  is measured is orthogonal to the gradient of  $\xi_j$ , which means that the force measured on  $\xi_i$  does not act on  $\xi_j$ . Equation (4.4) implies that constraint forces are orthogonal to the directions along which the free energy gradient is measured, so that the measurement is effectively performed on unconstrained degrees of freedom.

In the framework of ABF,  $\mathbf{F}_\xi$  is accumulated in bins of finite size  $\Delta\xi$ , thereby providing an estimate of the free energy gradient according to equation (4.2). The biasing force applied on the collective variables to overcome free energy barriers is calculated as:

$$\mathbf{F}_{\xi \text{ ABF}} = \alpha(N_\xi) \nabla_{\mathbf{x}} \tilde{A}(\boldsymbol{\xi}) \quad (4.6)$$

where  $\nabla_{\mathbf{x}} \tilde{A}(\boldsymbol{\xi})$  denotes the current estimate of the free energy gradient at the current point  $\boldsymbol{\xi}$  in the collective variable subspace, and  $\alpha(N_\xi)$  is a scaling factor that is ramped from 0 to 1 as the local number of samples  $N_\xi$  increases, to prevent non equilibrium effects in the early phase of the simulation, when the gradient estimate has a large variance.

As sampling of the phase space proceeds, the estimate  $\nabla_{\mathbf{x}} \tilde{A}(\boldsymbol{\xi})$  is progressively refined. The biasing force introduced in the equations of motion guarantees that in the bin centered around  $\boldsymbol{\xi}$ , the forces acting along the selected collective variables average to zero over time. Eventually, as the underlying free energy surface is canceled by the adaptive bias, evolution of the system along  $\boldsymbol{\xi}$  is governed mainly by diffusion.

Thus, an ABF profile can be compared to a relaxed energy scan. In Figure 4.1 and Figure 4.2 we show ABF Helmholtz free energy ( $A_{\text{ABF}}$ ) as a function of  $\varphi_{\text{CNNC}}$  compared to the potential energies obtained with the merged rigid scan used for the FF parameterization (paragraph 3.2.6). The ABF profiles were computed for a molecule of  $S_0$  and  $S_1$  azobenzene in Argon at 300 K and 1 atm. Argon atoms have been used in order to have some heat exchange, improving the performance of the thermostat.

As we can observe, ABF profile for azobenzene in the ground state is comparable with the  $\Delta U_{\text{QM}}$  one, but in the case of  $S_1$  state, although the shape of the two profiles is not too dissimilar, the potential energy derived from the merged rigid scan is higher, making difficult the comparison. This is because the scan was made using  $S_0$  *trans* and *cis* geometries, which are  $S_0$  optimized geometries. As a consequence, we get a correct PE profile in the case of the ground state, but the relative  $S_1$  potential energies are shifted to higher values with respect to those of a scan made using  $S_1$  optimized geometries. For this reason, we performed QM constrained optimization in the  $S_1$  state at  $\varphi_{\text{CNNC}} = 0^\circ$  in order to compare the peaks height of the ABF profiles with the ones obtained with QM calculations. We also plotted the PE of the energies of the three minimum geometries  $\mathbf{r}_{\text{pl min}}$ ,  $\mathbf{r}_{\text{tw min}}$  and  $\mathbf{r}_{\text{CI}}$ .

- $\varphi_{\text{CNNC}} = 0^\circ$ ;  
 $\Delta U_{\text{QM}}(\mathbf{r}) = U_{\text{QM}}(\mathbf{r}_{\varphi_{\text{CNNC}}=0}) - U_{\text{QM}}(\mathbf{r}_{\text{tw min}}) = 10.46 \text{ kcal mol}^{-1}$

As regards the  $S_0$  ABF profile, we can observe that the QM calculations slightly differ from values obtained with ABF simulations in the barriers height. This could be partly due to the fact that the peaks are the most delicate parts of the profiles: in fact, they are the last regions which are

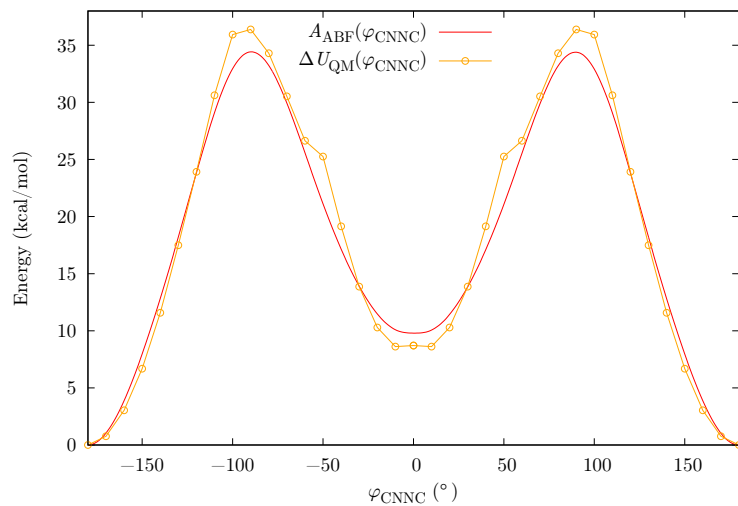


**Figure 4.1:** ABF Helmholtz free energy ( $A_{\text{ABF}}$ ) obtained with the new FF of  $S_0$  of an azobenzene molecule in Argon at 300 K and 1 atm, and QM potential energy ( $\Delta U_{\text{QM}}$ ) obtained with the merged rigid scan of  $\varphi_{\text{CNNC}}$ ,  $\vartheta_{\text{CNN}}$  and  $\vartheta_{\text{NNC}}$  as a function of  $\varphi_{\text{CNNC}}$ .

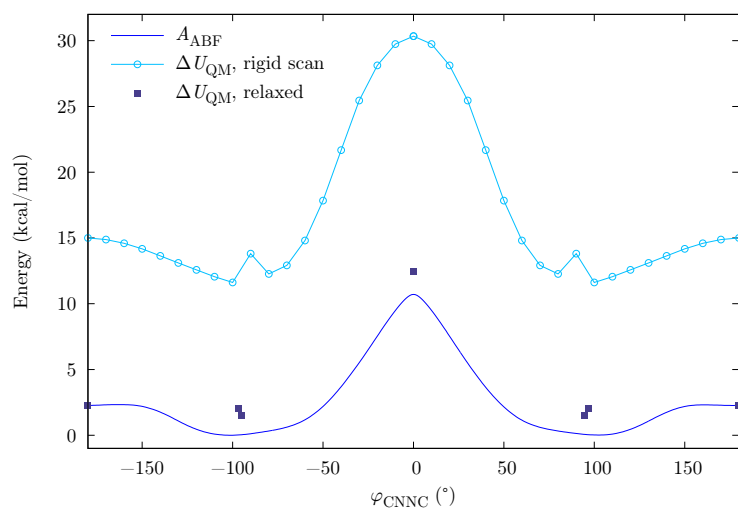


**Figure 4.2:**  $A_{\text{ABF}}$  obtained with the new FF of  $S_1$  of an azobenzene molecule in Argon at 300 K and 1 atm, QM potential energy ( $\Delta U_{\text{QM}}$ ) obtained with the merged rigid scan of  $\varphi_{\text{CNNC}}$ ,  $\vartheta_{\text{CNN}}$  and  $\vartheta_{\text{NNC}}$ , and potential energies of four geometries optimized in the  $S_1$  state as a function of  $\varphi_{\text{CNNC}}$ .

properly sampled by the ABF algorithm and a longer calculation may have led to obtain more accurate barriers.

The  $S_1$  ABF profile confirms what emerged from the comparison we made between the PE of the minimum geometries in the previous paragraph. Indeed, we note that the  $S_1$  planar minimum ( $\varphi_{\text{CNNC}} = 180^\circ$ ) is found at about  $2 \text{ kcal mol}^{-1}$  above the  $S_1$  twisted one ( $\varphi_{\text{CNNC}} \approx 90 - 100^\circ$ ).

On the other hand, the barrier height at  $\varphi_{\text{CNNC}} = 0^\circ$  measured with respect to the twisted minimum is comparable with the one obtained via QM calculations.

Furthermore, we must remember that we are comparing a potential energy with a Helmholtz free energy, which could be slightly different. However, the profiles are also reasonably comparable with those present in literature [24, 62].

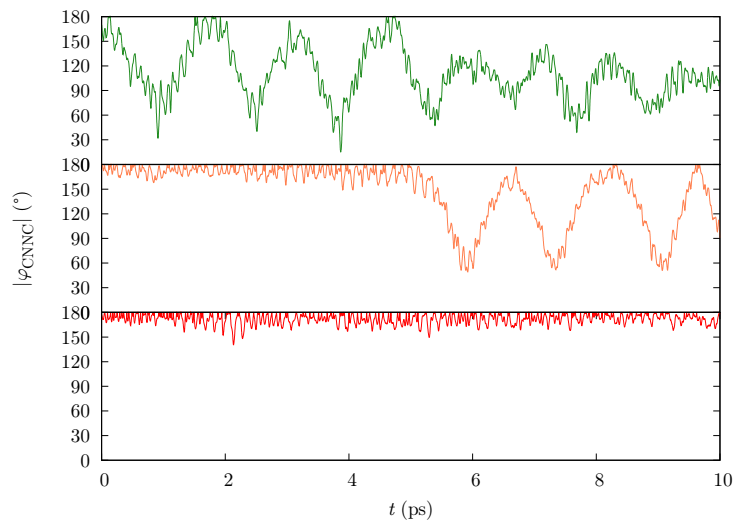
## 4.3 Trajectories analysis

### 4.3.1 Azobenzene in vacuum

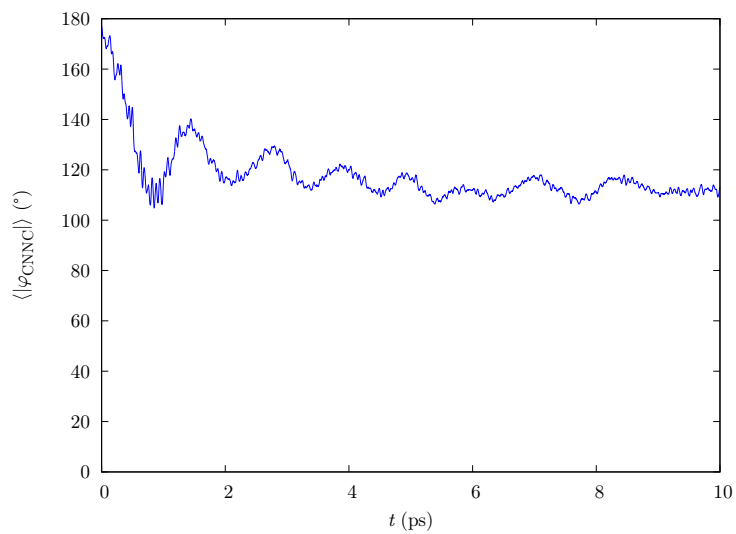
Once performed the above cited tests of the force field, we ran a Molecular Dynamics simulation of a single molecule of azobenzene in the ground state in vacuum at constant temperature (300 K) and volume (NVT). Then, we simulated the excitation process employing as starting configurations 100 frames of the  $S_0$  trajectory by changing the force field from the one of  $S_0$  to the one of  $S_1$ . We let the molecule evolve following the  $S_1$  PES for 10 ps and analyzed the trajectories of  $\varphi_{\text{CNNC}}$ ,  $\vartheta_{\text{CNN}}$  and  $\vartheta_{\text{NNC}}$  (Figure 4.3).

In Figure 4.3 we show  $\varphi_{\text{CNNC}}$  as a function of time for three different trajectories and averaged over all the simulations. In the first one the molecule soon reaches the  $S_1$  twisted geometry; in the second one, the C–N–N–C dihedral oscillates around  $180^\circ$  before going towards  $90^\circ$ ; in the last one, the molecule remains almost planar during all the simulation time. We noted that, in general, the molecule tends to rapidly reach the twisted minimum region. Indeed, defining  $\tau_{90}$  as the average time to reach the twisted geometry, we obtain  $\tau_{90} = 1.2 \text{ ps}$ . In about the 2% of the cases, after 10 ps the C–N–N–C dihedral angle is still oscillating around  $180^\circ$ . This gives a further proof of the presence of a torsional barrier to break the planarity.

In Figure 4.4a we show the trajectory projected on the two bending angles coordinates superimposed to the QM potential energy map of  $S_1$ . We observe, that the majority of the points of the trajectory are found in a region between the double well of the  $S_1$  PES. This is due to the fact that, as we argued in paragraph 3.2.6 and in the previous paragraphs of this chapter, the function  $\Delta U_{\text{tbb}}$  “smooths” them producing a unique well in the midpoint between the two (Figure 3.15d). As a consequence, the molecule rarely reaches regions where  $S_1$  and  $S_0$  are degenerate (see Figure 4.4b). Since the decay probability decreases with the increase of energy gap, this means

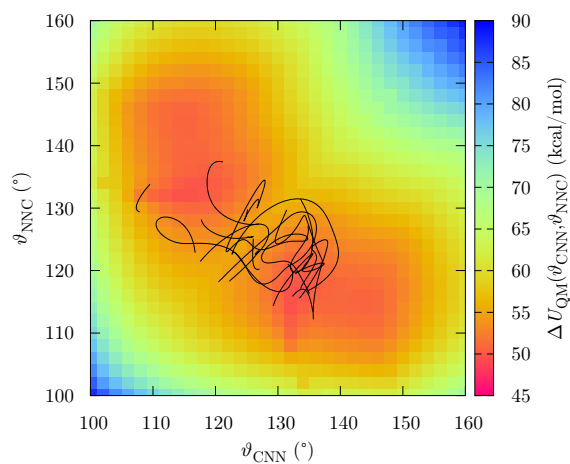


(a)

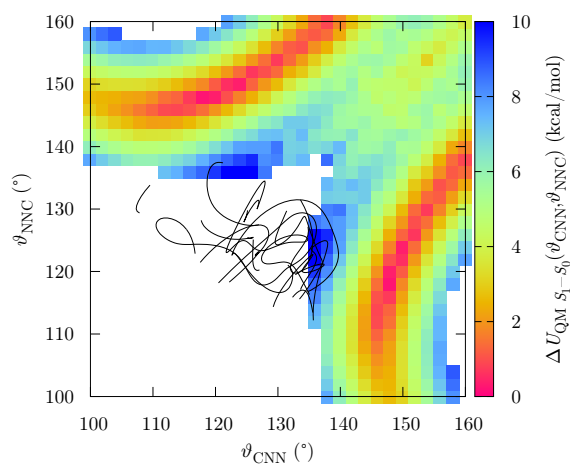


(b)

**Figure 4.3:** Top: MD trajectories of  $|\varphi_{\text{CNNC}}(t)|$  of three NTV simulations of one azobenzene molecule in the  $S_1$  electronic state in vacuum. Bottom: average trajectory over 100 simulations  $\langle |\varphi_{\text{CNNC}}(t)| \rangle$ . At  $t = 0$  the molecule is found in different Frank-Condon points.



(a)



(b)

**Figure 4.4:** Top: MD trajectories in vacuum of the two C–N–N bending angles  $\vartheta_{\text{CNN}}$ ,  $\vartheta_{\text{NNC}}$  of three NVT simulations of one azobenzene molecule in the  $S_1$  electronic state, superimposed to the QM energy map of the  $S_1$  state at  $\varphi_{\text{CNC}} = 90^\circ$  ( $\Delta U_{\text{QM}}(\varphi = 90^\circ, \vartheta_{\text{CNN}}, \vartheta_{\text{NNC}})$ ). Bottom: MD trajectories in vacuum of the two C–N–N bending angles  $\vartheta_{\text{CNN}}$ ,  $\vartheta_{\text{NNC}}$  of three NVT simulations of one azobenzene molecule in the  $S_1$  electronic state, superimposed to the QM  $S_1$ - $S_0$  energy gap map at  $\varphi_{\text{CNC}} = 90^\circ$  ( $\Delta U_{\text{QM}}(\varphi_{\text{CNC}} = 90^\circ, \vartheta_{\text{CNN}}, \vartheta_{\text{NNC}})$ ).

that the hopping events will be rather rare. Thus, the decay probability expression employed by Tiberio and co-workers is not the best one to be used in this case.

We then decided to re-normalize the decay probability so as to give any trajectory a chance to hop from  $S_1$  to  $S_0$  whenever it reaches a region with an energy gap smaller than 0.3 eV (7 kcal mol<sup>-1</sup>). This hopping probability is proportional to  $\exp[-\Delta U_{QM S_1-S_0}(\varphi_{\text{CNNC}}, \vartheta_{\text{CNN}}, \vartheta_{\text{NNC}})]$ .

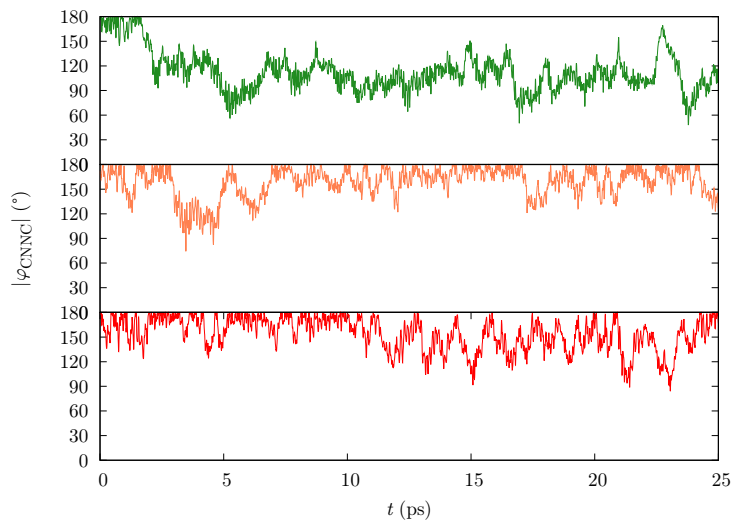
However, this makes the lifetime of the excited state ( $\tau_{S_1}$ ) physically meaningless. Indeed, we found  $\tau_{S_1} \approx 6$  ps, which is much greater than the literature values, usually below 1 ps [20, 5]).

The obtained photoisomerization quantum yield ( $\Phi_v$ ) is 0.35, comparable with the literature results (0.35 [63]; 0.46 [5]; 0.33 [20]).

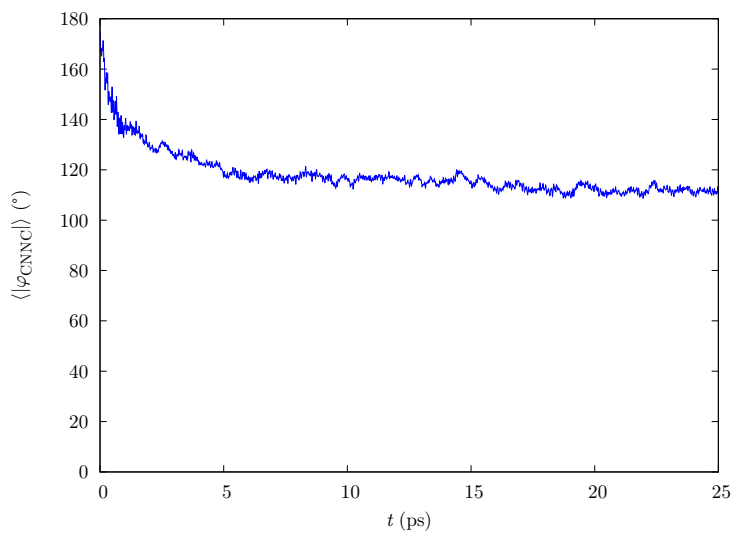
### 4.3.2 Azobenzene in 8CB

We then performed NVT MD simulations at 300 K and ca. 1 atm of a sample of 134 molecules of azobenzene dissolved in 2866 molecules of 8CB. We let the sample equilibrate for several nanoseconds, then, for each azobenzene molecule, we started a simulation of 25 ps in which it was brought to the excited states.

In Figure 4.5 we show  $\varphi_{\text{CNNC}}$  as a function of time for three different trajectories and averaged over all the simulations. We observe in figure Figure 4.5 that the molecules take longer to reach the  $S_1$  twisted geometry with respect to the simulations in vacuum. Indeed, we found that  $\tau_{90} = 4.0$  ps, due to the steric hindrance of the solvent, that prevents torsion. Furthermore, in Figure 4.6, we note that the trajectory explores wider values of C–N–N bending angles. This is again an effect of the solvent, which tends to elongate the molecule. Consequently, the trajectory reaches regions in where the energy gap between the electronic states is smaller. This, combines with the electrostatic effect of the solvent, which stabilizes  $S_1$  and destabilizes  $S_0$ , thus, further reducing the  $S_1$ - $S_0$  energy gap. As a result, the molecule can hop at higher values of  $\varphi_{\text{CNNC}}$ , lowering the photoisomerization quantum yield, which is  $\Phi_{8\text{CB}} = 0.2$ . This value is comparable with the experimental ones in several organic solvents (in hexane: 0.20-0.27 [5]; 0.25 [63]).

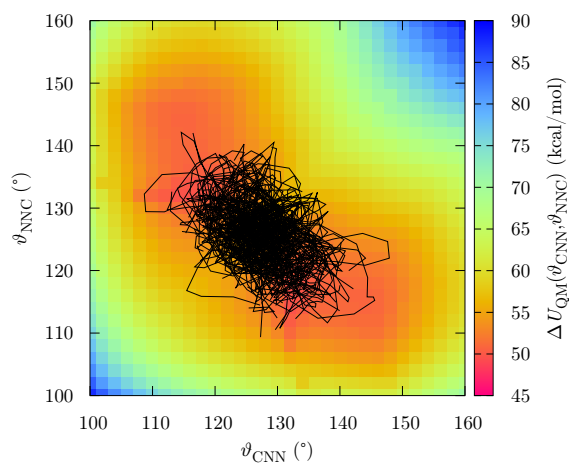


(a)

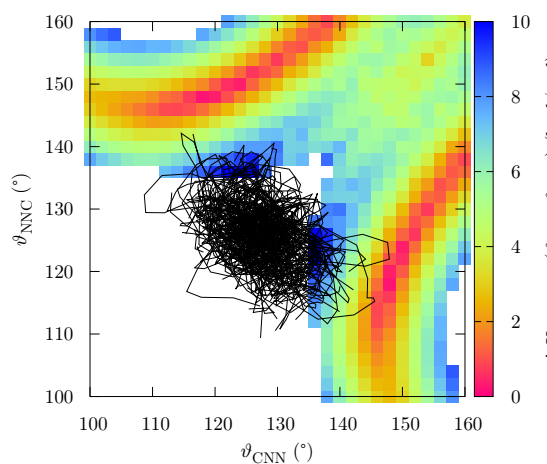


(b)

**Figure 4.5:** Top: MD trajectories  $|\varphi_{\text{CNNC}}(t)|$  of three NVT simulations of one azobenzene molecule in the  $S_1$  electronic state in 8CB. Bottom: average trajectory over 134 simulations  $\langle |\varphi_{\text{CNNC}}(t)| \rangle$ . At  $t = 0$  the molecule is found in different Frank-Condon points.



(a)



(b)

**Figure 4.6:** Top: MD trajectories in 8CB of the two C–N–N bending angles  $\vartheta_{\text{CNN}}$ ,  $\vartheta_{\text{CNN}}$  of three NVT simulations of the azobenzene molecule in the  $S_1$  electronic state, superimposed to the QM energy map of the  $S_1$  state at  $\varphi_{\text{CNNC}} = 90^\circ$  ( $\Delta U_{\text{QM}}(\varphi = 90^\circ, \vartheta_{\text{CNN}}, \vartheta_{\text{NNC}})$ ). Bottom: MD trajectories in 8CB of the two C–N–N bending angles  $\vartheta_{\text{CNN}}$ ,  $\vartheta_{\text{CNN}}$  of three NVT simulations of the azobenzene molecule in the  $S_1$  electronic state, superimposed to the QM  $S_1$ - $S_0$  energy gap map at  $\varphi_{\text{CNNC}} = 90^\circ$  ( $\Delta U_{\text{QM}}(\varphi_{\text{CNNC}} = 90^\circ, \vartheta_{\text{CNN}}, \vartheta_{\text{NNC}})$ ).

## Chapter 5

# Conclusions and future outlooks

In this work we have studied, by means of Molecular Dynamics simulations, the *trans-cis* photoisomerization mechanism of azobenzene dissolved in a liquid crystal when excited in the state associated to the  $n\pi^*$  transition (first excited singlet  $S_1$ ).

In order to properly describe the system, we have calculated a new Quantum-Mechanics-derived class II force field (FF) for azobenzene, including some terms of coupling between the internal molecular modes most involved in the photochemical process (*i.e.*, the C–N–N–C torsion and the two C–N–N bendings), which allowed us to accurately describe the two electronic states involved in the process (the ground state  $S_0$  and the  $S_1$  state). The FF parameters were determined by fitting the quantum mechanics potential energy profiles. In order to take into account the new FF terms, we modified the Molecular Dynamics software NAMD introducing new functions for cross-term energy and forces, and new keywords in the parameter input file. We ran simulations on the excited state and evaluated the probability of the decay process after a certain time has elapsed from the Frank-Condon excitation (ps), as a function of the instantaneous QM potential energy gap between the two electronic states.

We first performed simulations of one azobenzene molecule in vacuum and then of samples of azobenzene molecules dissolved in the liquid crystal 4'-octyl-4-biphenylcarbonitrile (8CB) at 300 K.

We obtained meaningful results in terms of the photoisomerization mechanism and quantum yield, both in vacuum and in 8CB ( $\Phi_v = 0.35$ ,  $\Phi_{8CB} = 0.20$ ), which were found to be comparable to the literature ones ( $\Phi_v = 0.33$ ,  $\Phi_{8CB} = 0.25$  [63]). We wish to point out that from the analysis of the trajectories we noted that the errors made in the approximation of the potential energy surface (PES) prevent the molecule from completely exploring the QM  $S_1$  minimum energy regions, (from where the decay process should

occur). This is because the analytic functions used in the new FF, even though of fundamental importance for the fit of the PES, do not perfectly reproduce the QM potential energy surface. These inaccuracies, however, can only affect the  $S_1$  lifetimes (make them longer than the experimental ones).

The simulations showed that the *trans-cis* photoisomerization mechanism follows an inversion-assisted torsional pathway both in vacuum and in 8CB, but in the latter case, the inversion character is emphasized with respect to what happens in vacuum (higher values of C–N–N bending angles). The solvent hindrance, combined with its electrostatic effect (which stabilizes the  $S_1$  state and destabilizes the  $S_0$  one), reduce the energy gap between the states and make the molecule reach high-decay-probability regions at wider values of the C–N–N–C dihedral angle, making the quantum yield of photoisomerization decrease.

As for the outlooks, we plan to improve several aspects of the presented approach and to add various features. The first step will be to improve the fit of the potential energy surface by adding other FF cross-terms or by interpolating using splines. Then, we will implement the Tully algorithm [64] to evaluate the decay process on the fly. This is a fewest-switches surface-hopping algorithm, based on the inter-state non-adiabatic coupling vector (which we already calculated). Another feature that we want to implement is to take into account the azobenzene transition dipole moment and simulate a continuous polarized-light-induced excitation, in order to examine the change in molecular organization and director orientation upon irradiation [65].

# Bibliography

- [1] P. Mondal, G. Granucci, D. Rastädter, M. Persico, and I. Burghardt. Azobenzene as a photoregulator covalently attached to rna: a quantum mechanics/molecular mechanics-surface hopping dynamics study. *Chem. Sci.*, 9:4671–4681, 2018.
- [2] T. Ikeda. Photomodulation of liquid crystal orientations for photonic applications. *J. Mater. Chem.*, 13:2037–2057, 2003.
- [3] K. Goda, M. Omori, and K. Takatoh. Optical switching in guest-host liquid crystal devices driven by photo- and thermal isomerisation of azobenzene. *Liquid Crystals*, 45(4):485–490, 2017.
- [4] X. Zhu, F. Yin, H. Zhao, S. Chen, and Z. Bian. Some new azobenzene liquid crystals involving chalcone and ester linkages. *RSC Adv.*, 7:46344–46353, 2017.
- [5] G. Tiberio, L. Muccioli, R. Berardi, and C. Zannoni. How does the *trans-cis* photoisomerization of azobenzene take place in organic solvents? *ChemPhysChem*, 11(5):1018–1028, 2010.
- [6] H. Finkelmann, E. Nishikawa, G. G. Pereira, and M. Warner. A new opto-mechanical effect in solids. *Phys. Rev. Lett.*, 87:015501, Jun 2001.
- [7] V. P. Toshchevikov, M. Saphiannikova, and G. Heinrich. Theory of light-induced deformation of azobenzene elastomers: Influence of network structure. *The Journal of Chemical Physics*, 137(2):024903, 2012.
- [8] V. Cantatore, G. Granucci, G. Rousseau, G. Padula, and M. Persico. Photoisomerization of self-assembled monolayers of azobiphenyls: Simulations highlight the role of packing and defects. *The Journal of Physical Chemistry Letters*, 7(19):4027–4031, 2016.
- [9] X. Tong, G. Wang, A. Yavrian, T. Galstian, and Y. Zhao. Dual-mode switching of diffraction gratings based on azobenzene-polymer-stabilized liquid crystals. *Advanced Materials*, 17(3):370–374, 2005.

- [10] Y. Lansac, M. Glaser, N. Clark, and O. Lavrentovich. Photocontrolled nanophase segregation in a liquid-crystal solvent. *Nature*, 398:54–57, 1999.
- [11] J. M. Mativetsky, G. Pace, M. Elbing, M. A. Rampi, M. Mayor, and P. Samori. Azobenzenes as light-controlled molecular electronic switches in nanoscale metal-molecule-metal junctions. *Journal of the American Chemical Society*, 130(29):9192–9193, 2008.
- [12] F. Bernardi, M. Olivucci, and M. A. Robb. Potential energy surface crossings in organic photochemistry. *Chem. Soc. Rev.*, 25:321–328, 1996.
- [13] M. Garavelli. Computational organic photochemistry: Strategy, achievements and perspectives. *Theoretical Chemistry Accounts*, 116:87–105, 2006.
- [14] N. L. Doltsinis and D. Marx. Nonadiabatic car-parrinello molecular dynamics. *Phys. Rev. Lett.*, 88:166402, 2002.
- [15] X. Li, J. C. Tully, H. B. Schlegel, and M. J. Frisch. *Ab initio* ehrenfest dynamics. *The Journal of Chemical Physics*, 123(8):084106, 2005.
- [16] M. Barbatti, G. Granucci, M. Persico, M. Ruckebauer, M. Vazdar, M. Eckert-Maksić, and H. Lischka. The on-the-fly surface-hopping program system newton-x: Application to ab initio simulation of the nonadiabatic photodynamics of benchmark systems. *Journal of Photochemistry and Photobiology A: Chemistry*, 190(2):228 – 240, 2007.
- [17] J. Kongsted, A. Osted, K. Mikkelsen, P.-O. Åstrand, and O. Christiansen. Solvent effects on the  $n \rightarrow \pi^*$  electronic transition in formaldehyde: A combined coupled cluster/molecular dynamics study. *The Journal of chemical physics*, 121:8435–45, 2004.
- [18] M. J. Bearpark and M. Boggio-Pasqua. Excited states of conjugated hydrocarbon radicals using the molecular mechanics - valence bond (mmvb) method. *Theoretical Chemistry Accounts*, 110:105–114, 2003.
- [19] T. Frauenheim, G. Seifert, M. Elstner, Niehaus T., Kohler C., M. Amkreutz, M. Sternberg, Z. Hajnal, A. Di Carlo, and S. Suhai. Atomistic simulations of complex materials: ground-state and excited-state properties. *Journal of Physics: Condensed Matter*, 14(11):3015, 2002.
- [20] C. Ciminelli, G. Granucci, and M. Persico. The photoisomerization mechanism of azobenzene: A semiclassical simulation of nonadiabatic dynamics. *Chemistry - A European Journal*, 10(9):2327–2341, 2004.

- [21] C. Ciminelli, G. Granucci, and M. Persico. Are azobenzenophanes rotation-restricted? *The Journal of Chemical Physics*, 123(17):174317, 2005.
- [22] J. R. Maple, M.-J. Hwang, T. P. Stockfisch, U. Dinur, M. Waldman, C. S. Ewig, and A. T. Hagler. Derivation of class ii force fields. i. methodology and quantum force field for the alkyl functional group and alkane molecules. *Journal of Computational Chemistry*, 15(2):162–182, 1994.
- [23] F. Santoro, A. Lami, R. Improta, and V. Barone. Effective method to compute vibrationally resolved optical spectra of large molecules at finite temperature in the gas phase and in solution. *The Journal of Chemical Physics*, 126(18):184102, 2007.
- [24] A. Cembran, F. Bernardi, M. Garavelli, L. Gagliardi, and G. Orlandi. On the mechanism of the cis-trans isomerization in the lowest electronic states of azobenzene: S<sub>0</sub>, s<sub>1</sub> and t<sub>1</sub>. *Journal of the American Chemical Society*, 126(10):3234–3243, 2004.
- [25] I. Conti, M. Garavelli, and G. Orlandi. The different photoisomerization efficiency of azobenzene in the lowest  $n\pi^*$  and  $\pi\pi^*$  singlets: The role of a phantom state. *Journal of the American Chemical Society*, 130(15):5216–5230, 2008.
- [26] L. Gagliardi, G. Orlandi, F. Bernardi, A. Cembran, and M. Garavelli. A theoretical study of the lowest electronic states of azobenzene: the role of torsion coordinate in the cis–trans photoisomerization. *Theoretical Chemistry Accounts*, 111(2):363–372, 2004.
- [27] C.-W. Chang, Y.-C. Lu, T.-T. Wang, and E. W.-G. Diau. Photoisomerization dynamics of azobenzene in solution with  $s_1$  excitation: A femtosecond fluorescence anisotropy study. *Journal of the American Chemical Society*, 126(32):10109–10118, 2004.
- [28] V. Marturano, V. Ambrogi, N. Bandeira, B. Tylkowski, M. Giamberini, and P. Cerruti. Modeling of azobenzene-based compounds. *Physical Sciences Reviews*, 2(1):138–141, 2017.
- [29] H. Rau. Spectroscopic properties of organic azo compounds. *Angewandte Chemie International Edition in English*, 12(3):224–235, 1973.
- [30] R. M. Hochstrasser and S. K. Lower. Polarization of the spectra of crystalline azobenzene and mixed crystals of azobenzene in stilbene at 77 and 42K in the region of the lowest  $n\pi^*$  transition. *The Journal of Chemical Physics*, 36(12):3505–3506, 1962.

- [31] H. Rau and E. Lueddecke. On the rotation-inversion controversy on photoisomerization of azobenzenes. experimental proof of inversion. *Journal of the American Chemical Society*, 104(6):1616–1620, 1982.
- [32] P. Bortolus and S. Monti. *Cis-trans* photoisomerization of azobenzene. solvent and triplet donors effects. *The Journal of Physical Chemistry*, 83(6):648–652, 1979.
- [33] N. Siampiringue, G. Guyot, S. Monti, and P. Bortolus. The *cis-trans* photoisomerization of azobenzene: an experimental re-examination. *Journal of Photochemistry*, 37(1):185 – 188, 1987.
- [34] T. Fujino, S. Yu. Arzhantsev, and T. Tahara. Femtosecond time-resolved fluorescence study of photoisomerization of *trans*-azobenzene. *The Journal of Physical Chemistry A*, 105(35):8123–8129, 2001.
- [35] T. Ishikawa, T. Noro, and T. Shoda. Theoretical study on the photoisomerization of azobenzene. *The Journal of Chemical Physics*, 115(16):7503–7512, 2001.
- [36] T. Schultz, J. Quenneville, B. Levine, A. Toniolo, T. J. MartíÁñez, S. Lochbrunner, M. Schmitt, J. P. Shaffer, M. Z. Zgierski, and A. Stolow. Mechanism and dynamics of azobenzene photoisomerization. *Journal of the American Chemical Society*, 125(27):8098–8099, 2003.
- [37] A. Nenov, R. Borrego-Varillas, A. Oriana, L. Ganzer, F. Segatta, I. Conti, J. Segarra-Marti, J. Omachi, M. Dapor, S. Taioli, C. Manzoni, S. Mukamel, G. Cerullo, and M. Garavelli. Uv-light-induced vibrational coherences: The key to understand kasha rule violation in *trans*-azobenzene. *The Journal of Physical Chemistry Letters*, 9(7):1534–1541, 2018.
- [38] T. Ikeda and O. Tsutsumi. Optical switching and image storage by means of azobenzene liquid-crystal films. *Science*, 268(5219):1873–1875, 1995.
- [39] A.N. Shipway and I. Willner. Electronically transduced molecular mechanical and information functions on surfaces. *Accounts of Chemical Research*, 34(6):421–432, 2001.
- [40] R. Ballardini, V. Balzani, A. Credi, M. T. Gandolfi, and M. Venturi. Artificial molecular-level machines: Which energy to make them work? *Accounts of Chemical Research*, 34(6):445–455, 2001.
- [41] I. Vecchi, A. Arcioni, C. Bacchiocchi, G. Tiberio, P. Zanirato, and C. Zannoni. Expected and unexpected behavior of the orientational

- order and dynamics induced by azobenzene solutes in a nematic. *The Journal of Physical Chemistry B*, 111(13):3355–3362, 2007.
- [42] O. M. Roscioni, A. Micas, and C. Zannoni. On the effect of *trans* and *cis* azobenzene on their local liquid crystal environment. 2018.
- [43] P. A. Bash, U. C. Singh, F. K. Brown, R. Langridge, and P. A. Kollman. Calculation of the relative change in binding free energy of a protein-inhibitor complex. *Science*, 235(4788):574–576, 1987.
- [44] A. Warshel, S. Russell, and F. Sussman. Computer simulation of enzymatic reactions. *Israel Journal of Chemistry*, 27(2):217–224, 1986.
- [45] F. Avbelj, J. Moult, D. H. Kitson, M. N. G. James, and A. T. Hagler. Molecular dynamics study of the structure and dynamics of a protein molecule in a crystalline ionic environment, streptomyces griseus protease a. *Biochemistry*, 29(37):8658–8676, 1990.
- [46] J. R. Maple, U. Dinur, and A. T. Hagler. Derivation of force fields for molecular mechanics and dynamics from ab initio energy surfaces. *Proc. Natl. Acad. Sci.*, 85(15):5350–5354, 1988.
- [47] J. Wang, R. M. Wolf, J. W. Caldwell, P. A. Kollman, and D. A. Case. Development and testing of a general amber force field. *Journal of Computational Chemistry*, 25(9):1157–1174, 2004.
- [48] M. J. Frisch, G. W. Trucks, H. B. Schlegel, G. E. Scuseria, M. A. Robb, J. R. Cheeseman, G. Scalmani, V. Barone, G. A. Petersson, H. Nakatsuji, X. Li, M. Caricato, A. V. Marenich, J. Bloino, B. G. Janesko, R. Gomperts, B. Mennucci, H. P. Hratchian, J. V. Ortiz, A. F. Izmaylov, J. L. Sonnenberg, D. Williams-Young, F. Ding, F. Lipparini, F. Egidi, J. Goings, B. Peng, A. Petrone, T. Henderson, D. Ranasinghe, V. G. Zakrzewski, J. Gao, N. Rega, G. Zheng, W. Liang, M. Hada, M. Ehara, K. Toyota, R. Fukuda, J. Hasegawa, M. Ishida, T. Nakajima, Y. Honda, O. Kitao, H. Nakai, T. Vreven, K. Throssell, Jr. Montgomery, J. A., J. E. Peralta, F. Ogliaro, M. J. Bearpark, J. J. Heyd, E. N. Brothers, K. N. Kudin, V. N. Staroverov, T. A. Keith, R. Kobayashi, J. Normand, K. Raghavachari, A. P. Rendell, J. C. Burant, S. S. Iyengar, J. Tomasi, M. Cossi, J. M. Millam, M. Klene, C. Adamo, R. Cammi, J. W. Ochterski, R. L. Martin, K. Morokuma, O. Farkas, J. B. Foresman, and D. J. Fox. Gaussian-16 Revision B.01, 2016. Gaussian Inc. Wallingford CT.
- [49] F. Aquilante, J. Autschbach, R. K. Carlson, L. F. Chibotaru, M. G. Delcey, L. De Vico, I. Fdez. Galván, N. Ferré, L. M. Frutos, L. Gagliardi, M. Garavelli, A. Giussani, C. E. Hoyer, G. Li Manni, H. Lischka, D. Ma, P. Å. Malmqvist, T. Müller, A. Nenov, M. Olivucci, T. B. Pedersen,

- D. Peng, F. Plasser, B. Pritchard, M. Reiher, I. Rivalta, I. Schapiro, J. Segarra-Martí, M. Stenrup, D. G. Truhlar, L. Ungur, A. Valentini, S. Vancoillie, V. Veryazov, V. P. Vysotskiy, O. Weingart, F. Zapata, and R. Lindh. Molcas 8: New capabilities for multiconfigurational quantum chemical calculations across the periodic table. *Journal of Computational Chemistry*, 37(5):506–541, 2015.
- [50] F. Gao and Lixing Han. Implementing the nelder-mead simplex algorithm with adaptive parameters. *Computational Optimization and Applications*, 51(1):259–277, 2012.
- [51] S. Dasgupta and W. A. Goddard. Hessian-biased force fields from combining theory and experiment. *The Journal of Chemical Physics*, 90(12):7207–7215, 1989.
- [52] S. Shi, L. Yan, Y. Yang, Fisher-Shaulsky J., and T. Thacher. An extensible and systematic force field, esff, for molecular modeling of organic, inorganic, and organometallic systems. *Journal of Computational Chemistry*, 24(9):1059–1076, 2003.
- [53] T. A. Halgren. Maximally diagonal force constants in dependent angle-bending coordinates. ii. implications for the design of empirical force fields. *Journal of the American Chemical Society*, 112(12):4710–4723, 1990.
- [54] L. Nørskov-Lauritsen and N. L. Allinger. A molecular mechanics treatment of the anomeric effect. *Journal of Computational Chemistry*, 5(4):326–335, 1984.
- [55] A. Warshel and S. Lifson. An empirical function for second neighbor interactions and its effect on vibrational modes and other properties of cyclo- and *n*-alkanes. *Chemical Physics Letters*, 4(5):255 – 256, 1969.
- [56] S. Yuan, Y. Dou, W. Wu, Y. Hu, and J. Zhao. Why does trans-azobenzene have a smaller isomerization yield for  $\pi\pi^*$  excitation than for  $n\pi^*$  excitation? *The Journal of Physical Chemistry A*, 112(51):13326–13334, 2008.
- [57] E. Darve, D. Rodríguez-Gómez, and A. Pohorille. Adaptive biasing force method for scalar and vector free energy calculations. *The Journal of Chemical Physics*, 128(14):144120, 2008.
- [58] E. A. Carter, G. Ciccotti, J. T. Hynes, and R. Kapral. Constrained reaction coordinate dynamics for the simulation of rare events. *Chemical Physics Letters*, 156(5):472 – 477, 1989.

- [59] M. J. Ruiz-Montero, D. Frenkel, and J. J. Brey. Efficient schemes to compute diffusive barrier crossing rates. *Molecular Physics*, 90(6):925–942, 1997.
- [60] W. K. den Otter. Thermodynamic integration of the free energy along a reaction coordinate in cartesian coordinates. *The Journal of Chemical Physics*, 112(17):7283–7292, 2000.
- [61] G. Ciccotti, R. Kapral, and E. Vanden-Eijnden. Blue moon sampling, vectorial reaction coordinates, and unbiased constrained dynamics. *ChemPhysChem*, 6(9):1809–1814, 2005.
- [62] R. Turanský, M. Konôpka, N. L. Doltsinis, I. Štich, and D. Marx. Switching of functionalized azobenzene suspended between gold tips by mechanochemical, photochemical, and opto-mechanical means. *Phys. Chem. Chem. Phys.*, 12:13922–13932, 2010.
- [63] H. M. D. Bandara and S. C. Burdette. Photoisomerization in different classes of azobenzene. *Chem. Soc. Rev.*, 41:1809–1825, 2012.
- [64] J. C. Tully. Molecular dynamics with electronic transitions. *The Journal of Chemical Physics*, 93(2):1061–1071, 1990.
- [65] Kunihiko Ichimura. Photoalignment of liquid-crystal systems. *Chemical Reviews*, 100(5):1847–1874, 2000.